2001

Theoretical studies of isolated silicon and germanium clusters, and silicon clusters on Si(111)-7x7 surface

Bei Liu
Iowa State University

INFORMATION TO USERS

This manuscript has been reproduced from the microfilm master. UMI films the text directly from the original or copy submitted. Thus, some thesis and dissertation copies are in typewriter face, while others may be from any type of computer printer.

The quality of this reproduction is dependent upon the quality of the copy submitted. Broken or indistinct print, colored or poor quality illustrations and photographs, print bleedthrough, substandard margins, and improper alignment can adversely affect reproduction.

In the unlikely event that the author did not send UMI a complete manuscript and there are missing pages, these will be noted. Also, if unauthorized copyright material had to be removed, a note will indicate the deletion.

Oversize materials (e.g., maps, drawings, charts) are reproduced by sectioning the original, beginning at the upper left-hand corner and continuing from left to right in equal sections with small overlaps.

Photographs included in the original manuscript have been reproduced xerographically in this copy. Higher quality 6" x 9" black and white photographic prints are available for any photographs or illustrations appearing in this copy for an additional charge. Contact UMI directly to order.

Bell & Howell Information and Learning
300 North Zeeb Road, Ann Arbor, MI 48106-1346 USA
800-521-0600

Theoretical studies of isolated silicon and germanium clusters, and silicon clusters on Si(111)-7×7 surface

by

Bei Liu

A dissertation submitted to the graduate faculty

in partial fulfillment of the requirements for the degree of

DOCTOR OF PHILOSOPHY

Major: Condensed Matter Physics

Major Professor: Kai-Ming Ho

Iowa State University

Ames, Iowa

2001

UMI Number: 3003251

UMI Microform 3003251

Bell & Howell Information and Learning Company
300 North Zeeb Road
P.O. Box 1346
Ann Arbor, MI 48106-1346

Graduate College
Iowa State University

This is to certify that the Doctoral dissertation of

Bei Liu

has met the dissertation requirements of Iowa State University

Signature was redacted for privacy.

Committee Member

Signature was redacted for privacy.

Committee Member

Signature was redacted for privacy.

Committee Member

Signature was redacted for privacy.

Committee Member

Signature was redacted for privacy.

Major Professor

Signature was redacted for privacy.

For the Major Program

Signature was redacted for privacy.

For the Graduate College

TABLE OF CONTENTS

LIST OF TABLES

LIST OF FIGURES

ACKNOWLEDGEMENTS

I would like to express my sincere thanks to my advisor Professor K. M. Ho for his kind guidance, stimulating discussions, and support for this study. I also extend my thanks to Dr. C. Z. Wang. Being an open-minded and good friend, he shared valuable discussions and excitement of discovery with me through this work.

I thank my wife, Fengmei Liu, for her patience and encouragement through the study. I also thank my parents back in China for their support and concern.

I am grateful to Dr. Z. Y. Lu, Ms. Y. Y. Ye and Professor M. S. Tang for their help, valuable discussions and friendship. I am also grateful for my colleagues, faculty and staff of the physics department for their help, kindness and friendship.

I wish to thank Dr. David W Lynch, Dr. Costas Soukoulis, Dr. David A. Carter-Lewis and Dr. Les Miller for serving as my thesis committee and critical review of my thesis.

This work was performed at Ames Laboratory under Contract No. W-7405-Eng-82 with the U.S. Department of Energy. The United States government has assigned the DOE Report number IS-T2104 to this dissertation.

ABSTRACT

We have performed a systematic search for the ground state geometry of Si_n^+ and Si_n^- in the size range $3 \leq n \leq 20$ within the framework of density functional theory (DFT) with the local density approximation (LDA) and generalized gradient approximation (GGA). Various properties such as ionization potentials for neutral clusters, vertical detachment energies and photoelectron spectra for anions, fragmentation pathways and dissociation energies for cations, and mobilities for both anions and cations, are calculated and compared with experiments. The structures for medium-sized clusters ($10 \leq n \leq 20$) generally follow the prolate "stacked Si_9 tricapped trigonal prism (TTP)" pattern. Both bulk silicon and bulk germanium pack in a tetrahedral "diamond" lattice. Small silicon and germanium clusters with $n \leq 10$ also have identical geometries. We performed a systematic ground state search for Ge_n and Ge_n^+ up to 16 atoms. Like silicon clusters, medium-sized germanium clusters build up by stacking TTP subunits but the global minima for sizes starting from n=13 differ in details indicating that the growth patterns of silicon and germanium clusters diverge after n=12. Global minima search for silicon clusters (n=6-14) on the Si(111)7×7 surface were also carried out using both simulated annealing and a genetic algorithm. For n=6 and n=7, cluster atoms are anchored to the surfaces to saturate the dangling bonds of the surfaces but the cluster atoms are not bonded together directly. Starting from n=8, cluster atoms bond together and the clusters begin to grow in three dimensions for $n \geq 13$.

CHAPTER 1 INTRODUCTION

Clusters, a new phase of matter, have been studied not only for their interesting physical and chemical properties, but also for their importance in technological applications. Fundamentally, the study of clusters helps us understand how the various properties of clusters evolve as the cluster size grows. It will help us to understand how discrete energy states in clusters transform to energy bands in solids, insulators become metals, and reactivity turns into passivity. Technologically, people can make use of the special properties of clusters to make new devices.

Silicon is the most important material in the microelectronic industry. As device features are becoming smaller and smaller, they will soon reach the size of clusters where the special properties of silicon clusters become important. Except for fullerenes, silicon clusters are the most intensively studied clusters. One of the most challenging problems in cluster physics is to determine the structure of cluster containing more than a few atoms. Experimentally, silicon clusters are studied by ionization potential (IP) measurement [1-4], Raman [5] and infrared [6] spectroscopy of matrix-isolated species, photoelectron spectroscopy of gas phase anions [7-10], fragmentation pathways and dissociation energies of cations [11-14] and mobility measurements for charged clusters [15, 16]. Unfortunately, only mobility measurement give some direct information about cluster structures. However, mobility measurements map the very rich structural information of clusters into a single value, mobility, thus it is impossible to tell the detailed structure of a cluster just by its mobility. Since there is no experimental tool to identify the atomic arrangements within a cluster (like X-ray for bulk materials), structure determination of clusters mainly reles on theoretical calculation. Essentially all semiconductor surfaces are reconstructed. For a silicon or germanium cluster, every atom of the cluster can

be considered as a surface atoms and thus reconstructioned. So it is not surprising that silicon or germanium clusters' structures are totally different from the diamond structure of bulk materials.

Clusters tend to stay in their ground states which are the structures with the lowest energies among all possible structures. Systematic theoretical global searches are performed on clusters of a given size and several lowest energy isomers are obtained. The properties of these isomers are calculated and compared with possible experimental values. Those isomers whose calculated properties all agree with the experiments are considered to be the structures observed experimentally. The calculation techniques for solid total energy evaluation are described in Chapter 2 in detail. Briefly, the total energies of the clusters are calculated within the framework of density functional theory (DFT) [22] with the local density approximation(LDA) [23] and generalized gradient approximation(GGA) [24,25]. Since the ground state charge density is unknown at the beginning of the calculation, the calculation is iterated to self-consistency until the difference between input and output charge densities become smaller than a predefined threshold value. Since the valence electrons are responsible for almost all of the ordinary physical and chemical properties, the frozen core approximation is adopted. Using a pseudopotential to simulate the effect of nucleus and core electrons, the computation cost is significantly reduced. However, for complex systems, the DFT approach is still too expensive. Tight-binding(TB) calculation, which include the basic features of the electronic structures in the description of the interatomic interaction, is much faster than DFT calculation, and are used to treat more complex problems that can not be handled by DFT calculations.

DFT and TB can optimize an arbitrary cluster geometry to the nearest local minimum and evaluate its energy. However, the existence of multiple local minima in the energy landscape presents a major difficulty in searching for the global energy minima of clusters. Generally, four search methods are used. (i) Enumerate all the possible configurations, evaluate their energies and find the lowest energy ones. (ii) Based on known structural motifs, construct the structures manually. (iii) Simulated annealing using molecular dynamics. (iv) Structural optimization using genetic algorithm. Method (i) works for small clusters ($n < 8$), when n grows bigger,

the possible configurations increase explosively and become impossible to enumerate. Method (ii) can only be a subsidiary method because the growth motifs have to be predetermined. Also it is possible that the cluster under study does not follow such a motif. Method (iii) is described in Chapter 2 in detail. In principle, cooling down from a liquid phase to a solid phase slowly can lead to the ground state. Unfortunately, our calculation can only simulate a very short time of the cooling process based on current computer power. Thus this method will not always find the global minimum for big clusters. Method (iv) is described in detail in Chapter 3 and Chapter 5. The Genetic algorithm has better performance than simulated annealing in the global minimum search of silicon clusters [17]. The geometry relaxation in the search is performed using TB. A genetic algorithm based on DFT is still too expensive to perform. In this thesis, we combine method (ii), method (iii) and method (iv) for the global minimum search.

One very interesting problem in surface physics is the dynamical behavior of a surface such as step motion and island growth. Studies of clusters on surfaces will give some hint on how the atoms attach on the surface and grow. The dynamic processes on the Si(111)-(7×7) surface have been intensively studied. Recent experiments [18] showed that an especially stable magic cluster plays a very important role in these dynamic processes. We studied the structures of silicon clusters on the Si(111)-(7×7) surface with sizes n=6-14. We found that the structures of these surface clusters are totally different from those of isolated clusters.

Germanium is also an important group IV material in the semiconductor industry. Another group IV element, carbon, has bulk structure and cluster structures very different from those of silicon (it takes the graphite instead of the diamond structure as the lowest-energy bulk structure. Its clusters evolve from linear chain to cyclic structures then to fullerenes) Unlike carbon, germanium is much more similar to silicon, it takes the diamond structure as the lowest-energy bulk structure and previous studies show that its small clusters' ($n \leq 10$) structures are the same as silicon clusters' structures of the same size. However, mobility measurement [19,20] show that the transition from prolate to near-spherical structure happens at $n \sim 60$ for Ge_n while this transition happens at $n \sim$ 24-30 for Si_n, indicating that there is a large structural

difference between medium-sized silicon and germanium clusters. This thesis explores at which size the growth pathways of silicon and germanium clusters start to diverge.

In Chapter 2, the density functional theory (DFT) and local density functional approximation (LDA) is reviewed. Several LDA techniques used in this thesis and the basic concepts of molecular dynamics are described briefly. This chapter also reviews the tight-binding formalism.

In Chapter 3, the ionization potentials (IPs) are calculated for all important isomers of neutral Si_n ($n \leq 20$) and compared with experimental values. A systematic global minimum search is performed for Si_n^+ and Si_n^- with $n \leq 20$. Based on the global minima of cations and neutrals, fragmentation pathways are modeled for Si_n^+ with $n \leq 26$ and dissociation energies of cation are calculated for $n \leq 20$. Fragmentation pathways are very sensitive to the cohesive energies of clusters. Excellent agreement with experiments provide strong support for our optimized geometries. Vertical detachment energies (VDEs) of Si_n^- ($n \leq 20$) are calculated and compared with experiment. It turns out that the VDE is a very sensitive quantity in structural assignment of anions. Photoelectron spectra (PES) of Si_n^- ($n \leq 20$) are modeled using molecular dynamics. The PES contain rich information on the electronic structures of anions. Thus the agreement between our simulated PES and measurement strongly supports our geometries for Si_n^-. Modelled mobilities of important charged isomers are compared with experimental values. An scattering model which takes the electron cloud into account instead of just the nuclear positions is proposed. This model can describe the mobilities of both the silicon cation and anions. The excellent agreement between all the properties calculated and measurements indicate that the global minima of neutral and charged clusters with $n \leq 20$ adopt the tricapped trigonal prism (TTP) motif. The effects of LDA and GGA on the silicon cluster system are also discussed in this chapter.

In Chapter 4, a systematic global minimum search for Ge_n and Ge_n^+ ($n \leq 16$) is reported. Like silicon clusters of the same sizes, medium-sized germanium clusters resemble stacks of tricapped trigonal prism (TTP). However, the structures of Ge_n and Si_n for $n=13$, $n=15$ and $n=16$ differ in detail. The onset of structural divergence between the growth patterns of Si and

Ge clusters is confirmed by measurements of gas phase ion mobilities, fragmentation pathways, and dissociation energies.

In Chapter 5, both simulated annealing and genetic algorithm are performed to search for the global minima of silicon clusters on the Si(111)-(7×7) surface with n=6-14. When n=6 and n=7, the cluster atoms are attached to the surface but the cluster atoms themselves are not bonded together. The cluster atoms begin to bond together from n=8. From n=13, the clusters begin to grow in three dimensions. The energetic stabilities of these surface clusters are also studied.

CHAPTER 2 CALCULATION METHODS

2.1 First-Principles Calculation

Theoretical studies of the properties of materials very often require information that can be provided by a detailed description of their electronic properties. A solid state system is a many particle system which consists of atomic nuclei and electrons. Since the mass of nucleus is much bigger than that of an electron, nuclei can be considered as fixed at their instantaneous positions when the electronic properties are calculated. This is the well known Born-Oppenheimer or adiabatic approximation. Based on the Born-Oppenheimer approximation, the motion of nuclei and electrons can be considered separately. Further more, due to the huge mass difference between nuclei and electrons, we can treat the electrons as a many body quantum system while regarding the nuclei as classical particles.

Assuming the Born-Oppenheimer approximation, the electronic properties can be determined by the Schrödinger equation

$$\left\{ \sum_{i=1}^{N} \left[-\frac{h^2}{2m} \nabla_i^2 + v(\vec{r}_i) \right] + \frac{1}{2} \sum_{i \neq j=1}^{N} \frac{e^2}{\mid \vec{r}_i - \vec{r}_j \mid} \right\} \psi(\vec{r}_1, ..., \vec{r}_N) = E \cdot \psi(\vec{r}_1, ..., \vec{r}_N) \qquad (2.1)$$

where $\vec{r}_i$ is the position of the ith electron, N is the total number of electrons, v is the external field in which the electrons move, and E is the total electronic energy. Most often, v is the electrostatic potential generated by the nuclei, whose positions are assumed fixed and whose spatial extensions are assumed negligible.

Although in equation 2.1 we ignore the spin coordinates in order to simplify the problem, it is still impossible to solve equation 2.1 in the general case. The eigenfunction ψ depends on 3N position coordinates, and due to the electron-electron interactions (the (i,j) summation

in equation 2.1) it is not possible to reduce equation 2.1 to equations of reduced dimensions. In 1964, Hohenberg and Kohn [22] proved that the electron density $\rho(\vec{r})$ of the ground state determines uniquely the external potential v so that uniquely determines the ground state properties. That is to say, the ground state properties are functionals of $\rho(\vec{r})$. Specifically, the total energy E can be written as

$$E = T(\rho) + \int v(\vec{r})\rho(\vec{r})d\vec{r} + \frac{1}{2}\int\int \frac{\rho(\vec{r})\rho(\vec{r})}{(\vec{r}-\vec{r'})}d\vec{r}d\vec{r'} + E_{xc}(\rho) \tag{2.2}$$

where $\rho(\vec{r})$ is the density, $T(\rho)$ is the kinetic energy and $E_{xc}(\rho)$ includes all many-body contributions to the total energy. Kohn and Sham [23] reformulated the problem of calculating the total electronic energy by solving a set of single-particle Schrödinger-like equations:

$$\left\{-\frac{\hbar^2}{2m}\nabla^2 + \left[v(\vec{r}) + \int \frac{\rho(\vec{r'})}{\mid \vec{r}-\vec{r'} \mid}d\vec{r'} + \mu_{xc}(\rho(\vec{r}))\right]\right\} \psi_i(\vec{r}) = \epsilon_i \psi_i(\vec{r}) \tag{2.3}$$

$$\rho(\vec{r}) = \sum_{i=1}^{N} \mid \psi_i(\vec{r}) \mid^2 \tag{2.4}$$

$$\mu_{xc} = \frac{\delta E_{xc}(\rho)}{\delta(\rho)} \tag{2.5}$$

The ground state for the system is described by occupying the N lowest energy single particle orbitals. $\mu_{xc}(\vec{r})$ is the exchange-correlation potential. μ_{xc} and E_{xc} are functionals of the electron density $\rho(\vec{r})$. However, the form is unknown. Adopting the local density approximation (LDA), which consider the slowly varying density system as a uniform electron gas system locally. E_{xc} can be expressed as:

$$E_{xc} = \int \epsilon_{xc}(\rho)\rho(\vec{r})d\vec{r} \tag{2.6}$$

where $\epsilon_{xc}(\rho)$ is the exchange and correlation energy per electron of a uniform electron gas with density ρ. Notice that in this approach all effects due to variations in $\rho(\vec{r})$ are neglected. Since

most of the practical quantities depend only on integrals over the whole space, some of the errors related to this approximation are averaged out.

The generalized gradient approximation (GGA) considers the effects due to the variations of the electron density by adding $|\nabla|$ and $\nabla^2\rho$ terms to the local density functionals. Long-range effects are indirectly included. The most widely used GGA are due to Becke [24] and to Perdew and Wang [25].

The Kohn and Sham equations can't be solved exactly. Therefore approximation methods are used. Most methods are based on expanding the eigenfunction $\psi_i(\vec{r})$ in some basis:

$$\psi_i(\vec{r}) = \sum_{j=1}^{N_b} c_{ij}\phi_j(\vec{r}) \tag{2.7}$$

where $\phi_j(\vec{r})$ are the basis functions and N_b is the number of basis functions.

In many problems of solid state physics, the electrons can be grouped into valence electrons and core electrons. In many cases, the important physical properties are determined by the valence electrons. It is natural to reduce the quantum mechanical problem from an N_a electron problem to an N_v electron problem, where N_a is the total number of electrons in the system and N_v is the number of valence electrons. A pseudopotential is introduced to model the interaction between the valence electrons and the core. In a plane wave basis, since the pseudopotential is smoother than the real potential, much less plane waves are required. This make the computation significantly faster.

The most widely used pseudopotentials are the norm-conserving pseudopotentials proposed by Hamann, Schlüter and Chiang (HSC) [26]. These potentials have the following desirable properties:

(1) Real and pseudo valence eigenvalues agree for a chosen "prototype" atomic configuration.

(2) Real and pseudo atomic wave functions agree beyond a chosen "core radius" r_c.

(3) The integrals from 0 to r of the real and pseudo charge densities agree for $r > r_c$ for each valence state (norm conservation).

(4) The logarithmic derivatives of the real and pseudo wave function and their first energy derivatives agree for $r > r_c$.

Properties (3) and (4) are crucial for the pseudopotential to have optimum transferability among a variety of chemical environments. The norm-conserving pseudopotentials used in the calculations of this thesis are generated by the Troullier and Martins' approach [27].

Most currently applied density function methods differ in the choices of the basis functions $\phi_j(\vec{r})$ in equation 2.7. In this thesis, mainly I used three density function methods:

1. DMol

DMol [30] is a commercial software package developed by Molecular Simulations, Inc. It calculates variational self-consistent solutions to the density function theory equations, expressed in a numerical atomic orbital basis rather than analytical functions (i.e., Gaussian orbitals). When solving the Kohn-Sham (equation 2.3), frozen-core approximation may be used. Core functions are simply frozen at the values for the free atoms and valence orbitals are orthogonalized to them. Use of frozen cores reduces the computational effort without much loss of accuracy.

2. Car-Parrinello (CP) method

Car and Parrinello [31] regard the minimization of the Kohn-Sham functional as a complex optimization problem which can be solved by applying the concept of simulated annealing. The CP method treats the electron eigenfunctions $\psi_i(\vec{r}, t)$ and nuclear position $\vec{R}_I$ as generalized coordinates. The ground state of the system can be reached by molecular dynamics simulated annealing performed on these generalized coordinates. In this approach, diagonalization, self-consistency, ionic relaxation, and volume and strain relaxation are achieved simultaneously.

3. Finite-Difference-Pseudopotential(FDP) method

Chelikowsky [32] *et al.* developed a method to solve the Kohn-Sham equation in real space. The approach is based on utilizing the finite difference method [33]. The "basis" in this approach is a real space grid. A higher order expansion for the kinetic energy operator is performed. By this way, to solve the Kohn-Sham equation, a M $\times$ M matrix need to be diagonalized if there are M grid points. The M $\times$ M matrix is real, symmetric, and sparse.

These attributes can be utilized in expediting the diagonalization procedure.

2.2 Molecular Dynamics

Molecular dynamics (MD) simulation is a very useful method for studying the properties of materials at finite temperature. Furthermore, molecular dynamics based simulated annealing is also an important technique to search for the ground state geometry of clusters in this thesis.

Computer simulations using molecular dynamics generate information at the microscopic level. These detailed information is converted into macroscopic quantities (pressure, internal energy etc.) to compare directly with experimental measurements. In molecular dynamics, observable macroscopic property Q_{obs} is the time average of Q(Γ(t)) [28]:

$$Q_{obs} =< Q_{obs} >_{time} = lim_{t_{obs}->\infty} \frac{1}{t_{obs}} \int_0^{t_{obs}} Q(\Gamma(t))dt \tag{2.8}$$

where Γ is a point in the system configuration phase space defined by the position $\vec{r_i}$ and momentum $\vec{p_i}$ of the particles in the system. The evolution of Γ(t) is governed by Newton's equation of motion:

$$\vec{F_i} = m_i \frac{d^2\vec{r_i}(t)}{dt^2} \tag{2.9}$$

In practice, the equations of motion are usually solved using a finite-difference method in a step-by-step basis, i.e. a large finite number τ_{obs} of time steps of length $\delta t = t_{obs}/\tau_{obs}$ are taken. The time step δt is chosen such that it is small enough compared with the period of the highest vibration mode in the system and as large as possible to simulate a long time interval. In this case, equation 2.8 is rewritten as:

$$Q_{obs} =< Q_{obs} >_{time} = \frac{1}{\tau_{obs}} \sum_{\tau=1}^{\tau_{obs}} Q(\mathbf{\Gamma}(\tau)) \tag{2.10}$$

where τ stands for an index running over the succession of time steps.

One algorithm to solve equation 2.9 is the predictor-corrector algorithm. Considering the classical trajectory, an estimation of the positions, velocities etc. at time t+δt can be obtained by a Taylor expansion about time t:

$$\begin{aligned}
\vec{r}^{p}(t+\delta t) &= \vec{r}(t) + \delta t\vec{v}(t) + \frac{1}{2}\delta t^2\vec{a}(t) + \frac{1}{6}\delta t^3\vec{b}(t) + \ldots \\
\vec{v}^{p}(t+\delta t) &= \vec{v}(t) + \delta t\vec{a}(t) + \frac{1}{2}\delta t^2\vec{b}(t) + \ldots \\
\vec{a}^{p}(t+\delta t) &= \vec{a}(t) + \delta t\vec{b}(t) + \ldots \\
\vec{b}^{p}(t+\delta t) &= \vec{b}(t) + \ldots
\end{aligned} \tag{2.11}$$

The superscript p marks these as predicted values. But the above equations will not generate correct trajectories as time advances because the equation of motion has not been introduced yet. The equation can be introduced through a correction step. Based on the new positions $\vec{r}^{p}$, we can calculate the forces and accelerations at time t+δt. The difference between these and the predicted accelerations $\Delta\vec{a}(t+\delta t) = \vec{a}^{c}(t+\delta t) - \vec{a}^{p}(t+\delta t)$ are fed into the corrector step:

$$\begin{aligned}
\vec{r}^{c}(t+\delta t) &= \vec{r}^{p}(t+\delta t) + C_0\Delta\vec{a}(t+\delta t) \\
\vec{v}^{c}(t+\delta t) &= \vec{v}^{p}(t+\delta t) + C_1\Delta\vec{a}(t+\delta t) \\
\vec{a}^{c}(t+\delta t) &= \vec{a}^{p}(t+\delta t) + C_2\Delta\vec{a}(t+\delta t) \\
\vec{b}^{c}(t+\delta t) &= \vec{b}^{p}(t+\delta t) + C_3\Delta\vec{a}(t+\delta t)
\end{aligned} \tag{2.12}$$

The superscript c means these are for corrected values. The corrected values describe the current positions, velocities, accelerations, etc. This prediction and correction procedure is repeated for all the time steps in the duration of the simulation. Different values of the coefficients in equation 2.12 are required if we do the Taylor expansion in more or less terms. One set of coefficients we used is Gear's [29] fifth order coefficients and they are: $C_0 = \frac{3}{16}, C_1 = \frac{251}{360}, C_2 = 1, C_3 = \frac{11}{18}, C_4 = \frac{1}{6}, C_5 = \frac{1}{60}$.

2.3 Tight-Binding: A Semi-Empirical Method

First-principles calculations such as the local density functional formalism, are well developed and have already produced many significant results. However, the computational cost is prohibitive for large systems. Simulation with an empirical classical potential can not give accurate descriptions of phenomena where quantum mechanical effects are essential, nor can it give any information about electronic structure. [36] Tight-binding bridge the gap between first-principles molecular dynamics and simulations using empirical classical potentials because it incorporates electronic structure calculation into molecular dynamics through an empirical tight-binding Hamiltonian. The quantum mechanical many-body nature of the interatomic force is calculated naturally through the Hellman-Feynman theorem. The tight-binding binding energy expression for a system is:

$$E_{binding} = E_{bs} + E_{rep} \tag{2.13}$$

where E_{bs} is the band structure energy from the tight-binding Hamiltonian H_{TB}. E_{rep} represents all the parts of energies that are not included in the first term.

However, generating accurate and transferable tight-binding models for molecular dynamics simulation of realistic materials is still a very challenging task. Previous tight-binding models almost invariably adopt the two-center approximation for the hopping integral [35] which greatly simplifes the parameterization. While the two-center approximation is appropriate for systems where electrons are well localized in strong covalent bonds, it can not adequately describe systems where metallic effects are significant. Recently, Wang *et al* [37] developed an environment-dependent tight-binding potential model which takes the multicenter interaction into account by allowing the interatomic interaction to depend on the bonding environment. This model has remarkably improved transferability and the properties of the higher-coordinated metallic systems of carbon and silicon are well described by this model in addition to those of the lower-coordinated covalent structures.

In this model, the environment dependence of the hopping parameter is modeled through

incorporating two new scaling functions into the traditional two-center integrals. The first one is a screening function which reduces the interaction strength between two atoms in the solid if there are intervening atoms located between them. This allows us to distinguish between first- and farther- neighbor interactions within the same interaction potential without specifying separate interactions for first and second neighbors. The second function scales the distance between two atoms according to their effective coordination numbers. Longer effective bond lengths are assumed for higher-coordinated atoms. Thus the strength of the hopping parameters between two atoms depends on the coordination number of the atoms with weaker interaction strength for larger-coordinated structures. The form of this model is still two-center like while taking multicenter effects into account. A minimal basis set of one s and three p atomic orbitals is used to construct the tight-binding Hamiltonian and the pairwise repulsive potential take the form:

$$h_{ij} = \alpha_1 R_{ij}^{-\alpha_2} exp(-\alpha_3 R_{ij}^{\alpha_4})(1 - S_{ij}) \tag{2.14}$$

where h_{ij} denotes the possible types of interatomic hopping integrals or pairwise repulsive potential. r_{ij} is the real distance and R_{ij} is the scaled distance between atoms i and j. S_{ij} is the screening function which is near 0 if i and j are nearest-neighbor atoms and close to 1 otherwise so that the nearest-neighbor interactions dominates. Both S_{ij} and R_{ij} depend on the environment of atom i and atom j. The parameters for the scaling function R_{ij} and the screening function S_{ij} can be different for different hopping integrals, and pairwise repulsive potential and are determined in the fitting procedure. In this thesis, all the tight-binding simulations are based on this environment-dependent model [37].

CHAPTER 3 THEORETICAL STUDIES ON MEDIUM-SIZED SILICON CLUSTERS

3.1 Introduction

Clusters' structural and electronic properties are quite different from atoms and bulk materials. e.g. Silicon clusters with atom number from 10 to 18 can be viewed as stacks of Si_9 tricapped trigonal prism (TTP) subunit [17,38-43] whose bonding structure is very different from the tetrahedral bonding structure of bulk silicon material. Cluster physics fills the gap between atomic physics and solid state physics and it helps to answer questions like: When does cluster become solid, at which size do clusters begin to "realize" it will evolve to metallic or insulating, how does magnetism appear or disappear as atoms agglomerate to form solids [46]. Silicon is the most important material in semiconductor industry. Semiconductor device features are becoming smaller and smaller and will soon approach the size of clusters if current miniaturization trends continue. Enormous effort has been invested over the last decade to study the structural and electronic properties of silicon clusters [47-96]. Experimentally there is no direct tool to determine the structure of clusters, so the structure determination of clusters rely mainly on theoretical global energy minimum search and comparison between experimental results and calculated properties based on the theoretical geometries. In this article I describe the recent achievements in the theoretical structure identification of silicon clusters and the comparison with experimental results.

3.2 Neutral Silicon Clusters and Their Ionization Potentials

3.2.1 Global Minimum Search

For small silicon clusters Si_n with $n \leq 7$, it is possible to perform an exhaustive global minimum search theoretically because there are not many possible atom arrangements for these sizes. Clusters in these sizes have been extensively studied by theoretical and experimental methods. The structures of these clusters predicted by theory have been confirmed by photodetachment spectroscopy [7], Raman [5], and infrared [6] measurements on matrix-isolated clusters. For clusters with $n \geq 8$, too many local minima in the energy landscape present the main difficulty for theoretical global minimum search. For n=8-11, extensive searches have been performed but some of the conclusions are still the subject of debate [49, 52, 67, 93, 97]. For larger clusters, several different families of prolate clusters based on arbitrary stacking hexagonal rings [91, 92, 95] or triangles [93] have been proposed. None of these structures has been verified experimentally.

Recently, Ho *et al* [17] have successfully applied genetic algorithm (GA) to silicon cluster global minimum search. GA is an optimization strategy inspired by biological evolution. Manipulating the parent structures generates a bunch of child structures. Child structures and parent structures compete to live. The fittest structures live and become the new generation of parent. Other structures are discarded. In Ho's approach, four parent structures generate 16 "offspring" structures through "mating" process. "Offspring" clusters are relaxed through tight binding potential relaxation [98]. Fully relaxed structures replace the structures of parent if they have lower energy than their parent, or discarded otherwise. Continue this process for at least 600 generation with occasional mutation to increase the diversity of the population. Multiple populations are simulated to ensure a truly global search. By this way a bunch of promising candidate isomers are obtained. Their geometries are further relaxed to the nearby local minima and their energies are reevaluated by density functional theory using local density approximation (LDA). This approach find the same global minimum as the simulated annealing using Car-Parrinello LDA technique for $n \leq 16$. For bigger cluster, structures found by GA

have lower energy than those found by simulated annealing.

For n$\leq$ 10, the structures found by GA agree with the previously accepted structures. They are a C_{2v} triangle for Si_3, a D_{2h} rhombus for Si_4, and D_{3h} trigonal, D_{4h} tetragonal, and D_{5h} pentagonal bipyramids for Si_5, Si_6 and Si_7. The C_{2v} distorted octahedral structure was proposed for Si_6 by Raghvachari *et al* [51]. However, further relaxation of this C_{2v} structure of Si_6 leads to the D_{4h} tetragonal bipyramid structure, showing that this C_{2v} distorted octahedra structure of Si_6 is not a local minimum at all within LDA. For n=8, 9 and 10, the structures are as shown in Fig. 3.1. For n=11, GA found the C_{2v} [51] structure and a C_s(I) isoenergetic isomer (see Fig. 3.2) not described before. The C_s(II) isomer (Fig. 3.1) proposed by Lee *et al.* [65] and Sieck *et al.* [66] has higher energy by ~0.25 eV in both LDA and GGA. The tetragonal antiprism considered as ground state geometry in Ref. [51] (isomer 11e in the paper) is higher in energy by ~0.4 eV. The LDA and GGA energies for 12$\leq$ n $\leq$20 are significantly lower than previously proposed structures in literature.

From Fig. 3.1 and Fig. 3.2, it is clear that the geometries for 10$\leq$n$\leq$18 are prolate, resembling stacks of tricapped trigonal prism (TTP). The mobilities calculated for these structures are in good agreement with experiment [17]. For n=19, 20, LDA calculation show that the energies of the TTP based prolate structures (Si_{19} C_s and Si_{20} C_2 in Fig. 3.2) are about a fraction of eV higher than those of the near-spherical structures (Si_{19} C_{2v} and Si_{20} C_s in Fig. 3.2) from the global minimum search. However, the near-spherical structures don't agree with the mobility measurement while the prolate ones do. More recently, Ionel *et al* [44] developed a single parent GA and found a prolate Si_{19} C_1 structure (Fig. 3.2) whose energy is lower than that of Si_{19} C_s(I) (Fig. 3.2) by 0.15 eV. But its energy is still higher than the that of the near-spherical Si_{19} C_{2v}. For Si_{20}, they also found a prolate structure (Si_{20} C_{3v} in Fig. 3.2) whose energy (LDA) is the same as that of Si_{20} C_s in Fig. 3.2, and is 0.14 eV lower than that of Si_{20} C_2. The mobilities calculated based on Si_{19} C_1 and the Si_{20} C_{3v} are also in good agreement with experiment [44].

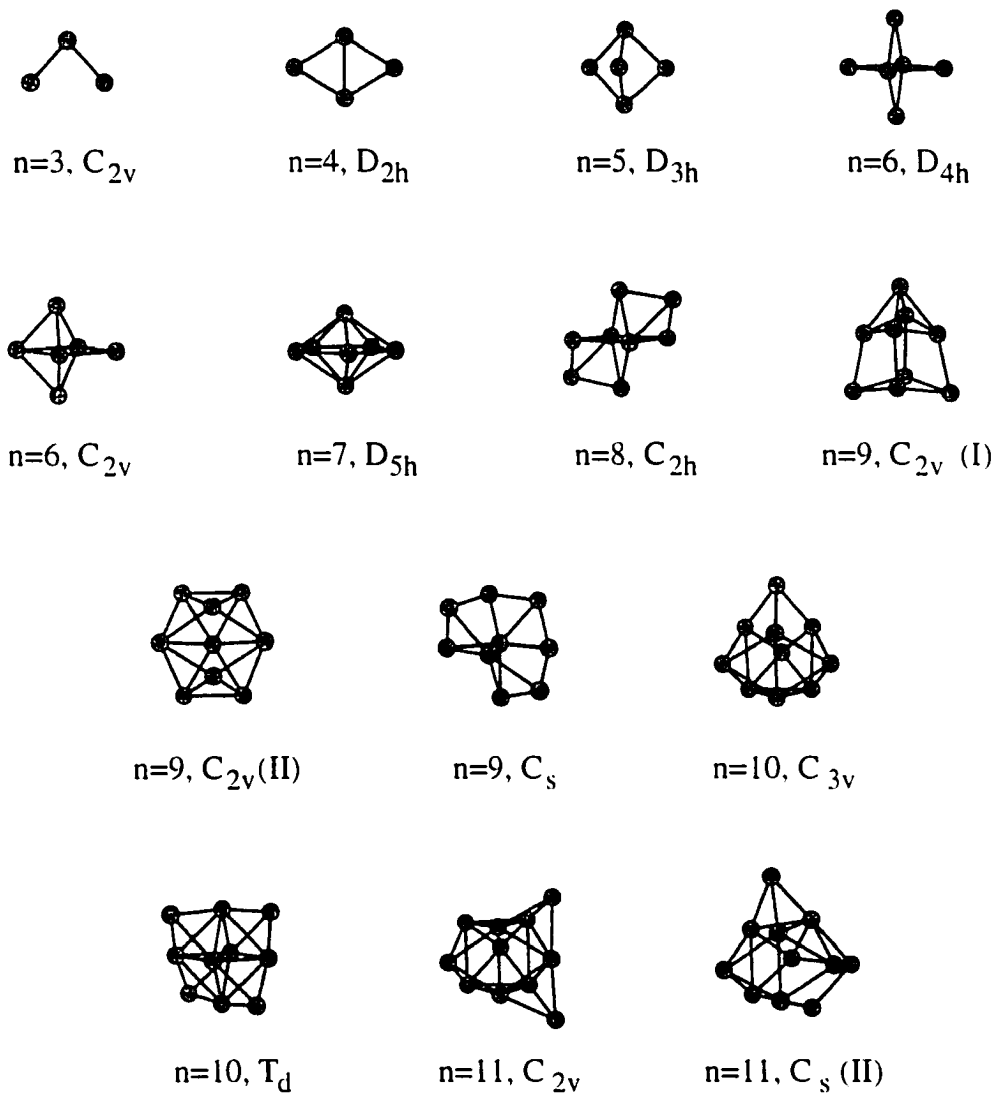

Figure 3.1 Lowest energy geometries proposed for Si_n ($n \leq 11$) neutrals in the literature.

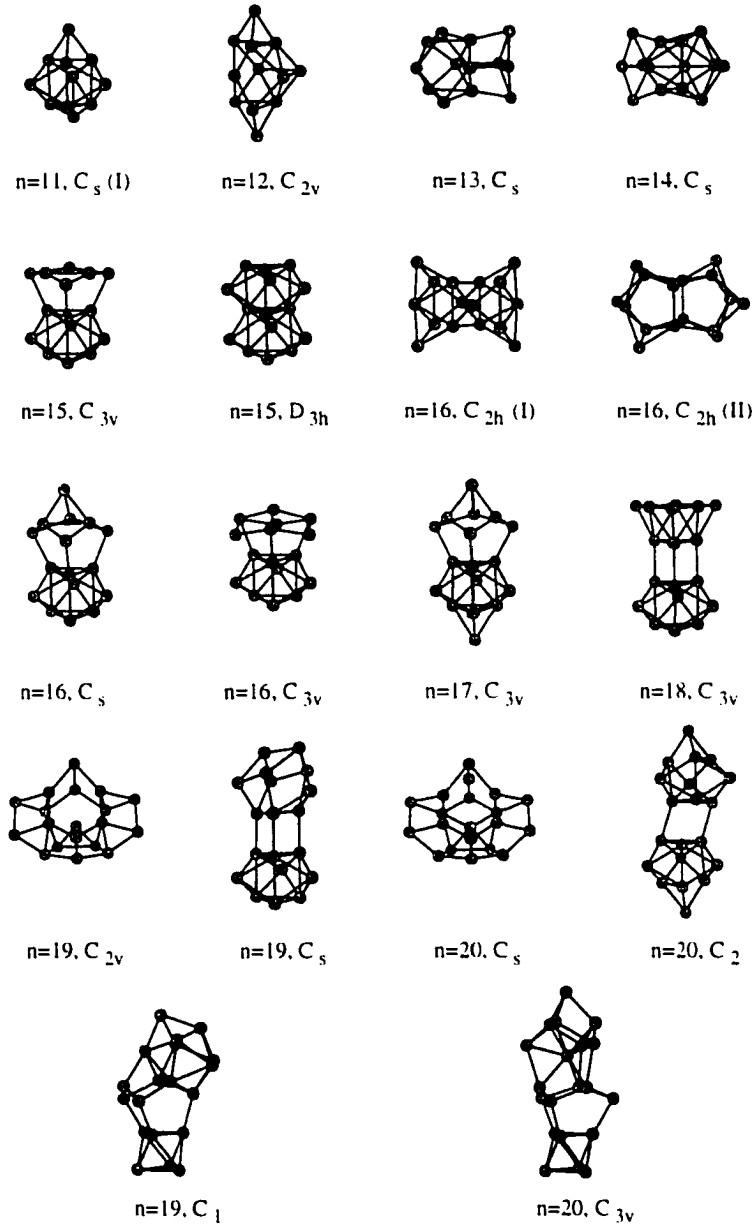

Figure 3.2 Lowest energy structures for Si_n (n=11-20) neutrals and geometries lying within 5 meV/atom found in the LDA calculations. Prolate structure for n=19 and 20 and structures of Ionel *et al* (C_1 Si_{19} and C_{3v} Si_{20}) are also shown. The C_{2v} geometry for Si_{19} is identical to that labeled in Ref. [17] as C_{1h}.

3.2.2 Ionization Potentials of Neutral Silicon Clusters

3.2.2.1 Calculation of Ionization Potentials

Most experiments for cluster research study charged clusters. However, ionization potential(IP) measurement provided very valuable data for neutral clusters. Photoionization thresholds for silicon clusters have been measured [1-4]. The measured IPs are bracket values. Furthermore, if the cluster structures change significantly upon ionization then the true thresholds would probably not be located, and the measured value will lie between the adiabatic ionization potentials(AIP) and the vertical ionization potentials(VIP).

The ionization potentials of silicon clusters have previously been calculated by MP4 perturbation theory [47], LDA and gradient-corrected PLSD [99], outer valence Green function(OVGF) technique [101], and tight binding(TB) [100, 102]. All these calculations only calculated the IPs of Si_n with $n \leq 10$, except for TB, which also calculated the IPs of Si_{11} and Si_{12}. But the icosahedron-based geometries assumed in the TB calculations are very high in energy. We analyzed the IPs for $n \leq 20$ based on the geometries optimized by GA and compared them with experiment values. We used all-electron localized-basis DMOL code [30] to do relaxation and evaluate the total energies of clusters. We employed the double numerical plus polarization basis set. Spin-polarization terms were included. Both LDA and GGA calculation were performed. For LDA we use the Vosko-Wilk-Nusair(VWN) functional for exchange and correlation and Perdew, Wang and Becke(PWB) functional for GGA. The VIPs were evaluated by the total energy difference between the relaxed neutrals and the ionized clusters with exactly the same geometry as the relaxed neutrals, while the AIPs were calculated by relaxing the ionized clusters toward to the nearest local minimum without any symmetry constraints. Our calculated IPs are listed in table 3.1.

The IPs calculated by PWB is below the LDA values by 0.05-0.2 eV. All the size dependent feature are the same for PWB and LDA IP values. In most cases, the difference between AIPs and VIPs are small, ranging from under 0.03 eV for Si_7 and Si_{10} T_d to 0.3 eV. The exceptional case is for Si_8 C_1/C_s, the difference is 0.67 eV for LDA and 0.57 eV for PWB. This is because for this isomer, the geometry changes significantly upon ionization, also the symmetry of the

cluster changes from C_1 to C_s upon ionization. In the range of comparison ($n \leq 10$), our IPs exhibit the same size dependent trend as previous calculations [47, 99, 101], although the absolute values differ (see table 3.1).

3.2.2.2 Structure Assignments

We compared the PWB IPs of Si_n clusters ($n \leq 20$) with the measurements in Fig. 3.3. The filled triangles are for the lowest energy (in GGA) isomers and empty ones are for other non-ground state isomers. All size-dependent experimental features for $n \leq 19$ are reproduced by our calculation, including the major peak at n=10 and the "plateau" for $12 \leq n \leq 15$. Unfortunately, the error margin of absolute values of the order of 0.4 eV (based on the data of n=16 and n=17) and a fairly broad experimental bracketing limit the utility of this comparison in distinguishing between different geometries. Also, the threshold measurements on an isomeric mixture will reveal the isomer with the lowest IP, even if its relative abundance is minor. Even with these limitations, we can still see that the calculated IPs for Si_{11} C_s (I) and Si_{12} C_s don't agree with the measurement nearly as well as those for the C_{2v} isomers of Si_{11} and Si_{12} (Fig 3.3). For n=12, this result is in accordance with the LDA and GGA calculations which show that the C_{2v} structure is in substantial lower energy than the C_s isomer. The C_{2v} and C_s (I) isomers of n=11 are essentially degenerate for neutral according to both the LDA and GGA energies. The Si_{17} C_2 isomer can be ruled out because its IPs are too low compared with the measurements. For n=19 and 20, The calculated IPs for our lowest energy "prolate" structures (Si_{19} C_s and Si_{20} C_2) and "near spherical" structures (Si_{19} C_{2v} and Si_{20} C_s) are very close. The calculated IPs of both Si_{19} C_s and Si_{19} C_{2v} agree with the experiment quite good while the kink observed for n=20 is not reproduced by either geometry. The calculated IPs of Ionel's "prolate" structures [44] for n=19 and n=20 are very close to our values and don't agree with the experiment value for n=20, either, indicating that the global minimum for Si_{20} neutral is not yet located. Real threshold IP measurements for silicon clusters that have an error margin of $\sim$0.1 eV will allow us to extract a lot more structural information from the comparison.

Table 3.1 Calculated ionization potentials (eV) of Si_n clusters up to n=20

Size	Point group	Our LDA, AIP-VIP	Our PWB, AIP-VIP	PLSD[a], AIP-VIP	OVGF, VIP[c]	MP4, VIP[d]	TB[e],VIP[f]	TB[b], VIP
1		8.29	8.30	8.53		8.0		
2		7.94-7.94	7.86-7.87	8.04-8.14		7.5	8.09/8.28	8.24
3	C_{2v}	8.18-8.27	8.11-8.20	8.36-8.47	8.14	7.9	8.11/8.38	8.49
4	D_{2h}	7.87-8.17	7.74-8.06	7.99-8.28	8.11	7.6	7.70/8.02	7.95
5	D_{3h}	8.25-8.32	8.12-8.18	8.22-8.42	8.19	7.8	8.07/8.08	8.53
6	D_{4h}	7.85-7.99	7.76-7.89			7.5	8.27/8.52	8.42
6	D_{2v}	7.66-7.98	7.51-7.54	7.70-8.18	7.81			
7	D_{5h}	8.11-8.14	8.02-8.04	8.04-8.24	7.83		7.73/7.77	8.08
8	C_{2h}	7.29-7.44	7.16-7.30	7.39-7.57	7.44		7.12/7.19	7.80
8[g]	C_1/C_s	6.65-7.32	6.61-7.18					
9	C_{2v}(I)	7.63-7.75	7.44-7.57				7.43/7.52	
9	C_{2v}(II)	7.32-7.50	7.20-7.41	7.25-7.60			7.10/7.12	
9	C_s	7.17-7.51	6.98-7.35		7.17			
10	C_{3v}	8.02-8.08	7.82-7.91	7.84-8.21	7.92		7.36/7.53	
10	T_d	7.66-7.68	7.52-7.52				7.27/7.34	

[a]Reference [99].
[b]Reference [102].
[c]Reference [101].
[d]Reference [47].
[e]Reference [100].
[f]Two values correspond to two different tight-binding parameterizations.
[g]Si_8 C_1/C_s has C_s symmetry for cation and C_1 for the neutral. Si_{19} C_{2v} is the same as the near-spherical geometry denoted in Ref. [17] as C_{1h}.

Table 3.1 (Continued)

Size	Point group	Our LDA. AIP-VIP	Our PWB AIP-VIP
11	C_{2v}	7.07-7.20	6.96-7.06
11	C_s(I)	6.62-6.82	6.50-6.72
11	C_s(II)	6.88-7.16	6.82-7.07
12	C_{2v}	7.43-7.60	7.37-7.45
12	C_s	6.68-6.89	6.64-6.76
13	C_s	7.24-7.48	7.03-7.32
13	C_{3v}	7.16-7.29	7.05-7.20
13	C_{2v}	6.85-7.03	6.68-6.84
14	C_s	7.08-7.41	6.94-7.31
15	C_{3v}	7.31-7.51	7.14-7.40
15	D_{3h}	7.50-7.52	7.37-7.41
15	C_1	7.10-7.51	6.98-7.43
16	C_{2h}(I)	6.88-6.95	6.77-6.90
16	C_{2h}(II)	6.61-6.66	6.51-6.58
16	C_s	6.88-7.10	6.74-7.02
16	C_{3v}	6.67-6.74	6.56-6.64
17	C_{3v}	7.02-7.19	6.89-7.07
17	C_2	6.68-6.79	6.53-6.63
18	C_{3v}	6.98-7.03	6.84-6.91
18	D_{3h}	6.89-6.94	6.75-6.79
19[g]	C_{2v}	6.73-6.83	6.57-6.75
19	C_s	6.82-6.96	6.69-6.81
19	C_s(II)	6.84-7.04	6.67-6.87
19	C_1	6.63-6.88	6.44-6.69
20	C_s	6.70-6.86	6.52-6.76
20	C_2	6.76-6.83	6.62-6.79
20	C_{3v}	6.90-6.93	6.86-6.89

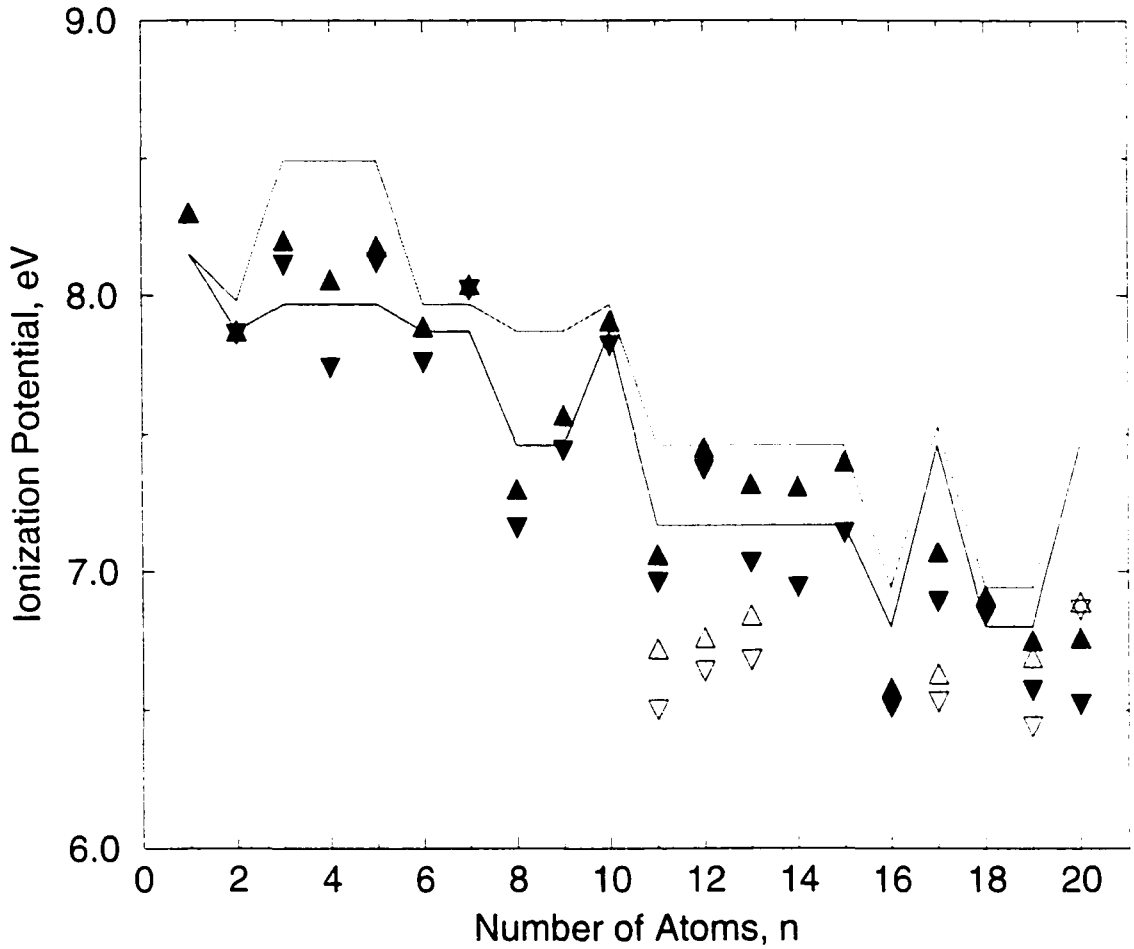

Figure 3.3 Ionization potentials of neutral silicon clusters. For n≥3, solid lines are the lower and upper boundaries obtained in the bracketing experiments of Fuke *et al.* (Ref. [3]). The limits for n=3 and 11 were adjusted on the basis of raw data (Ref. [3]) (see Ref. [4] and Note 48 in Ref. [103]). The value for the dimer is from the more accurate measurements (Ref. [4]) and that for the atom is from Ref. [151]. The upward and downward triangles are vertical and adiabatic IPs computed using the gradient-corrected PWB functional for our neutral geometries, respectively. Filled symbols are for the lowest energy isomers (in GGA), empty ones are for the Si_{11} C_s (I), Si_{12} C_s, Si_{13} C_{2v}, Si_{17} C_2, Si_{19} C_1, and Si_{20} C_{3v} (The Si_{20} C_{3v} correspond to the Si_{20} C_s (II) in Ref. [44]). For n=19 and 20, the "prolate" structures are assumed.

3.3 Cation and Fragmentation Pathways

3.3.1 Ground State Geometries for Cations

To search for the global minima of Si_n^+ with $n \leq 20$, we optimized a number of low energy isomers of the neutrals to the nearest local minima of cations without any symmetry constraints. The optimizations were performed using the all-electron localized-basis DMol code [30]. For $n \leq 12$, simulated annealing using Car-Parrinello LDA technique was also performed to locate the global minima. In agreement with Raghavachari [50] and Kishi [103], we found the C_{2v} edge-capped trigonal bipyramid structure, which can be viewed as Jahn-Teller distorted from the D_{4h} tetragonal bipyramid structure, is the ground state for Si_6^+. Similarly, the C_{2v} structures for Si_5^+ and Si_7^+ and the C_s structure of Si_{10}^+ (Fig. 3.4) are Jahn-Teller distorted from the D_{3h} Si_5, D_{5h} Si_7 and C_{3v} Si_{10} and these distorted structures are the global minima for respective cations. Kishi *et al.* [103] and Grein and co-workers [104] also found the same distortion for Si_5^+ and Si_7^+. For n=11, 15 and 16, one of the two nearly degenerate isomers for the neutral becomes the definite ground state for the cations. For n=11, the C_s (I) geometry, one of the two degenerate isomers for the neutral, is now favored by 0.04 eV/atom as the ground state for cation. The C_{3v} of Si_{15}^+ and the C_{2h}^+ (II) for Si_{16}^+ becomes the global minima for n=15 and n=16, respectively (see table 3.2 for the cohesive energy). For n=8 and 12, the cation ground states are quite different from the neutrals. The ground state for Si_8^+ is a capped pentagonal bipyramid. The C_s structure previously proposed [60, 66] for neutral Si_{12}, which lies over 0.05 eV/atom above the C_{2v} ground state for the neutral, is actually the global minimum for cation.

More recently, Ionel *et al* [44] applied GA directly to the global minimum search for charged silicon clusters, and they found new cation geometries which are more energetically favored (PWB) than the previously proposed structures [38]. For Si_n^+ with n=14, 17, 18 and 20, their structures are slightly favored by 0.007, 0.003, 0.005 and 0.005 eV/atom, respectively. For Si_{13}^+ and Si_{19}^+, these structures are favored significantly by 0.030 and 0.011 eV/atom, respectively. Based on the cohesive energies of their structures for Si_{13}^+ and Si_{19}^+, the agreement between calculated dissociation energies and measured values is significantly improved [39, 44]. Their

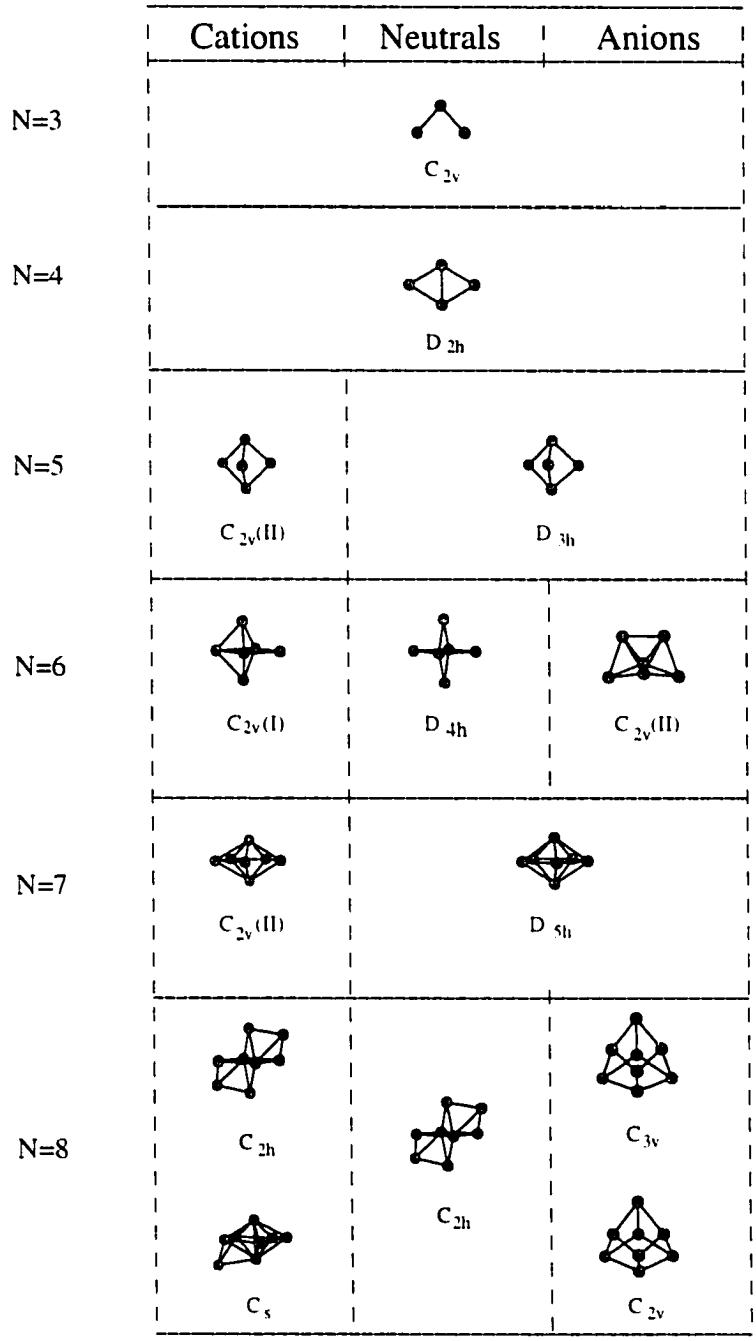

Figure 3.4 PWB global minima for Si_n^+, Si_n and Si_n^- (n=3-20). Multiple entries mean that the geometries are degenerate within the computational accuracy (~3 meV/atom).

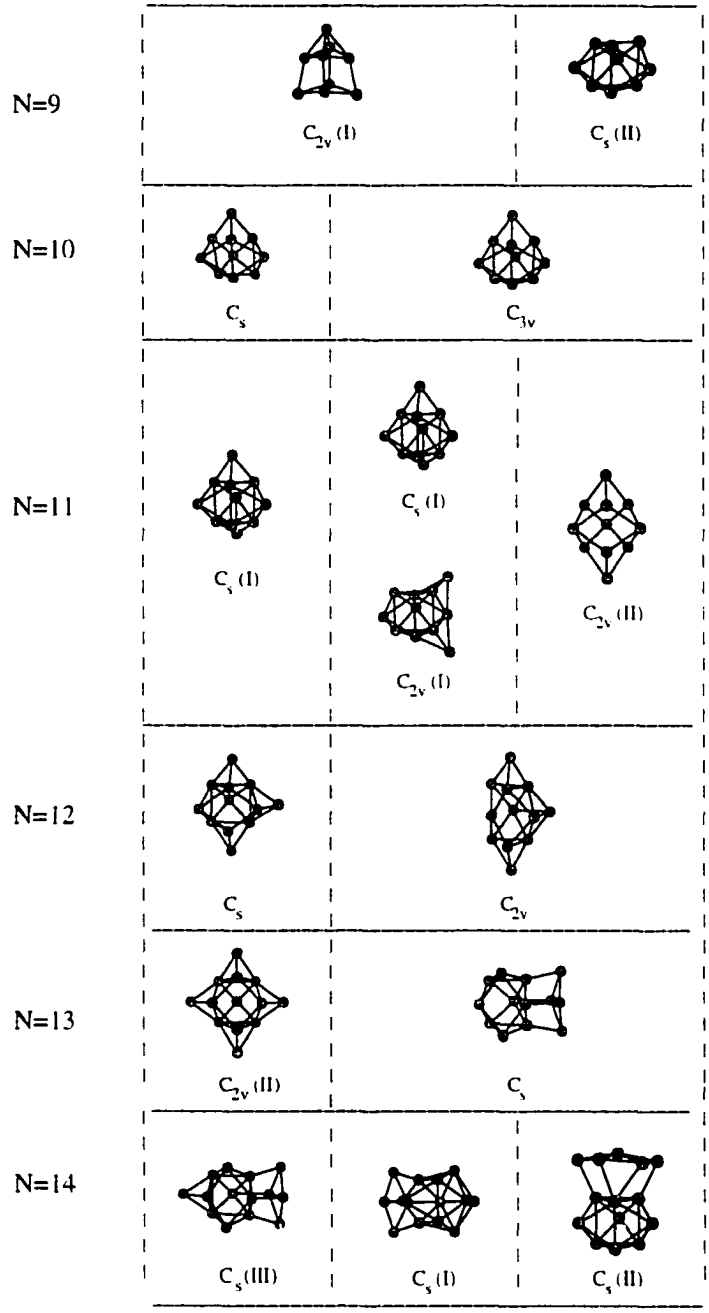

Figure 3.4 (Continued)

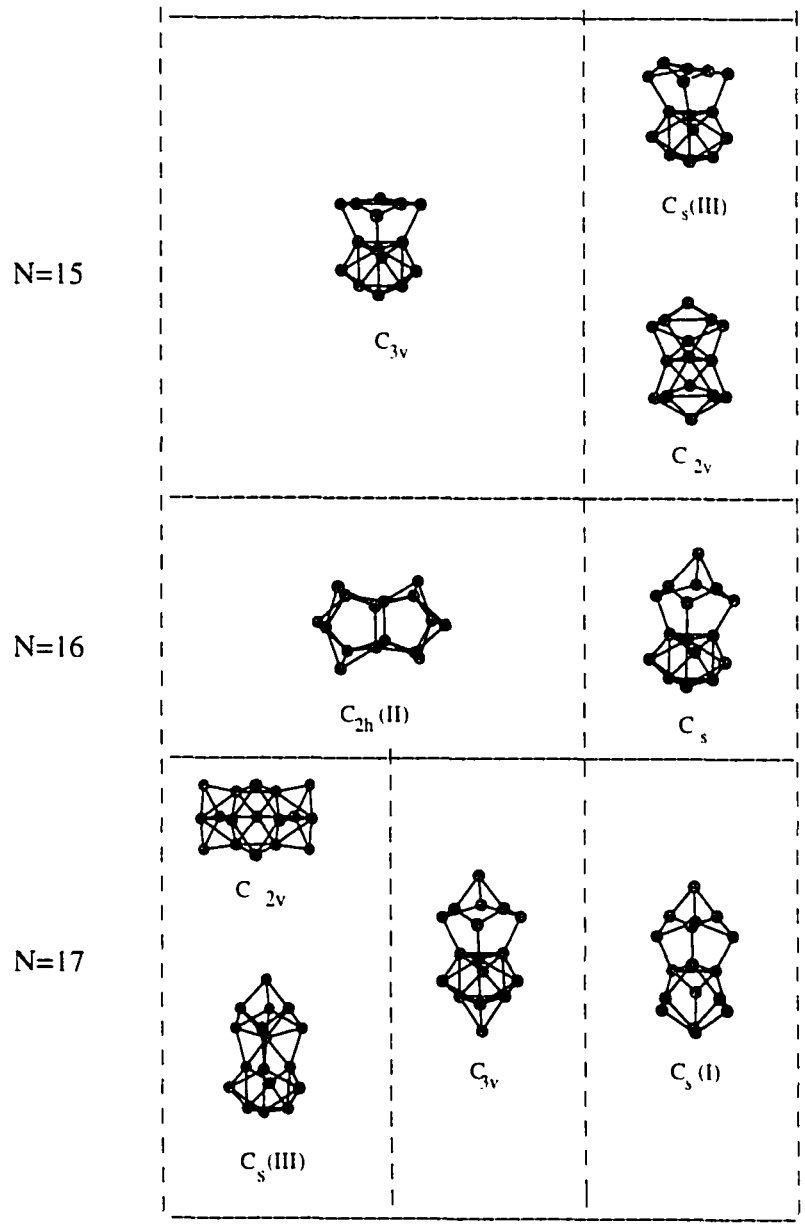

Figure 3.4 (Continued)

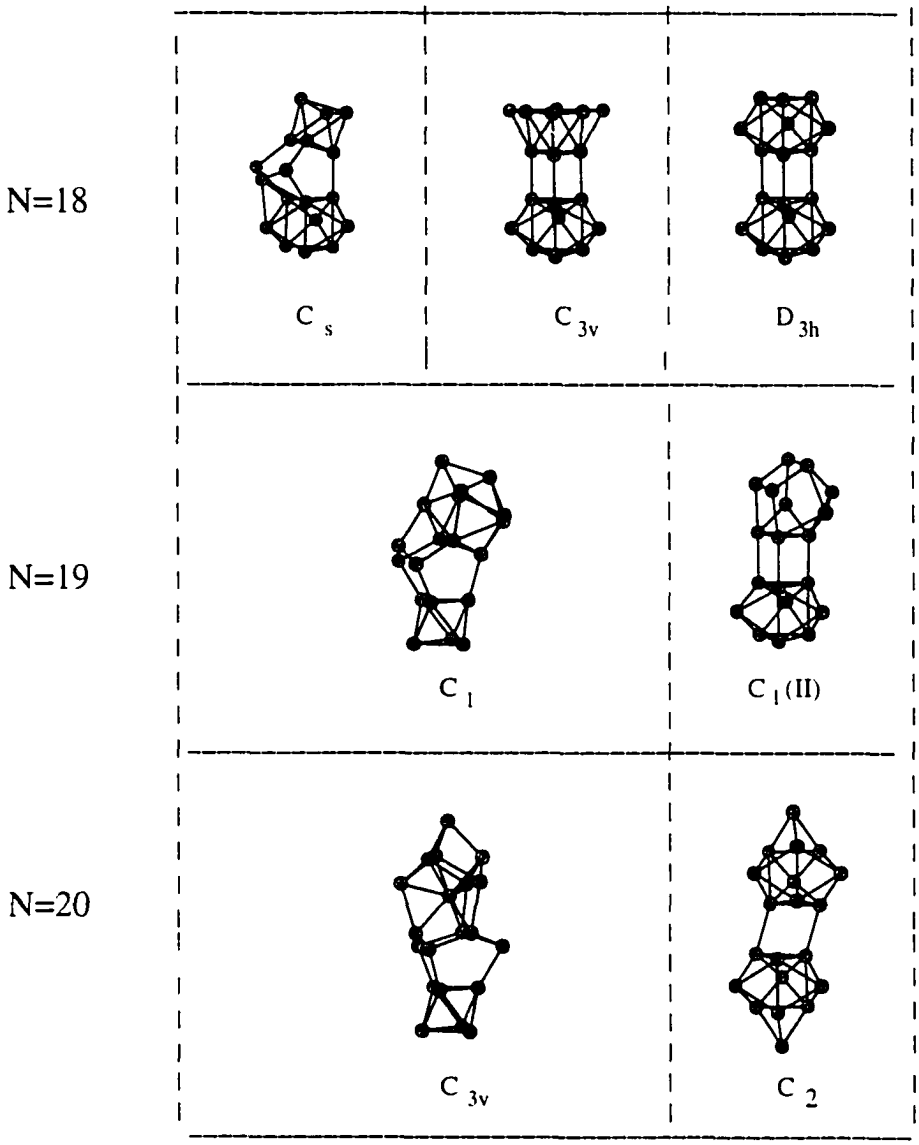

Fig 3.4 (Continued)

structures for Si_{19}^+ and Si_{20}^+ are also favored by 0.004 and 0.022 eV/atom as neutral (see table 3.2), respectively. The calculated IPs for these two neutral clusters are about the same as our previous lowest energy isomers. For anions, they found an isomer of Si_{19}^- which is favored by 0.011 eV/atom. For Si_{19}^-, the agreement in mobility is dramatically improved over that of our C_{2v} structure [42]. The reason for the different results from our previous studies maybe due to: (i) They applied GA directly to charged silicon clusters while in our previous studies we only relax the low energy neutral isomers as charged clusters to search for the global minima of charged clusters. (ii) In their approach, they adopt a different TB potential [45] from the potential developed by Wang *et al* [37]. (iii) They use a single parent GA instead of multiple parent GA. Giving up the diversity of parent, this single parent GA searches in much more detail around the parent geometry than the multiple parent GA [17]. Based on our previous studies and the result of the single parent GA. The ground state structures for cations which are different from neutrals are shownin Fig. 3.4. We can see that most structures with $n \geq 10$ also have the TTP motif.

3.3.2 Effect of Gradient Correction

Gradient-corrected post local spin density (PLSD) functional has been used to evaluate the energies of Si_n clusters for $n \leq 10$ [99]. However, these calculations were performed for the lowest energy isomers' LDA geometries. No gradient-corrected DFT treatment has been previously applied to larger silicon clusters. To check the effects of gradient correction, we performed optimization upon silicon clusters using two different generalized gradient approximations (GGA) functionals: the Perdew-Wang-Becke 88 (PWB) and Becke-Lee-Yang-Par(BLYP), as well as the LDA functional of Vosko-Wilk-Nusair (VWN). After full optimization of Si_n and Si_n^+, we found that, compared with LDA, all the bondlengths systematically increase by $\sim$1.5% in PWB and 2.5% in BLYP. While the cohesive energies decreased by 15%-20% in PWB and 25%-30% in BLYP. Also, the neutrals' IPs calculated by PWB is below the LDA values by 0.05-0.2 eV (table 3.1). But the relative energy order of different isomers remain remarkably unperturbed

Table 3.2 Cohesive energies of the low-energy geometries of Si_n, Si_n^+ and Si_n^- (n≤20), and measured and calculated mobilities for cations and anions. All calculated mobilities are by the SEDI model.

		(Cohesive energy, eV)						(Inv. mobili., Vs/m^2)			
	Point	Cations		Neutrals[a]		Anions		Cations		Anions	
n	group	*LDA*	*PWB*	*LDA*	*PWB*	*LDA*	*PWB*	*Calc.*	*Exp.*[b,c]	*Calc.*	*Exp.*
2		-2.003	-2.176	1.968	1.755	3.208	2.676				
3	C_{2v}	0.203	-0.165	2.929	2.537	3.688	3.267			915	920
4	D_{2h}	1.541	1.106	3.509	3.042	4.408	3.565	930	915	1040	1040
5	D_{3h}	2.141	1.642	3.791	3.266	4.272	3.733	1020	1005	1115	1115
	C_{2v}(I)	2.157	1.665	⇒D_{3h}		⇒D_{3h}		1020		...	
	C_{2v}(II)	2.160	1.669	⇒D_{3h}		⇒D_{3h}		1020			
6	D_{4h}	2.692	2.145	4.001	3.439	4.346	3.778	1105	1105	1210	1215
	$C_{2v}(I)^d$	2.724	2.187	4.001	3.438	⇒D_{4h}		1110		...	
	C_{2v}(II)	⇒D_{4h}		⇒D_{4h}		4.362	3.789	...		1210	
7	D_{5h}	2.988	2.410	4.147	3.555	4.418	3.828	1190	1195	1295	1295
	C_{2v}(I)	3.000	2.433	⇒D_{5h}		⇒D_{5h}		1195		...	
	C_{2v}(II)	3.019	2.452	⇒D_{5h}		⇒D_{5h}		1195		...	
8	C_{2h}	3.179	2.596	4.090	3.491	4.377	3.752	1300	1315	1390	1400
	C_1/C_s^d	3.185	2.596	4.016	3.422	4.358	3.736	1290		1385	
	C_{3v}	3.033	2.458	4.001	3.407	4.394	3.789	1325		1395	
	C_{2v}	3.094	2.517	4.041	3.445	4.396	3.791	1310		1395	
9	C_{2v}(I)	3.354	2.753	4.202	3.580	4.398	3.772	1375	1380	1465	1440
	C_1	⇒$C_{2v}(I)$		⇒$C_{2v}(I)$		4.440	3.812	...		1465	
	C_{2v}(II)	3.332	2.727	4.145	3.527	4.371	3.739	1365		1460	
	$C_s(I)^d$	3.284	2.690	4.081	3.466	4.400	3.760	1405		1465	
	D_{3h}	3.224	2.627	4.041	3.415	4.439	3.804	1350		1435	
	C_s(II)	⇒$C_{2v}(II)$		⇒$C_{2v}(II)$		4.449	3.819	...		1440	
10	C_{3v}	3.527	2.900	4.329	3.682	4.553	3.897	1425	1415	1510	1520
	C_s	3.550	2.924	⇒C_{3v}		⇒C_{3v}		1415		...	
	T_d	3.494	2.874	4.260	3.626	4.431	3.781	1455		1550	
	C_{4v}	3.473	2.842	4.244	3.595	4.541	3.874	1410		1505	
11	$C_{2v}(I)^d$	3.627	2.985	4.270	3.618	4.433	3.777	1520	1505	1620	1615
	C_s(I)	3.667	3.029	4.269	3.620	4.461	3.803	1515		1610	
	C_s(II)	3.662	2.973	4.247	3.593	4.477	3.816	1510		1600	
	C_{2v}(II)	3.627	2.986	4.219	3.577	4.480	3.821	1505		1595	
12	C_{2v}	3.684	3.034	4.303	3.648	4.499	3.826	1615	1600	1695	1700
	C_s	3.694	3.040	4.251	3.593	4.483	3.821	1595		1700	
13	C_s	3.746	3.093	4.303	3.634	4.538	3.860	1670	1680	1760	1775
	C_{3v}	3.734	3.082	4.285	3.624	4.456	3.792	1670		1750	
	C_{2v}	3.751	3.102	4.278	3.616	4.448	3.782	1675		1775	
	C_{2v}(II)	[e]	3.132	4.295	3.634	4.472	3.805	1675		[e]	

Table 3.2 (Continued)

n	Point group	(Cohesive energy, eV) Cations LDA	PWB	Neutrals[a] LDA	PWB	Anions LDA	PWB	(Inv. mobili. Vs/m^2) Cations Calc.	Exp.[b] [c]	Anions Calc.	Exp.
14	$C_s(I)$[d]	3.842	3.181	4.348	3.677	4.505	3.830	1745	1755	1845	1850
	C_s(II)	3.769	3.114	4.289	3.621	4.534	3.860	1770		1855	
	C_s(III)	3.851	3.188	[e]	3.663	4.505	3.835	1756		[e]	
15	C_{3v}	3.891	3.225	4.378	3.701	4.515	3.837	1845	1840	1945	1915
	C_s(III)	$\Rightarrow C_{3v}$		$\Rightarrow C_{3v}$		4.538	3.862	...		1945	
	D_{3h}	3.878	3.197	4.377	3.688	4.489	3.789	1760		1850	
	$C_s(I)$[d]	3.878	3.203	4.367	3.684	4.536	3.848	1795		1895	
	$C_s(II)$[d]	3.894	3.219	4.366	3.685	4.539	3.851	1795		1895	
	C_{2v}	[e]	3.215	[e]	3.657	4.545	3.860	[e]		1893	
16	C_{2h}(I)	3.909	3.236	4.339	3.659	4.482	3.800	1925	1930	2035	2010
	C_{2h}(II)	3.925	3.265	4.338	3.672	4.508	3.837	1950		2055	
	C_s	3.906	3.240	4.336	3.661	4.544	3.865	1925		2035	
	C_{3v}	3.917	3.232	4.334	3.642	4.468	3.772	1840		1935	
17	C_{3v}	3.970	3.298	4.383	3.703	4.533	3.850	2010	1985(1)	2130	2105
	C_s(I)	3.957	3.287	4.359	3.681	4.548	3.869	2015	2050(2)	2120	
	C_2	3.971	3.291	4.364	3.675	4.521	3.825	1925	1935(3)	2010	
	C_s(II)	3.955	3.281	4.343	3.664	4.475	3.794	2020		2135	
	C_{2v}	3.979	3.302	[e]	3.669	4.518	3.830	1991		[e]	
	C_s(III)	3.974	3.301	4.366	3.686	4.509	3.825	1995		[e]	
18	C_{3v}	4.013	3.340	4.401	3.720	4.513	3.830	2170	2115(1)	2270	2155
	D_{3h}	4.006	3.329	4.389	3.704	4.573	3.881	2095	2155(2)	2185	
	C_s	4.019	3.345	4.391	3.709	4.545	3.859	2107		[e]	
19	C_{2v}[d]	4.058	3.369	4.412	3.715	4.561	3.860	2070	2200(1)	2175	2265
	C_s	4.037	3.357	4.396	3.709	4.545	3.854	2195	2165(2)	2300	
	C_1	4.051	3.380	4.400	3.719	4.539	3.852	2184	2075(3)	[e]	
	C_1(II)	[e]	3.357	[e]	3.710	4.560	3.871	[e]		2258	
20	C_s	4.081	3.388	4.416	3.714	4.554	3.848	2145	2245	2245	2330
	C_2	4.061	3.381	4.399	3.712	4.559	3.866	2295		2395	
	C_{3v}	4.068	3.393	4.416	3.736	4.531	3.851	2284		[e]	

[a]The LDA energies of neutrals in the table differ from those listed in Ref. [17] by a small constant shift due to our use of a different local density functional code.

[b]The experimental mobilities listed here for certain cations deviate slightly from those reported previously (Ref. [38]). The present values result from the high-resolution measurements [16] and thus are deemed more accurate than those obtained using the injected drift tube technique (Ref. [38].

[c]For sizes where multiple isomers have been resolved [16] (cations with n=17-19), the ordering of their abundances is given in parentheses (from 1 to 3).

[d]Si_6 C_{2v} (I) is the same as C_{2v} in Ref. [38]. Si_8 C_1/C_s (capped pentagonal bipyramid) has a C_s for cation and C_1 for the neutral. Si_9 C_s (I) (Distorted tricapped octahedron) is identical to C_s in Refs. [17,38]. Si_{11} C_{2v} (I) is identical to C_{2v} in Refs. [17,38,40]. Si_{14} C_s (I) is the same as C_s in Refs. [17,38]. Si_{15} C_s (II) is identical to the isomer labeled in Refs. [38] as C_1, and C_s (I) is minor distortion of that structure. Si_{19} C_{2v} is the same as the Si_{19} C_s near-spherical geometry in Refs. [17].

[e]Not available.

in either GGA treatments (table 3.2). The energy difference among isomers varies on the order of one to several hundredths of eV/atom (less than one percent of the total cohesive energy) upon LDA, PWB and BLYP treatments. For n≥15, GGA favors more elongated geometries with BLYP favors more than PWB. This effect is already sufficient to make the C_{3v} and C_{2h} (II), which are degenerate with other isomers in LDA energetics, the clear global minima for Si_{15} and Si_{16}, respectively. It also make the C_{2h} and C_s isomers of Si_8^+ degenerate.

Experimentally the "prolate-to-spherical" transition begins at n=24 [20]. High resolution mobility spectra [16] observed the "near-spherical" Si_{17}^+ and Si_{19}^+ structures in minor abundance. However, the "near-spherical" isomers for Si_{19}^+, Si_{19}^- and Si_{20}^+ are lower in energy according to LDA calculation. The possible reasons are: (i) LDA doesn't count the effects due to the variations of electron density and GGA appears more appropriate to describe the silicon cluster system. In fact, the GGA treatment for charged or neutral Si_{19} and Si_{20} make the lowest energy "prolate" structures of n=19 and 20 the truly global minimum (see Table 3.2). (ii) At finite temperatures, entropic effect which possibly delay the onset of structural transition of carbon clusters need to be considered for silicon cluster, too. (iii) The energies of clusters should include zero-point energies(ZPE) [51], while the energies listed in Table 3.2 correspond to the bottom of potential wells. When the average vibrational frequencies of compared isomers are essentially equal, the ZPE effect just results in a constant shift for all isomers. This turn out to be the case when the competing isomers are roughly similar in shape [107]. Otherwise, the geometries having lower frequencies have lower ZPEs therefore are favored. Our preliminary evaluations based on the vibrational spectra calculated for selected cases indicate that this effect should additionally favor the prolate species for n=19 and 20 by several meV/atom.

3.3.3 Fragmentation Pathways and Dissociation Energies of Cations

Dissociation of silicon clusters has been intensively studied [11-14, 109-111]. Studies of dissociation of silicon cluster provide useful information on how the fragmentation pattern changes with cluster size as well as the stabilities of silicon clusters [108]. Unlike bulk silicon, which will evaporate individual atoms when heated, both silicon cations [1, 2, 11-14, 109] and

anions [110] undergo fission in the size range $9 \leq n \leq 70$. For clusters with n=12 to 18, they dissociate mainly by loss of 6 or 7 atom pieces. While for n=19 to 26, one of the dissociation pieces always contains 10 atoms [12, 109]. Raghvachari *et al* [111] have shown that n=6, 7 and 10 are particularly stable species theoretically. The measured size dependence of dissociation energies of Si_n^+ is also abnormal [14]. While the cohesive energy per atom increase steadily to the bulk cohesive energy for silicon cluster, the dissociation energy first vibrate between n=2 and 6 and then drop down its value by 60% from n=6 to $n \approx 20$ and then begin to increase to the bulk dissociation energy as n increase. Raghavachari and Rohlfing [117] have calculated the fragmentation energies of different fragmentation pathway for Si_n up to $n \leq 10$. Based on the lowest fragmentation energies among all the fragmentation pathways for $n \leq 10$, they explained the particular stability of magic clusters. However, they calculated the fragmentations of neutrals rather than cations and the octahedron-based geometries they assumed for n=9 and n=10 are now known not to be the global minimum for either the neutral or the charged clusters.

The fragmentation energy of neutral silicon cluster Si_n along a path leading to Si_m and Si_{n-m} is given by:

$$D_{(n,m)} = nE_n - mE_m - (n-m)E_{(n-m)} \tag{3.1}$$

where E_n is the cohesive energy per atom for neutral silicon clusters. Based on the E_n for the lowest energy geometries we found [17, 38], we calculated the fragmentation energies for various fragmentation pathways for each size up to n=26. The lowest fragmentation energy pathways for $n \leq 26$ are listed in table 3.3 assuming the E_n values by PWB functionals. For $n \leq 12$, our lowest energy fragmentation pathways agree with the earlier predictions based on MP4/6-31G* E_n values [111] except that we found alternative channels for n=9, 11 and 12. The dissociation energies corresponds to the lowest fragmentation energy pathways.

We use a formula similar to Eq. 3.1 to evaluate the fragmentation energy of cations Si_n^+ for fragmentation channel leading to Si_m^+ and Si_{n-m}. PWB per atom energies are used for Si_n^+ and Si_m^+. We calculate the lowest energy fragmentation channel for Si_n^+ with $n \leq 26$ (table 3.3)

Table 3.3 Fragmentation channels of silicon cluster neutrals and cations

n (reactant)	Products for neutrals[a]	(Products of primary calc.[b]	expt.	the secondary calc.[b c]	cations) expt.[d]
3	2	2	2	1	1
4	3	3	3	1	1,2
5	4	4	4	1	3
6	5	5	5	1,4	4
7	6	6	6	1	4,5
8	7	7	7	1,4,6	4
9	5,7	4,6,8	6		8
10	6	6	6	4	4
11	6,7	6	7	4	6
12	6,7	6	6	7,11	7
13	7	6	6	7	7
14	7	7	7	8	8
15	10	8	8	9,11	9
16	10	6	10	9,10,11	6
17	10	10,11	10		11
18	10,11	11	11	8	No
19	10	9	9	11,12	12
20	10	10	10	11	No
21	11	11	11	14	No
22	12	12,15	12		15
23	13	11,13,16	13		16
24	14	14	14	17	7,11
25	15	15	15	18	18
26	16,19	16	16	19	19

[a]Several fragmentation channels are given if their energies are within 0.12 eV . We report the larger product for neutrals and the ionic product for cations.

[b]Discounting the possibility of channels leading to a product with m$\geq$21.

[c]In cases with more than one calculated primary pathway no secondary pathway is shown.

[d]"No" means that the relative abundance of secondary products was so minor as to prevent identification ($\leq$1%).

and the dissociation energy for Si_n^+ with $n \leq 20$. The lowest energy fragmentation pathways of cations are pretty much the same as those of neutrals, except for n=9 and n=15. For n=9, the fragmentation product change from m=5, 7 for neutral to m=4, 6, 8 for cation. For n=15, the product change from m=10 to m=8. For n=17, 22 and 23, other competitive pathways are open for cations. They are m=11 for Si_{17}^+, m=15 for Si_{22}^+ and m=11, 16 for Si_{23}^+. These changes can be explained by the low AIPs of Si_4, Si_6, Si_8, Si_{11} and Si_{16} compared to their neighbors [38], which lead to these cations relatively more stable than respective neutrals. On the other hand, the relative high AIPs of Si_7, Si_{10} and Si_{19} make the alternative fragmentation pathways for neutrals, m=7 for both Si_{11} and Si_{12}, m=10 for Si_{18} and m=19 for Si_{26} close for cations. Similarly, the high AIP of Si_{12} make that it is an alternative pathway for Si_{22}^+ while it is the only pathway for Si_{22}.

Experimental fragmentation patterns have been studied by both photodissociation [1, 2, 11-13] and collision-induced dissociation [14, 110] (CID). In the range of $n \leq 27$, the dissociation patterns are quite similar for these two experimental methods. The photodissociation lead to a larger variety of fragments with lower abundance of each, thus the photodissociation correspond to higher excitation energy [14], while the excitation scheme of CID is particularly suited to identifying the lowest energy fragmentation pathways [108]. For Si_n^+ with $n \leq 26$, the primary and secondary (if there are) pathways of CID and our modeling based on our lowest energy geometries for neutrals and cations with $n \leq 20$ [17, 38] are compared in table 3.3. The calculated primary pathways are in excellent agreement with the CID experiment except for n=11 and 16. Even for n=11 and 16, our modeled primary pathways are the secondary pathways in CID [13, 109] and the primary pathways of CID are only ~0.3 eV higher in energy than the lowest energy pathways in our calculation. For both sizes n=11 and 16, the secondary pathways of CID are very important pathways with an intensity of 20-30% of the total. While in photodissociation [11], the two major pathways are almost equally intense for n=11. For n=16, our calculation predict the two fragments after dissociation are $Si_6^+ + Si_{10}$ instead of $Si_6 + Si_{10}^+$ for the CID. The comparison are very sensitive to both the cohesive energies of neutrals and cations. For example, the existence of an isomer of Si_{11}^+ lower in energy than our

global minimum [38] by only 0.1 eV would have switched the dissociation of Si_{15}^+, Si_{17}^+ and Si_{23}^+ into a wrong channel. 0.1 eV is only ~0.25% of the cohesive energy of Si_{11}^+. The existence of isomers which have lower cohesive energies than any of our global minimum cation Si_m^+ with m=12, 15-18 by just 0.1-0.4 eV would have caused Si_{m+7}^+ to lose Si_7 rather than Si_{10}. On the other hand, if we didn't base our modeling on the global minimum we found [17,38] then this excellent agreement will not have been achieved. For instance, if the search for any of the cations Si_m^+ with m=12-16 stop at the isomers higher in energy than our global minimum by only 0.1-0.4 eV, the wrong primary channel would have been predicted for Si_{m+10}^+. For Si_9^+, if the global minimum take either the C_s distorted tricapped octahedron [49] or the C_{2v} distorted tricapped trigonal prism [64], then the cation Si_{19}^+ would rather fragment into Si_{12}^+ + Si_7 instead of Si_9^+ + Si_{10}. Noticing Si_{10} and Si_{10}^+ are the fragmentation products for many cations, if the T_d tetracapped ocatehedron [49] were taken as the global minimum for Si_{10}^+ and Si_{10} instead of C_s and C_{3v} for Si_{10} and Si_{10}^+, then none of the primary fragmentation pathways of n=16, 17, 19, 20, 22-26 could be properly predicted.

We also properly predicted the second most important fragmentation channel for Si_n^+ with $n \leq 26$ where there are more than one fragmentation pathways observed in CID except for n=7 and 24. In these two cases, Like n=11 and 16 for primary channel, the second most important pathways in the CID rank the third in our calculation and are only higher in fragmentation energy by 0.3-0.4 eV than the second important pathways of calculation. The comparison of the second most important fragmentation channels furthermore prove that our lowest energy geometries [17,38] are very close to the real global minimum in cohesive energy.

The relative fragmentation energy difference determine the abundance of different channel products thus the comparison of modeled fragmentation pathways with experiment is valuable in checking the relative cohesive energies of clusters. While the comparison of dissociation energies provides a way to check the absolute value of clusters' cohesive energies. The dissociation energies correspond to the fragmentation energies of the lowest energy fragmentation energy pathways. Based on the lowest energy geometries we found (the prolate structures for n=19 and 20 were assumed) [17,38], we compared the dissociation energies (PWB) with the

experiment values in Fig. 3.5. For n≤18, our predicted dissociation energies agree with the measurement excellently except for n=13. The overall trend for n=19 and 20 agree with the experiment but the calculated cohesive energy for these two sizes are low. The comparison indicate that our prolate Si_{19}^+, Si_{20}^+ and possibly our Si_{13}^+ are not the true global minimum. This is not surprising because our Si_{19}^+ was constructed rather than by extensive search [17, 38]. The recent finding of new structures [44] for charged silicon clusters lead to the excellent agreement for n=13 and 19. The new structure for Si_{13}^+ is the C_{2v}(II) structure in Fig. 3.4 and the new Si_{19}^+ is the same isomer as the Si_{19} C_1 in Fig. 3.2. The new PWB dissociation energies for Si_{13}^+ and Si_{19}^+ are 2.71 eV and 2.62 eV, respectively, and agree very well with their experimental values of 2.70 eV. Furthermore, the new structure of Si_{13}^+ also improved the agreement of the fragmentation pathways comparison for n=23. The CID experiment shows only one primary pathway for Si_{23}^+: $Si_{23}^+ \longrightarrow Si_{13}^+ + Si_{10}$. Modelled by the old geometry of Si_{13}^+, this pathways is only one of the three primary pathways (table 3.3). The substantial lower energy isomer of Si_{13}^+ render the Si_{23}^+'s pathway leading to this product much more favorable than the other pathways, in better agreement with the measurement [44]. The new Si_{20}^+'s PWB dissociation energy is closer to the measurement but still somewhat low (1.80 eV versus 2.15 eV), suggesting that the true global minimum for Si_{20}^+ is not located, yet. Dissociation energies evaluated by LDA shows the same size dependency but the absolute value are overestimated as expected [38, 93].

3.4 Anion and Photoelectron Spectra(PES)

3.4.1 Ground State Geometries for Anions

We relaxed a number of low-energy neutral isomers of Si_n with n≤20 as anions without any symmetry constraints. We also performed the simulated annealing for n≤12 to locate the structures of the ground state anion clusters for each size. We also performed lower temperature simulated annealing for n≥13 starting from the geometries of low energy neutrals. This procedure is good for exploring the configurations around the low energy neutrals for any distortion that might lower the energy. Finally all geometries are relaxed by both LDA and

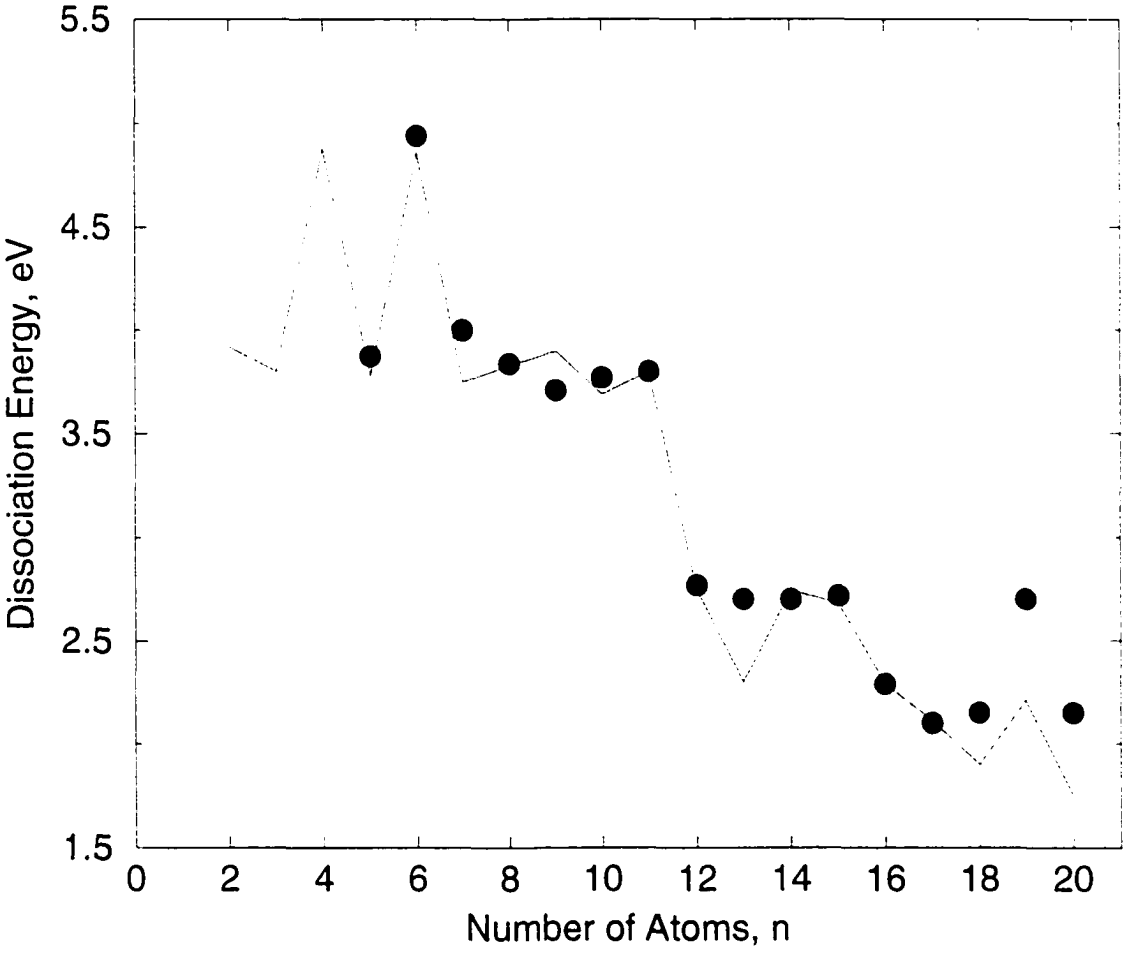

Figure 3.5 Dissociation energies of Si_n^+. Circles are the experimental values [14]. The line show the energies calculated employing the Perdew-Wang-Becke 88 gradient-corrected density functional.

GGA using the all-electron localized basis DMol package [30] for comparison. Double numerical basis set with polarization functions were employed.

The structures of the lowest energy isomers for cation, neutral and anion silicon clusters with n≤20 are shown in Fig. 3.4. The energies evaluated by both LDA and PWB for all important silicon clusters with n≤20 are listed in table 3.2. Like neutrals and cations we discussed before, the LDA or GGA treatment doesn't change the relative order of different isomers in most cases, with the exception of the more elongated isomers within GGA favored by 0.01-0.02 eV/atom. The bondlength from PWB is longer than that of LDA by 1.5% and the cohesive energies evaluated by PWB is 15-20% lower than that of LDA regardless of cluster charge.

For n≤10, our anion global minimum structures agree with the previous search [103, 114, 115, 117–121]. They are identical to those of neutral for n=3, 4, 5, 7 and 10. That is C_{2v} triangle for Si_3^-, D_{2h} rhombus for Si_4^-, D_{3h} trigonal bipyramid for Si_5^-, D_{5h} pentagonal bipyramid for Si_7^- and C_{3v} tetracapped trigonal prism for Si_{10}^-. The ground state of Si_6^- is neither identical to Si_6 nor Si_6^+. Instead, it take the C_{2v} (II) bicapped tetrahedron geometry. For Si_8^-, The C_{3v} tetracapped tetrahedron [117] is the previously accepted geometry. In either our LDA or PWB calculation, a tiny distortion of this structure to C_{2v} symmetry structure slightly lowers the energy. The TTP structural motif begin from n=9 for anion. For Si_9^-, the distorted TTP structure with C_s (II) point group is the global minimum whose energy is lower than that of the D_{3h} TTP by 0.13 eV in Raghavachari's calculation [117] and 0.10-0.15 eV in our DFT calculation. The lowest energy geometry of Si_{11}^- takes C_{2v} (II) point group. This structure ranks fourth in neutral Si_{11} and ranks second in cation Si_{11}^+. For Si_{12}^- and Si_{13}^-, the global minimum geometries are the same as their neutral global minimum and they are C_{2v} and C_s for Si_{12}^- and Si_{13}^-, respectively. For n=14, the global minimum of Si_{14}^- with C_s (II) point group is different from the global minima of C_s (I) structure for neutral and C_s (III) structure for cation. For n=15, the global minimum has C_s (III) symmetry which is distorted from the C_{3v} global minimum for neutral and cation. Like Si_6^-, the global minima of Si_{15}^- will merge to the high symmetry global minimum of neutral if relaxed it as neutral. The global minimum of

Si_{17}^- C_s (I) is also distorted from the C_{3v} neutral global minimum but is exists as a separate local minimum of neutral. For n=18, the D_{3h} isomer is the global minimum for Si_{18}^-, which is different from the C_s global minimum for Si_{18}^+ and the C_{3v} global minimum for neutral Si_{18}. The global minima for Si_{16}^-, Si_{19}^- and Si_{20}^- are the C_s, C_1 and C_2 isomers which are different from their global minima for neutrals and cations (C_{2h} (II) for n=16, C_1 for and C_{3v} for n=20).

3.4.2 Spectroscopic Evidence for the TTP Structure of Silicon Anions

Photoelectron spectroscopy reflects the electronic structure of neutrals at the anion geometries. Experimentally, the anion is photoexcited above the detachment threshold and the energy distribution of released electrons is recorded. Depending on the energy of photon, different energy levels of electrons below the highest occupied molecular orbital (HOMO) can be emitted. Photoelectron spectroscopy is a powerful tool for the structural characterization of isolated atomic clusters [7, 8, 61, 114, 116, 122]. Cluster geometries can be distinguished by comparing the measured photoelectron spectroscopy and those modeled on the possible candidate structures [41, 61, 114, 116]. Previously the structures of Si_6^- and Si_{10}^- have been confirmed to be the C_{2v} (II) bicapped tetrahedron and C_{3v} tetracapped trigonal prism by this way, respectively [61, 114, 116].

Recently, photoelectron spectra for Si_n^- up to n=20 were measured [41]. The results agrees with earlier measurements for $n \leq 12$ [9, 10]. Photoelectron spectra for Si_n^- with $n \geq 8$ are shown in Fig. 3.6.

For the low energy isomers of Si_n^- ($n \leq 20$), we first calculated their vertical detachment energies (VDE) and compared them with the experiments. For isomers whose calculated VDE agree with experiment, their PES is modeled and compared with the measured photoelectron spectra. VDEs are calculated by substracting the energy of anion from that of the neutral at the same geometry. The anions and their neutrals' energies were evaluated by both LDA and PWB using DMol [30]. The electronic structures were modeled by MD simulation at 300 K using the real space finite-difference-pseudopotential (FDP) LDA method [32]. PES were

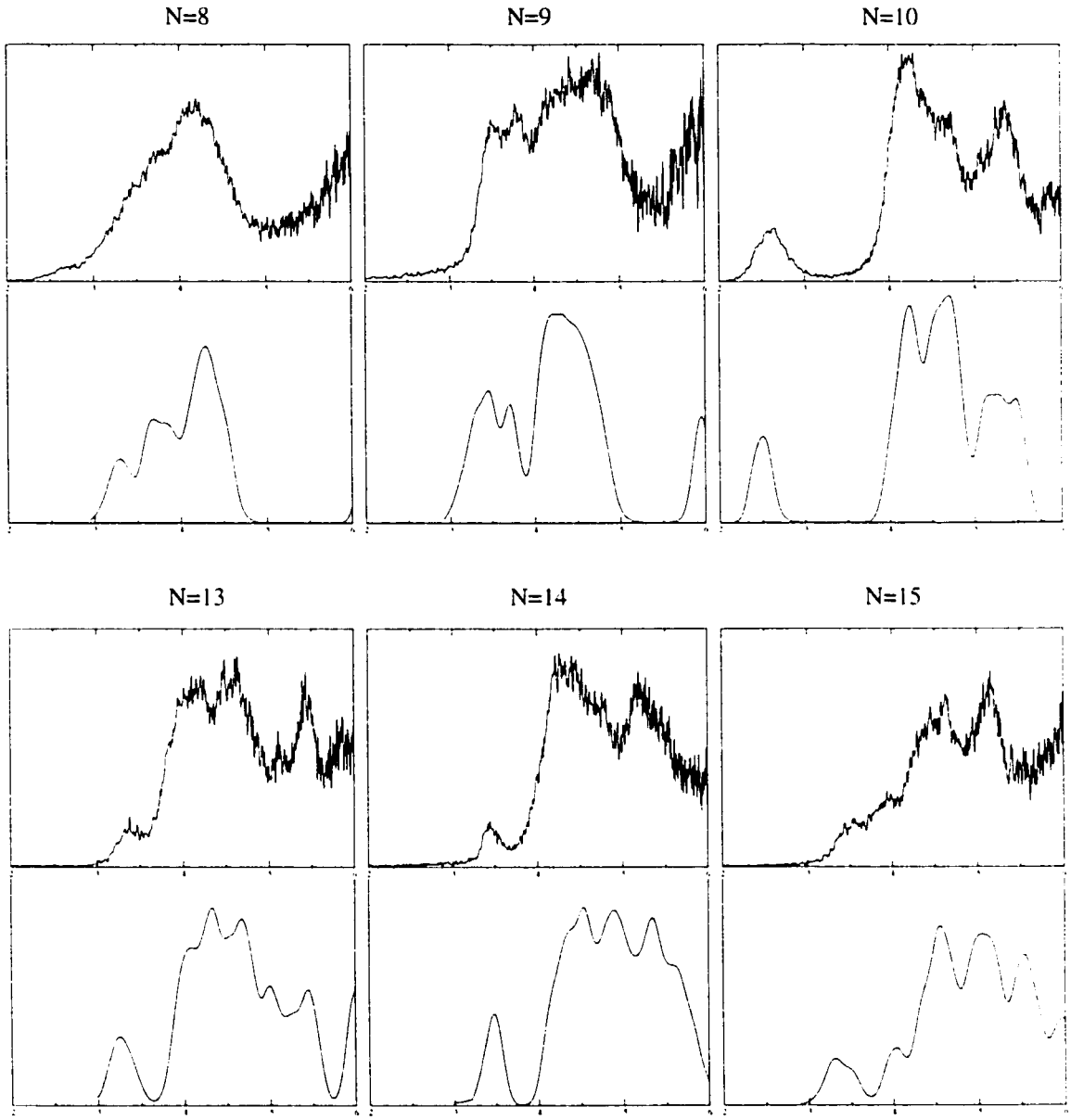

Figure 3.6 Photoelectron spectra for Si_n anions (n=8-20), measurements and LDA simulation (smooth lines). Calculations have been performed for Si_n^- ground states. For n=11, we show the PES simulated for the four low-energy C_s (II), C_s (III), C_s (IV) and C_{2v} (II) isomers.

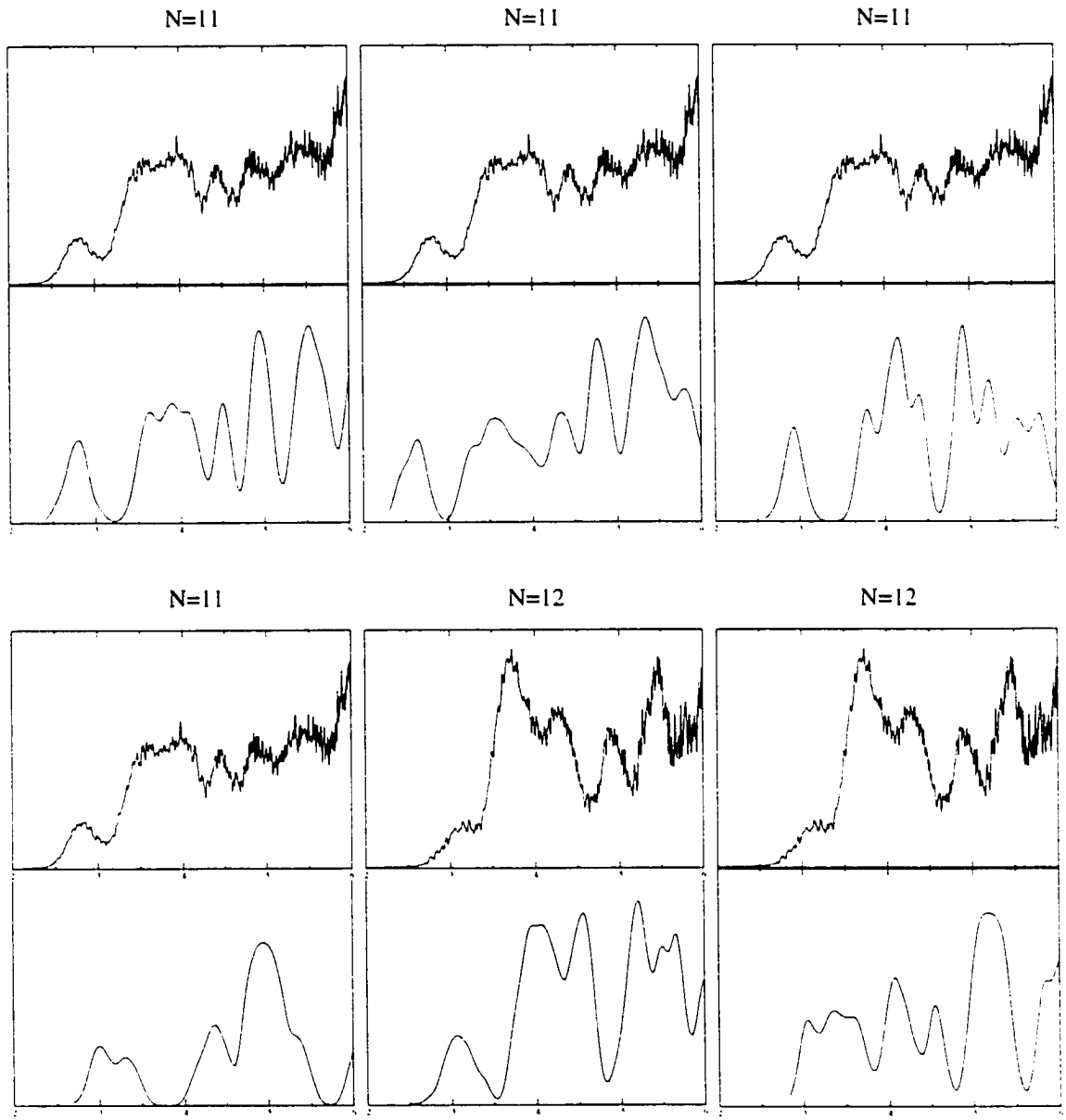

Fig 3.6 (Continued)

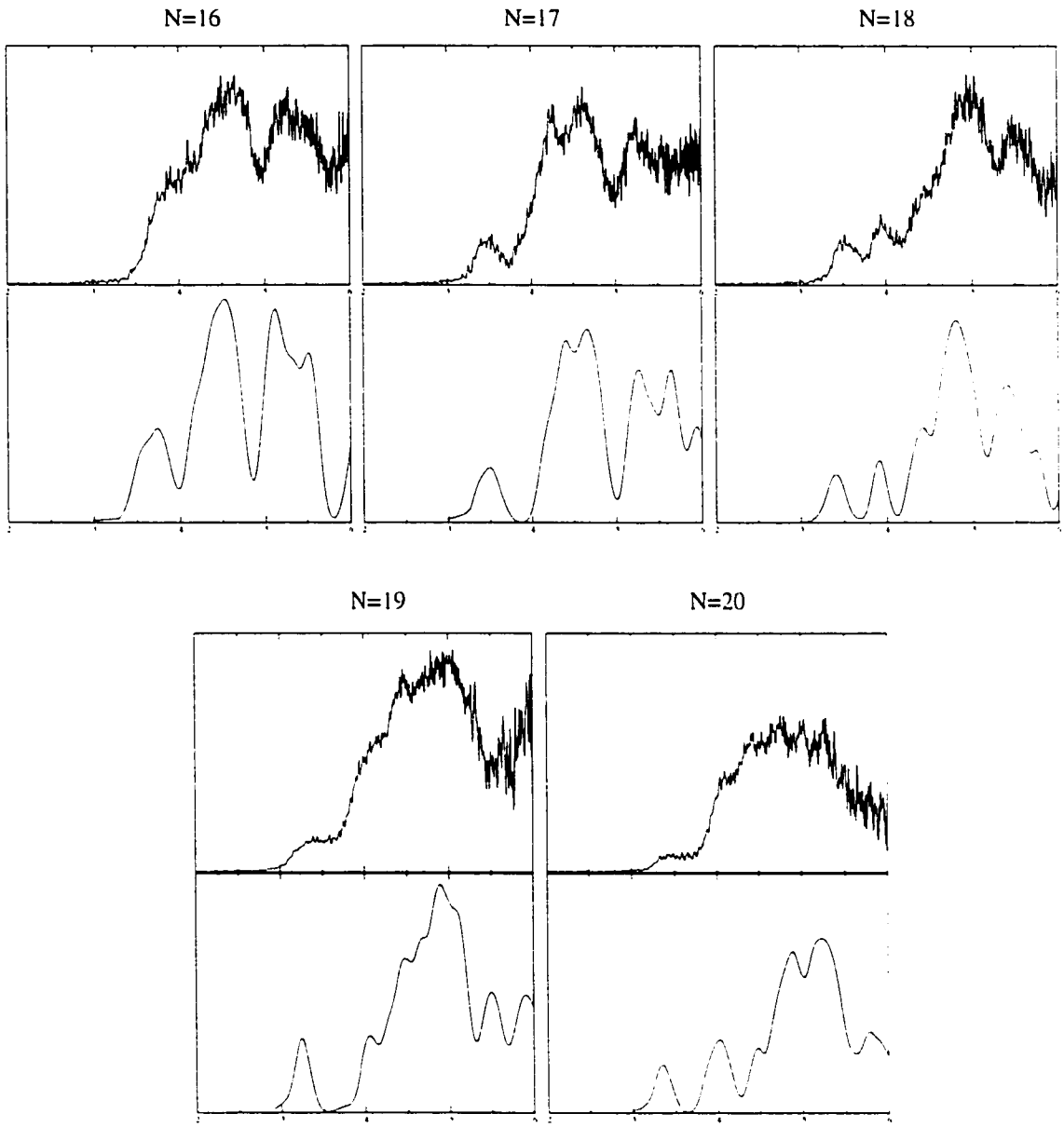

Fig 3.6 (Continued)

modeled based on the electronic structures with a 1000K gaussian broadening to fit the width of measured features. Because factors besides thermal broadening contribute to the total peak width, it is not surprising that measured feature widths are fit better assuming T $\sim$ 1000K rather than the real cluster temperature of $\sim$ 300K.

VDEs calculated for Si_n^- ($n \leq 20$) global minima and other important isomers are compared with the experimental values in Fig. 3.7. The VDEs turn out to be very sensitive to cluster structures. As we can see from Fig. 3.7, the VDEs of global minimum structures agree with the measured values while almost all other higher energy isomers do not (We estimated the combined error margin of calculation and experiment to be 0.3 eV) . For $n \leq 7$ and n=10, our results agree with previous calculation [61, 114, 116]. For Si_{10}^-, both the C_{4v} bicapped tetragonal antiprism and the T_d tetracapped octahedron, which are the second and the third lowest energy isomers, can be ruled out because their calculated VDEs deviate from the measured value by $\sim$ 1eV. For n=8, the global minimum for cation, neutral and anion are totally different. They are the C_1/C_s capped pentagonal bipyramid for cation [38], the C_{2h} distorted bicapped octahedron [38, 49] for neutral and C_{2v} (or C_{3v}) tetracapped tetrahedron [117] for anion. The mobilities for these three isomers agree with the measured mobility for Si_8^- within the error margin of 1%, so these structures cannot be distinguished by mobility comparison [42]. From Fig. 3.7, we can see that the calculated VDEs for the structures of Si_8^+ and Si_8 differ from the measured value by $\sim$ 0.5eV and 1.0 eV, respectively. While the VDE of the C_{2v} (or C_{3v}) tetracapped tetrahedron Si_8^- predicted theoretically [117] agree with the measured value excellently. For n=9, it is worthwhile to discuss the four low energy isomers: the C_{2v} (I) capped Bernal's structure [67], the C_{2v} (II) distorted TTP [93], the C_s tricapped octahedron [49, 117] and another distorted C_s (II) TTP [117]. The global minima for Si_9^- is distorted C_s (II) TTP [42, 117] and the global minimum for Si_9 and for Si_9^+ is the C_{2v} (I) capped Bernal's structure [67]. The mobility measurement can distinguish these structures by ruling out the C_s (II) isomer for Si_9^+, C_{2v} (I) and C_{2v} (II) for Si_9^- and C_s (I) for both charged states [38, 42]. The VDE comparison further confirm the structure assignment as the VDEs for the C_{2v} (I), C_{2v} (II) and C_s (I) isomers all fail to match the measured VDE while the calculated VDE of the

C_s (II) structure match the measurement perfectly. For n=11, the C_s (I) and C_{2v} structures are two essentially degenerate global minimum for neutral [38, 51], the C_s (I) structure become the obvious global minima for cation [38] and the C_{2v} (II) structure are the global minima for anion [42]. These structures cannot be distinguished by mobility because the modeled mobilities for these structures are within 1% of the measurement for either Si_{11}^+ or Si_{11}^-. We can identify the C_{2v} (I) isomer as the observed neutral Si_{11} based on the IP results [38]. The VDEs of the C_s (I) and C_{2v} structures do not agree with the measured results while all the calculated VDEs of the four virtually degenerate structures of Si_{11}^- (the C_{2v} (II), C_s (II), C_s (III) and C_s (IV) isomers in Fig. 3.8) agree with the measured VDE within the estimated error margin of 0.3 eV. These structures cannot be distinguished because they also have similar mobilities. The VDE of C_{2v}, the global minimum for both neutral and anion of n=12 [42], match the measured value. However, so does the VDE of the C_s geometry global minimum for cation [38]. Also, the mobilities calculated for these two isomers for anion are essentially equal and agree with measurement. Further comparison with the measured PES spectra of Si_{11}^- is necessary to elucidate the structure of Si_{11}^- and Si_{12}^-. The VDE for the C_s structure, which is the global minimum for both neutral and anion of n=13 [42], agree with the measurement while the VDEs for other isomers are significantly lower. For n=14, the VDE of the C_s (II) ground state of Si_{14}^- [42] fits the experimental value while that of the C_s (I) ground state of neutral [38] doesn't. For n=15, neither the C_s (III) structure found to be the global minima for Si_{15}^- [42], nor the C_{3v} global minima for both neutral and cation [38] agree with the experiment. However, a new isomer of Si_{15}^- with C_{2v} point group [44], which is essentially degenerate with the C_s (III) Si_{15}^- (the C_{2v} is lower in energy by 0.11 eV in LDA but higher by 0.03 eV in PWB), match the experiment in VDE nicely. The VDE of the lowest-energy Si_{16}^- isomer with C_s point group agree the measurement. While the VDE of C_{2h} (II), which is the lowest-energy isomer for the neutral and cation of n=16, doesn't. The situations for n=17, 18, 19 and 20 are similar: the calculated VDEs of the global minimum for anions agree with the experimental values while those of all other structures don't.

The measured and simulated PES are compared in Fig. 3.6. Except for n=11, 12, and (to

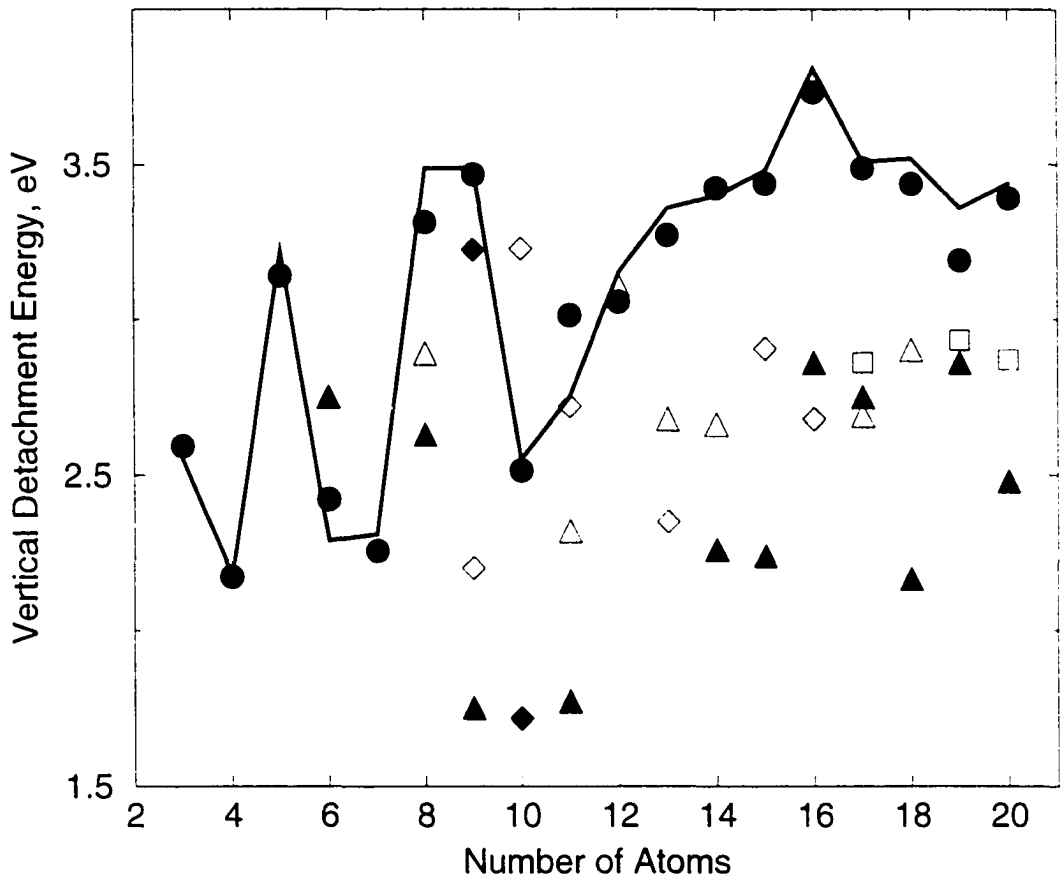

Figure 3.7 Vertical detachment energies of Si_n^- ($n \leq 20$). The line indicates the measurements. The symbols mark values calculated using LDA for a variety of geometries: the lowest-energy Si_n^- [42, 44] (circles, C_{2v} structure adopted for Si_{15}^-); isomers that are global minima for Si_n [17, 42, 44] when different from Si_n^- (filled triangles, Si_{11} C_{2v} (I) assumed); isomers that are global minima for Si_n^+ [38, 42, 44] when different from both Si_n^- and Si_n (empty triangles, C_s geometry assumed for Si_8^+); some other low-energy TTP-based species: Si_9^- C_{2v} (II) distorted TTP [42, 93], Si_{10}^- C_{4v} bi-capped tetragonal antiprism [115], Si_{11}^- C_s (II) [42, 66], Si_{13}^- C_{3v} capped trigonal antiprism [42, 150], Si_{15}^- C_s (III) and Si_{16}^- C_{2h}^- (I) [42] (empty diamonds); octahedron-based structures [42, 117] Si_9^- C_s (I) and Si_{10}^- T_d (filled diamonds); and near-spherical [42] Si_{17}^- C_2, Si_{19}^- C_{2v}, and Si_{20}^- C_s (squares). VDEs computed using PWB are within 0.1-0.2 eV of LDA values, typically (but not always) on the lower side.

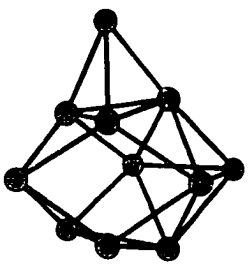

Si_{11}^- C_s (II) 3.816(2.795)

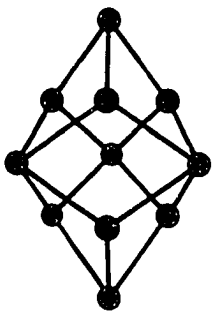

Si_{11}^- C_{2v}(II) 3.821(3.012)

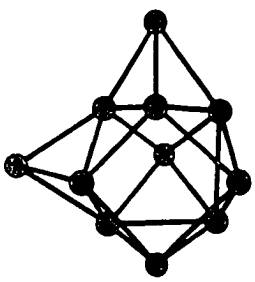

Si_{11}^- C_s (III) 3.818(2.665)

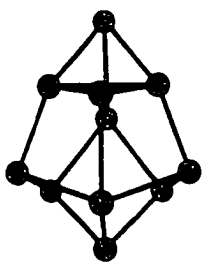

Si_{11}^- C_s (IV) 3.818(2.936)

Figure 3.8 Four near-degenerate lowest energy Si_{11}^- isomers that have vertical detachment energies close to the measured value. We list calculated cohesive energies (PWB in eV/atom) and VDEs (LDA, eV) in parentheses.

some extent) 20, PES simulation based on the global minima clearly reproduce all the significant features distinguishable in the measured PES. While for n=11, the C_s (II) Si_{11}^- isomer whose energy is higher than the global minima isomer C_{2v}^- (II) Si_{11}^- by 0.06eV is essentially degenerate with the global minima (Fig. 3.8) and this isomer's simulated PES agree with the experiment perfectly. The simulated PES of Si_{12}^- C_s and the other two isomers of Si_{11}^- with point group C_s (III) and C_s (IV), whose energies are a few meV/atom above their global minima, do not fit the measurement even their VDEs agree with the measured values. For n=19, the global minima's VDE is lower than the measured value by $\sim$ 0.3 eV which is close to the error margin, so the agreement of VDE for n=19 is kind of soft. The mobility calculated for the lowest energy Si_{20}^- located doesn't agree with the measurement [42]. Thus perhaps the ground state for Si_{20}^- is yet to be found. Except for n=10 and 11, the observed Si_n^- isomers are those with highest VDEs. This is because the lowest-energy isomers tends to have the lowest-lying HOMOs thus have the highest VDEs.

The PES of silicon anion with n=8 and 9 exhibit ledges at energies down to $\sim$2.5 eV while the PES for other sizes do not have this feature. These ledges normally indicate the existence of multiple isomers with low VDE. But no low cohesive energy isomers with the requisite VDE are found for these sizes. These ledges may originate from anions trapped in the geometries of their neutral global minima. The calculated PWB VDEs for anions relaxed from their neutral global minimum geometries are 2.45 eV and 2.67 eV (the requisite VDEs for the ledges) for n=8 and 9, respectively. Experimentally, the anions are generated in a laser vaporization source by attachment of electrons to neutrals. A anion may then assume the global minima geometry for anion or keep the geometry of the global minimum neutral depending on the energy barrier between these two structures and the source conditions. Besides n=8 and 9, the neutral and anion global minimum structures differ for many other sizes. However, for other sizes the structural differences between neutral and anion global minima are smaller which may lead to the lower energy barrier for structure rearrangement than for n=8 and 9.

3.5 Charged Clusters and Mobility

3.5.1 Introduction

Mobility measurement has shown promise in providing structural information of atomic clusters and has been successfully applied to elucidate the geometries of charged silicon clusters [38,42]. Experimentally, a short pulse of size selected cluster ions enter the drift tube full of inert buffer gas. The charged clusters are driven by a weak electric field and they will collide with the buffer gas atoms. By measuring the flight time of clusters across the drift tube the mobilities of the cluster ions are determined. Mobilities can be measured for both charged clusters: anions and cations (but not for neutrals). Theoretically, mobilities are modeled by calculating the collision integrals for a number of candidate geometries. The assignment of structures is obtained by comparing the modeled mobilities and measured values.

Most research to date have been carried out on cations. For example, the extensive research on carbon clusters that revealed structural transitions from chains to monocyclic and polycyclic rings to fullerenes [123–125], and demonstrated the isomerization of carbon rings into fullerenes [126–128] was performed mainly on cations. Mobility measurement for Si_n^+ indicated that there is a "prolate to spherical" structural transition for silicon cations [20]. Thus the theoretical models for mobility evaluation based on cluster ion geometries is built on the data of cations and only validated for cations. In the order of increasing sophistication thus computational expense, those models are:

1. The projection approximation that equates the collision integral to the orientationally averaged projection [124, 129].

2. The exact hard spheres scattering [130] (EHSS) model that replaces the collision integral by the orientationally averaged momentum-transfer cross section of a collection of hard spheres.

3. Trajectory calculation [131, 137] where the trajectories of buffer gas atoms are propagated in a realistic molecular potential of the target ion using the methods of molecular dynamics.

While the projection approximation produces large errors in many cases, [38, 132–134,

137] the EHSS and trajectory calculations have been successful in accurately predicting the mobilities of both homoatomic [17, 38, 40, 132–137] (C_n^+, Si_n^+,Ge_n^+) and heteroatomic [138–142] ($Na_nCl_{n+1}^-$, C_nSi^+, $C_{60}Nb_m^+$) clusters, as well as various bio-organic molecules [143, 144].

In many cases, anions have different structures from cations [38, 42, 132, 133]. For carbon clusters, the size range of certain structural families are different for C_n^+ and C_n^- [132, 133]. C_n^- also exhibit the structures of monocyclic rings with side chains attached ("tadpole") [145] which have not been observed for C_n^+. For $n \leq 20$, the global minima of Si_n^- are totally different from Si_n^+ for many sizes [42]. For an anion with the same geometry as the cation, the anion has two more electrons than the cation thus it has more densely and widely distributed electron cloud. The buffer gas atoms scatter on the electron cloud of charged clusters therefore the anion should have smaller mobility than the cation. While the EHSS and trajectory calculations have been very successful in modeling the mobilities of cations, these methods have not been verified for anions.

3.5.2 Mobilities of Charged Silicon Clusters: Si_n^+ and Si_n^-

3.5.2.1 Mobilities of charged silicon clusters determined by trajectory calculations and EHSS model

The mobility of a gas phase ion, K, is inversely proportional to the orientationally averaged collision integral [148], Ω_{avg},

$$K = \frac{(18\pi)^{1/2}}{16}\left[\frac{1}{m} + \frac{1}{m_b}\right]^{1/2} \frac{Ze}{(k_B T)^{1/2}} \frac{1}{\Omega_{avg}} \frac{1}{N} \tag{3.2}$$

where m and m_b are the masses of the ion and buffer gas atom, respectively. Ze is the ion's charge, N is the buffer gas atom number density and T is the buffer gas temperature.

The interaction of buffer gas atom and ions are modeled by Lennard-Jones potential plus a charge induced dipole term. The charge distribution over different atoms of the ions are calculated from DFT (the charge population calculated by LDA and GGA are essentially identical). For small clusters the charge is almost uniformly distributed on each atom. Starting

from n=9, the ionic charge becomes increasingly localized on just a few atoms. The collision integral is evaluated numerically by integrating the momentum transfer cross section between buffer gas and ion. A maxwellian distribution of relative velocities is assumed. The cross section is calculated by averaging a function of the scattering angle over the impact parameter and collision geometry and scattering angle is calculated from the interaction. The two parameters in the Lennard-Jones potential are fitted to reproduce the mobilities of Si_7^+ at both 78K and 298K.

The EHSS simplify the interaction between buffer gas atoms and ions using an exact hard spheres scattering model [130] instead of the Lennard-Jones potential. Only one parameter, the collision radius between the buffer gas atom and the ion was fitted to reproduce the measured mobility of the ion at a certain temperature. This simplified model works fine for Si_n^+ but failed for carbon system mainly because the buffer gas atoms can interact with the inner atoms of the carbon cluster, because of the much smaller C-C bond length (L $\sim$ 1.3 -1.4 Å), the hard sphere constructed by outer atoms can hardly model the interaction. The bondlength of Si, Ge, Sn and Na_nCl_{n+1} are $\sim$2.5, $\sim$2.7, $\sim$3.0 and $\sim$2.8 Å, respectively, and the EHSS model correctly predicts the mobilities of the cations of these systems. [140-142]. Thus we attempt to use the EHSS model to model the mobilities of Si_n^- [42]. Since the cross section of Si_n^- systematically exceed those of Si_n^+, a larger hard sphere radius is needed for Si_n^- and the value fitted to reproduce the mobility of Si_{10}^- is $R_{Si^-} = 3.09$ Å($R_{Si^+} = 2.92$ Å). The mobilities of the global minima for Si_n^- with n$\leq$20 are evaluated by this model and compared with measurement values in Fig. 3.9. We can see that the inverse mobilities which is proportional to the cross section increases faster than the experiment values as the cluster size grows. This difference persists regardless of which isomer's measured mobility is reproduced to fit the R_{Si^-} value. Thus, the EHSS model can not accurately model the mobilities of Si_n^-.

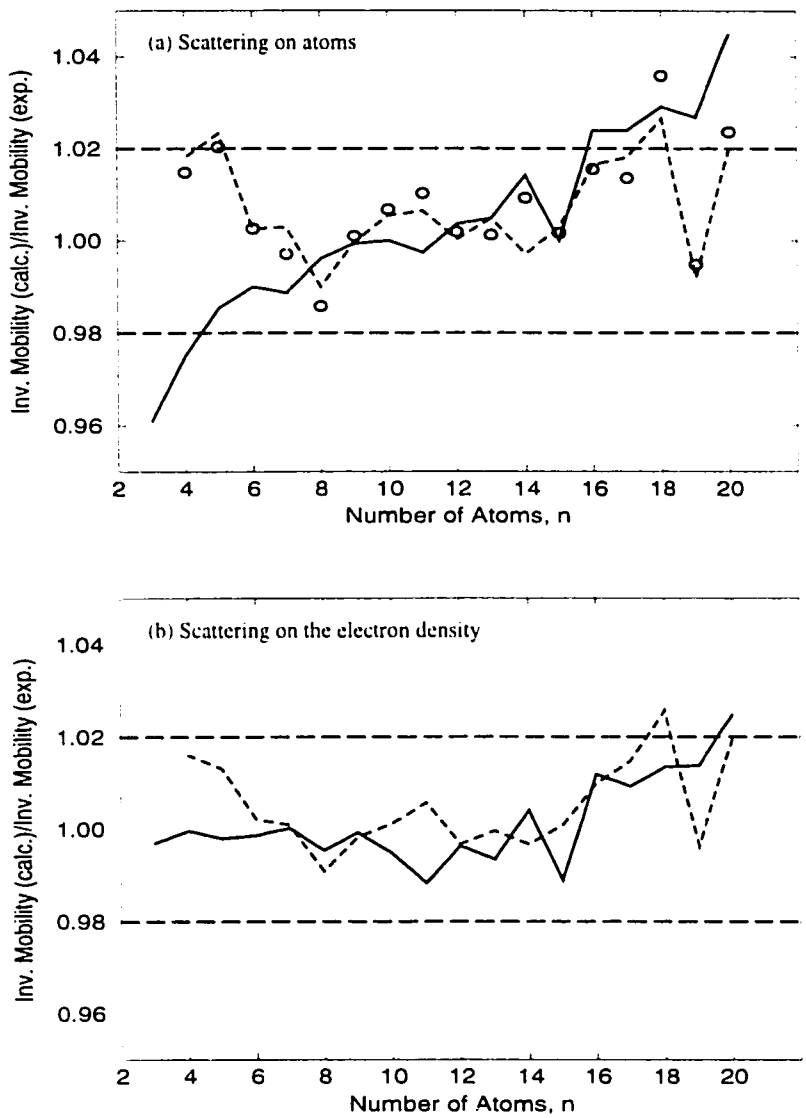

Figure 3.9 Inverse mobilities calculated for the lowest-energy (PWB except C_{2v} geometry for Si_{15}^{-}) Si_n cations (dotted line) and anions (solid line) in Fig. 3.4 relative to the high-resolution measurements (for the dominant isomers) (Ref. [16]). The C_{2h} isomer is chosen for Si_8^{+}. Lines in graph (a) result from the exact hard spheres scattering (EHSS) model (Ref. [130]) and those in (b) from the scattering on electron density isosurface (SEDI). Circles in (a) are by the trajectory calculations (Ref. [38]). Dashed lines delimit the customary 2% error margin (Refs. [123, 152])

3.5.2.2 Modeling the charged cluster's mobilities by scattering on the electronic density isosurfaces (SEDI)

Both the EHSS and trajectory calculation model the interaction between ions and buffer gas atoms by a potential tied to the position of the cluster nuclei. In trajectory calculation the potential is Lennard-Jones potential and in EHSS the potential is a hard sphere model without consideration of long range attraction. However, the scattering of buffer gas originates from the interaction between electrons instead of nuclei. As a rigorous quantum mechanics treatment is entirely out of question for this problem, a simplified approach involving some aspects of the electron cloud was developed [42]. In this approach, the electron cloud of the ion is described as a energy barrier wall of infinite height. The shape and position of the wall is determined by a fixed value of the ion's total electron density, E_{cut}. This is the only parameter to adjust to reproduce the measured mobility of a certain ion and then transfer to other systems. Conceptually this approach is similar to EHSS method except that in EHSS the position and the shape of the wall is determined by the spatial geometry of the cluster nuclei. The spatial distribution of the total electron density is calculated by DFT numerically on a three dimensional grid. Electron density isosurfaces are extracted from total electron density space distribution by setting a small density window around E_{cut} to filter out the points where the densities are outside the window. Thus an isosurface contour is obtained. The mesh is made finer until the calculated collision integral converges. This is typically achieved when the mesh size goes below 0.1 Å. Several thousands of points are needed for a small ion. This make the computation expense of SEDI comparable to that of trajectory calculations. The SEDI mobilities for Si_n^+ are within 1% of both trajectory calculations and EHSS values for Si_n^+ with n=4-20. The SEDI mobilities for those cations are in better agreement with the measured room temperature mobilities than either EHSS or trajectory calculations. When applied to anions, the SEDI mobilities of the global minima of Si_n^- are, unlike the EHSS mobilities, in excellent agreement with experiment (Fig. 3.9).

3.5.2.3 Structure assignment for Si_n^+ and characterization of "spherical" geometries

The trajectory calculation evaluated mobilities on the global minima we found and the previous measured mobilities are in excellent agreement for n≤17. [38] The previous structural assignment [38] are fully supported by the high resolution experimental data [16] and more accurate SEDI modeled mobilities. However, with the high resolution data, we can obtain more information [38].

As in the previous structure assignment [38], the modeled mobility of the T_d tetracapped octahedron isomer of Si_{10}^+ exceed the measurements by 2.5%-2.8%, which excludes this isomer. For Si_8^+, the trajectory calculation evaluated mobilities for the two degenerate isomers, the C_{2h} distorted bicapped octahedron and the C_s capped pentagon bipyramid, are so close that they can not be distinguished. However, the new SEDI mobility evaluation and the new experiment data exclude the C_s isomer. Unfortunately, like the previous comparison [38], the difference in mobilities between other reasonable low energy isomer for n≤13 is insufficient to unambiguously confirm the calculated global minima with the error margin of 2%, even for most sizes, the deviation of modeled mobilities of global minima from the measured values is only ~0.7%. For n=15, the cation isomers C_s (II) that is the lowest energy geometry in LDA and second lowest in GGA (Table 3.2) is disqualified as its modeled mobility exceed the measured value by ~2.5%. Similarly, the C_{3v} isomer of Si_{16}^+ can also be excluded. For n=17-19, two or three isomers are resolved in the high resolution measurement [16] instead of just one [38]. (Fig. 3.10) For Si_{17}^+, the two newly found [44] nearly-degenerate isomers (Fig. 3.4) have virtually identical mobilities that are closer to the major experimental peak at 1985 Vs/m^2 than that of the C_{3v} geometry found previously [38]. The calculated mobility of the third lowest energy (in PWB) isomer, which has the C_2 point group and is near-spherical, agree with the mobility of the smallest peak excellently. The C_{3v} geometry which is the second lowest energy isomer now may correspond to the middle intensity peak in Fig. 3.10. For Si_{18}^+, the modeled mobility of the newly found [44] global minimum with C_s point group (Fig. 3.4) agree with the measured mobility of the major peak perfectly while the previous lowest energy

C_{3v} isomer's (now the second lowest energy isomer) modeled mobility agree excellently with the mobility of the second peak (Fig 3.10). For Si_{19}^+, the modeled mobility of the new lowest PWB energy isomer's (the C_{2v} cage-like isomer has the lowest energy evaluated in LDA) (Fig. 3.4) agree with the mobility of the major peak in Fig. 3.10. While the C_{2v} cage-like structure's calculated mobility agree with the smallest peak excellently. Like Si_{19}^+, the lowest PWB energy isomer of Si_{20}^+, C_s (II), is the second lowest LDA energy isomer. Its calculated mobility agree with the measured value nicely. Noticing that for Si_{17}^+, Si_{18}^+ and Si_{19}^+, where multiple peaks correspond to different isomers are observed in the high resolution mobility measurement [16], the relative abundances of competing isomers are consistent with their PWB energy ordering and PWB energies and geometies agree with experiment better than those of LDA [38, 42, 44]. Therefore, it appears that cluster generation in these sizes is thermodynamically controlled. Mobility measurement show that the "prolate-to-spherical" transition begins at n=24 [20]. However, the assignment of minor features in the drift time distribution of Si_{17}^+ and Si_{19}^+ to the near-spherical isomers indicate that the cage-like isomers may begin to show up at smaller sizes in minor abundance. (Fig. 3.11)

3.5.2.4 Structural rearrangements between Si_n^+ and Si_n^- for n≤20

The absolute difference between the inverse mobilities of Si_n^- and Si_n^+ with n≤20 has been analyzed for silicon anion and cations' structure rearrangement [42]. With the new global minima for some sizes (Fig. 3.4), we redraw the size dependency of mobility gap between Si_n^- and Si_n^+ in Fig. 3.12. The dashed line is the same as the previous one [42] so it is not all produced on the global minima of cation morphologies because newly found global minima for cations. This should not affect out analysis because the dashed line exhibit the systematic mobility shift due to the systematic expansion of electronic cloud on going from cations to anions caused by the two extra electrons. The dashed line has no size dependent feature because the dashed assumes no structure transition. The solid line in Fig. 3.12, which described the mobility difference correspond to the assumption that the clusters in both charge states adopt

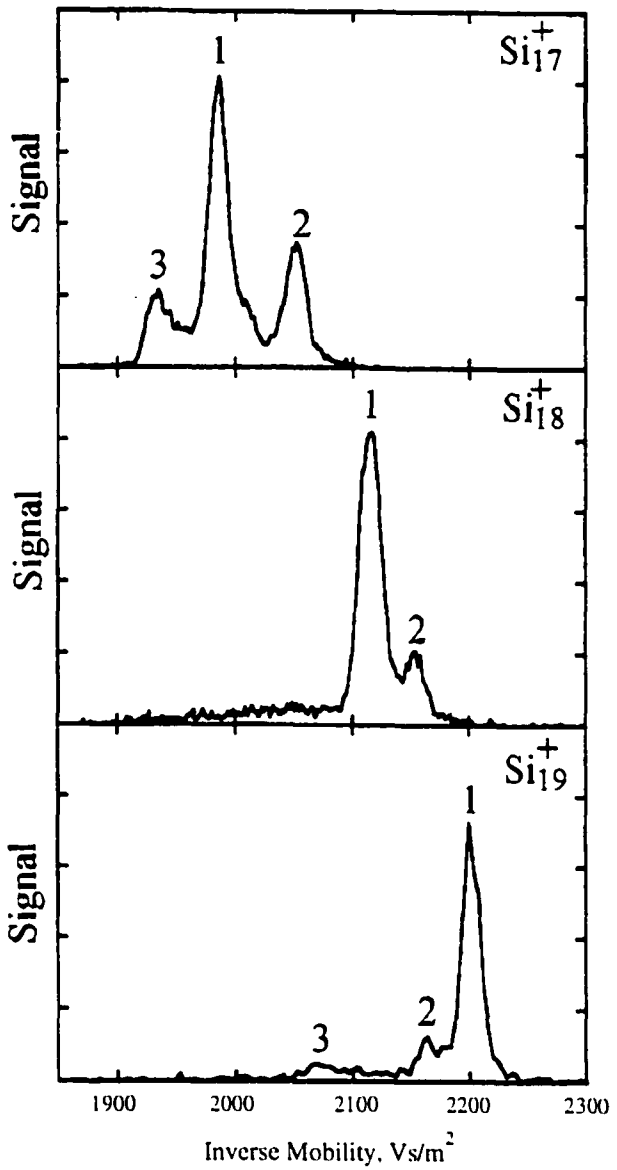

Figure 3.10 High-resolution drift time distributions (Ref. [16]) for Si_n^+ (n=17-19) with multiple isomers resolved.

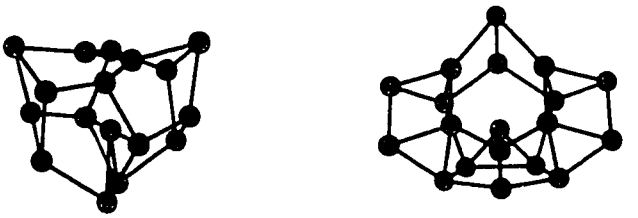

N = 17 C_2 N = 19 C_{2v}

Figure 3.11 Low-energy isomers for Si_n^+ (n=17-19) possibly observed in the high-resolution mobility measurements (Ref. [16]).

their lowest-energy geometries, exhibit the same overall trend as the previous one [42] (The modeled mobility for Si_{15}^- is the C_{2v} isomer (Fig. 3.4) because it is confirmed as the observed anion for n=15 by the PES [41] even its energy (PWB) is not the lowest). Besides the overall shift caused by the two extra electrons in anions, there are size-dependent features. The SEDI calculation reproduce all major minima in the experimental curve and they are: n=9, 15, 16, 18 and 19 (Fig. 3.12). These deviation from the overall shift show that for these sizes there are structure transition between anions and cations: anions of these sizes have more compact geometries than the cations of the same sizes. From Fig. 3.4 we can see that for these sizes the anions' structures are different from those of cations. For n=6, 8 and 11-14, the structure transitions (Fig. 3.4) can not be revealed by mobility measurements because the cross sections for these sizes are not detectably affected by the structure transitions.

The mobility analysis also exclude the distorted tricapped octahedron Si_9 C_s (I) and the tetracapped octahedron Si_{10} T_d which are extensively discussed in literature [49–53]. Just like cations [38], the previously proposed non-TTP structures for medium-sized silicon clusters, icosahedra, [82, 84, 149], "stacked puckered sixfold rings" [92, 95], "alternating stacked triangles" [93], "TBN" species retaining the "adamantane" tetrahedral bonding network of bulk Si [74], etc., are all ruled out for anions by the mobility measurements. From the energy order-

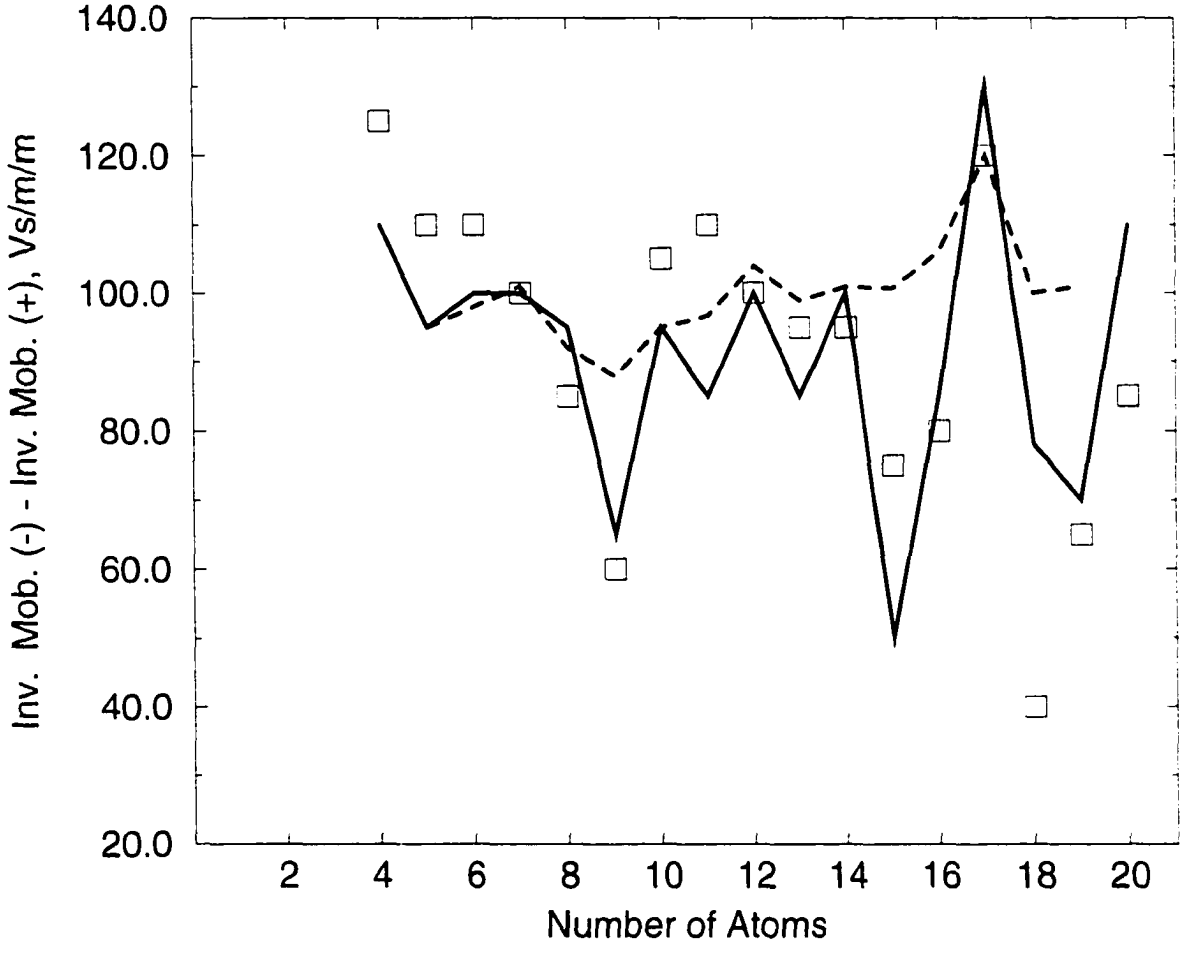

Figure 3.12 Gap between the inverse mobilities for Si_n^+ and Si_n^-. Squares are from the high-resolution measurement (for the dominant isomers) (Ref. [16]) and the lines are by SEDI calculations. The solid line corresponds to the assumption that the clusters in both charge states adopt their lowest-energy geometries [PWB, except that we have chosen the C_{2v} isomers for Si_{15}^-; Si_8^+ is assumed to have the C_{2h} structure]. The dashed line would be produced if the morphologies for Si_n anions were identified to those of global minima for cations save for a local relaxation.

ing in Table 3.2 we can see that anion favors the "prolate" geometries over the "spherical" ones. This is supported by mobility measurements. For cations of n=17 and 19, features correspond to spherical isomer show up in the mobility measurement while no "spherical" isomers are revealed in mobility measurement for the anions of these sizes and the "prolate" to "spherical" structure transition is delayed to larger sizes for anion.

3.6 Summary

Global minimum search are performed for neutral and charged silicon clusters with cluster size $n \leq 20$. In many cases, neutral, cation and anion take different structures. However, for $n \geq 10$, most of these structures contain the tricapped trigonal prism (TTP) subunits. These structures are "prolate" and agree with the mobility measurement which conclude that the Si_n structure transition from "prolate" to "near-spherical" happens at n=24-30. For neutral Si_n ($n \leq 20$), calculated ionization potentials (IPs) agree with the measurements except for n=20. For Si_n^+, modeled fragmentation pathways for Si_n^+ with $n \leq 26$ and dissociation energies of Si_n^+ with $n \leq 19$ agree with experiments excellently. The fragmentation pathways and dissociation energies are very energetic sensitive thus the excellent agreement with experiment verifies that our lowest energy geometries are very close to the true global minima in energy. For Si_n^-, the vertical detachment energies (VDEs) are calculated and compared with measurement. For isomers with reasonable agreement in VDEs, photoelectron spectra (PES) are modeled using molecular dynamics and compared with experiment. The agreement is excellent except for n=12, 20. Gas phase mobilities for charged silicon clusters (Si_n^+ and Si_n^-) are modeled and structures are assigned according to the comparison with measurement. The structure assignment agree with the structure assignment based on VDE, PES, fragmentation pathways and dissociation energy comparison. The agreement with measurements of calculated properties is a necessary but not sufficient criterion for accepting the optimized cluster structures. However, that such a wide range of data such as calculated IPs, mobilities, VDEs, PES, fragmentation pathways and dissociation energies based on the optimized cluster structures all agree with the

measurements is very strong support for the global minimum search of silicon clusters with $n \leq 19$ except Si_{12}^-.

CHAPTER 4 STRUCTURES OF GERMANIUM CLUSTERS: WHERE THE GROWTH PATTERNS OF SILICON AND GERMANIUM CLUSTERS DIVERGE

An enormous effort has been invested in the structural characterization of clusters of the group IV semiconductor elements, silicon and germanium. These are the two most important microelectronic materials, so understanding the growth habit of their clusters is of substantial practical revelance. From an academic viewpoint, cluster research is primarily driven by an interest in the evolution of the structure and properties of materials from the molecular to macroscopic regimes. In the bulk, both Si and Ge pack in a tetrahedral "diamond" lattice. As reviewed below, previous studies of Si_n and Ge_n found that the small clusters (with $n \leq 10$) also have identical geometries. Hence Si and Ge species were expected to be isomorphous in all size regimes. However, ion mobility measurements have revealed a large structural difference between the medium-sized clusters of these two elements [19,20]. Si_n^+ clusters grow as prolate structures that rearrange to near-spherical geometries over the $n \sim 24$-30 size range [20], while the near-spherical Ge_n^+ geometries do not appear until $n \sim 65$ [19]. It is important to determine exactly where the growth pathways of Si and Ge clusters diverge and where they converge. We consider the first issue in this contribution.

Previous efforts towards the structural characterization of Ge clusters have been less extensive than for silicon (Reviewed in Refs. [38,39]) and mostly limited to small sizes ($n \leq 10$). The mass spectra of Si_n and Ge_n appear nearly the same, with "magic number" for cations at n=4, 6, and 10 [153,154]. Unlike most other atomic clusters, both Si_n and Ge_n cations [13,19,39] and anions [13] with $n \geq 10$ fragment by fission rather than evaporation, ejecting neutrals with 4-11 atoms. The products of photodissociation [13] and collision-induced dissociation (CID)

[19] are almost identical, so the dissociation is statistical. Photoelectron spectra (PES) have been recorded for Ge_n anions ($n \leq 32$) [9, 155]. For n=3 and 4 , the vibrationally resolved features correspond to triangle and rhombus geometries analogous to those for Si_3^- and Si_4^-. Structural assignments for larger Ge_n^- have been made by modeling the observed electronic transitions [116, 156]. For n=5-9, all bands closely follow those for Si_n^-, which suggests structural isomorphism. Indeed, the optimized geometries for Si_n and Ge_n with $n \leq 10$ are the same [54, 67, 157-160]. The PES for Si_{10}^- and Ge_{10}^- are quite different [9, 116, 155, 156]. The global minimum (in LDA) is the C_{3v} tetracapped trigonal prism for Si_{10}^- while the C_{4v} bicapped tetracapped antiprism is the global minimum for Ge_{10}^- [116, 156]. However, the C_{3v} geometry is still the lowest energy one for both both neutrals [116, 156]. PES for larger clusters become increasingly featureless, which has prevented structural assignments. The assumed geometries for Ge_n with $n \geq 10$ have been studied using semiempirical methods only [161]. In summary, there has been no theoretical support for different Si_n and Ge_n geometry at any n.

We have mentioned that mobility measurements for cations show that the growth pathways of Si_n and Ge_n grossly diverge by n~25. However, a close examination of the size-dependent trends reveals that the difference occurs by n=15. To pinpoint the onset of this divergence and elucidate the growth of Ge clusters thereafter, we have searched for the lowest energy geometries of Ge_n and Ge_n^+ and compared them with those of the silicon analog [17, 38]. The energies of all isomers were evaluated using LDA and the gradient-corrected Perdew-Wang-Becke 88 (PWB) functional. For silicon, this functional yielded results in excellent agreement with experiment [38, 39]. For all calculations, we used the double numeric basis set with polarization functions as implemented in the all-electron DMOL code [30]. The search for the lowest energy Ge_n geometries was initially attempted by simulated annealing with the Car-Perinello LDA technique [31], but the geometries produced for n>13 were higher in energy than those obtained by relaxing the Si_n global minima for Ge_n. Clearly, simulated annealing fails to find the lowest energy geometries for Ge_n with n>13, as it failed for Si_n at about the same juncture [17]. We were able to proceed to larger Si_n using a genetic algorithm coupled with a new tight-binding potential. Unfortunately, no such potential presently exists for germanium.

and employing a genetic algorithm directly with DFT is computationally prohibitive. So we reoptimized many of the low-energy Si_n isomers for Ge_n. We expect that when the growth pathways of Si and Ge clusters just start to diverge, the Ge_n global minima should be among the low-energy geometries for Si_n. This assumption cannot be verified independently. However, the resulting Ge_n structures have been tested against experimental data as discussed below. In any case, for certain sizes the Ge_n geometries are lower in energy than the Si_n global minima relaxed for Ge. This proves the divergence of growth patterns between Si and Ge clusters, even if the above assumption is incorrect.

Our optimized structures for Ge_n with $n \leq 10$ agree with those previously accepted [54, 67, 116, 156-160]. They are the C_{2v} triangle for n=3, D_{2h} rhombus for n=4, D_{3h} trigonal, D_{4h} tetragonal, and D_{5h} pentagonal bipyramids for n=5, 6, and 7, respectively, the C_{2h} distorted bicapped octahedron for n=8, the C_{2v} (I) capped Bernal's structure for n=9, and the C_{3v} tetracapped trigonal prism for n=10. All cases where we found different geometries for Si_n and Ge_n (or Si_n^+ and Ge_n^+) with $n \leq 16$ are listed in Table 4.1. The only difference for $n < 11$ is that the C_1 capped pentagona bipyramid and the C_{2v} (II) distorted TTP, that are above the global minima by ~ 0.5eV for Si_8 and Si_9, respectively [38], become essentially degenerate with them for Ge_8 and Ge_9. For Si_{11}, the C_{2v} isomer of Raghvachari and Rohlfing [51] closely competes with our C_s (I) [38], but for Ge_{11} the C_s (I) isomer is lower by $\approx$0.35 eV and at least two other geometries are lower than the C_{2v}. The global minimum for Ge_{12} is the same as for Si_{12}: C_{2v} [17, 38], while the C_s geometry previously believed to be the ground state for Si_{12} is higher in energy by $\approx$ 0.7 eV. The structures of Si and Ge clusters first clearly diverge at n=13: Ge_{13} assumes the C_{2v} (II) structure, whereas the C_s isomer, the lowest energy one for Si_{13}, is the third lowest at $\approx$ 0.25 eV above the ground state. Si_{14} has only one low-energy isomer, C_s [38], so not surprisingly this geometry is shared by Ge_{14}. The global minimum for Si_{15} is C_{3v} , with less elongated D_{3h}, C_s (I), and C_s (II) isomers $\approx$ 0.2 eV higher [38]. For Ge_{15}, the ordering inverts to two isoenergetic structures, C_s (I) and C_s (II), and then near-degenerate D_{3h} and C_{3v} $\approx$ 0.15 eV higher. The difference between low-energy Si_n and Ge_n geometries increases for n=16: the C_{2h} (II) structure, the global minimum for Si_{16} [38], is $\approx$ 0.8 eV above

Table 4.1 Calculated PWB cohesive energies (eV) of selected Si and Ge cluster isomers (with respect to the spin-polarized isolated neutral atoms).

Size	Point group	Si_n	Si_n^+	Ge_n	Ge_n^+
8	C_{2h}	3.491[a]	2.596[a]	2.103[a]	2.143
8	C_1	3.422	2.596[a]	2.104[a]	2.151[a]
9	C_{2v}(I)	3.580[a]	2.753[a]	3.081[a]	2.305[a]
9	C_{2v}(II)	3.527	2.727	3.082[a]	2.306[a]
9	C_s	3.466	2.690	2.960	2.227
11	C_{2v}	3.618[a]	2.985	3.073	2.469
11	C_s(I)	3.620[a]	3.029[a]	3.105[a]	2.526[a]
11	C_s(II)	3.593	2.973	3.088	2.494
12	C_{2v}	3.648[a]	3.034	3.115[a]	2.543[a]
12	C_s	3.593	3.040[a]	3.060	2.521
13	C_s	3.634[a]	3.093	3.098	2.584
13	C_{2v}	3.616	3.102[a]	3.054	2.575
13	C_{2v}(II)	3.609	3.082	3.118[a]	2.591[a]
15	C_{3v}	3.701[a]	3.225[a]	3.153	2.707
15	D_{3h}	3.688	3.197	3.151	2.701
15	C_s(I)	3.685	3.203	3.162[a]	2.704
15	C_s(II)	3.684	3.219	3.162[a]	2.710[a]
16	C_{2h}(II)	3.672[a]	3.265[a]	3.104	2.701
16	C_{2h}(I)	3.659	3.236	3.091	2.683
16	C_s	3.661	3.240	3.133	2.723
16	C_{3v}	3.642	3.232	3.112	2.720
16	C_{2v}	3.642	3.230	3.157[a]	2.747[a]

[a] Energies of global minima.

the lowest energy C_{2v} geometry for Ge_{16}, and there are least the other structures in between. The global minima of Si_n and Ge_n for n=13, 15, and 16 are presented in Fig. 4.1.

We verified the geometries of Si_n neutrals using ionization potential measurements [38]. These are not available for Ge_n. However, ion mobilities, dissociation energies, and pathways are available. All these measurements were performed for cations. The structures of the cations with $n > 5$ have not previously been described, so we reoptimized a number of low-energy Ge_n geometries for Ge_n^+ searching for the global minima. In addition, simulated annealing was performed for $n < 11$. We found that for n=5, 6, 7 and 10, the lowest-energy cation structures are similar to those of neutral ground states, but Jahn-Teller distorted to lower symmetries: C_{2v} (as also pointed out in Ref. [157]), C_s, C_{2v}, and C_s, respectively. The lowest energy Ge_n^+ with $n \leq 11$ and n=14 are identical to Si_n^+ [38], except that for Ge_8^+ C_1 is clearly preferred to C_{2h} (for Si_8^+ C_1 and C_{2h} are degenerate [38]) and , for Ge_9^+ C_{2v} (I) and C_{2v} (II) are degenerate [for Si_9^+ C_{2v} (I) is preferred]. The lowest-energy Si_{12}^+ assumes a C_s geometry that is different from the C_{2v} neutral [41], but Ge_{12}^+ retains the C_{2v} structure of Ge_{12}. So in the DFT calculations the growth patterns of Si_n and Ge_n cations diverge at n=12, one size earlier than for neutrals. For n=13, 15, and 16, Si_n^+ and Ge_n^+ are different as they are for Si_n and Ge_n. The global minima for Ge clusters are less sensitive to ionization than those for Si ones, where energy ordering of isomers for cations and neutrals often differs [41].

The mobilities of Ge_n cations in He gas were measured at two buffer gas temperature: 78 and 295 K [17,38]. The mobilities for candidate isomers were evaluated by means of trajectory calculations employing a realistic cluster-He potential [132,137]. This potential was constructed as a sum of Lennard-Jones interactions between the He and each Ge atom plus a charge-induced dipole term that employs the computed partial charges on each atom. This model has been successfully used for Si_n^+ species [17,38]. The elementary LJ interactions were fit to reproduce the measured mobilities of small Ge_n cations with known geometries: the parameters derived were $\epsilon = 1.50$ meV for the potential depth and $\sigma = 3.45$ Å for the radial extent (the point where the potential becomes zero). These values are close to those for the Si-He potential [38]. Calculated and measured mobilities at 295 K are compared in

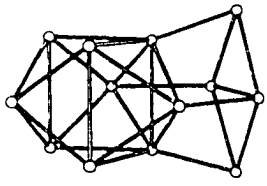

Ge N=13 C2v

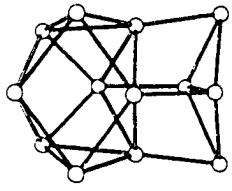

Si N=13 Cs

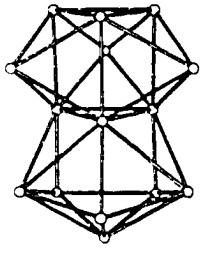

Ge N=15 Cs(I)

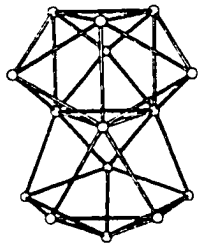

Ge N=15 Cs(II)

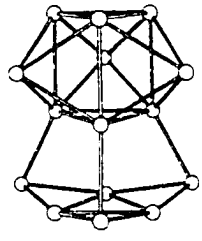

Si N=15 C3v

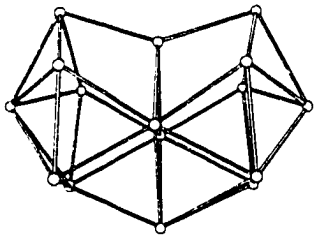

Ge N=16 C2v

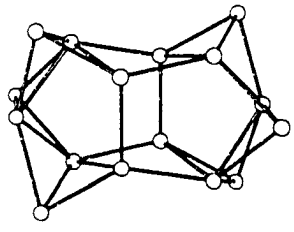

Si N=16 C2h

Figure 4.1 Lowest-energy geometries (in DFT) for the Si_n and Ge_n neutrals (n=13, 15, and 16).

Fig. 4.2. The values for the lowest-energy Ge_n^+ geometries described above all agree with the measurements, except for n=12. The agreement between calculations and experiment at 78 K is as good. However, the mobilities for Ge_{15}^+ C_{3v} and Ge_{16}^+ C_{2h} (II), the global minima for Si_{15}^+ and Si_{16}^+, do not match the measurements at either temperature. For Si clusters, these geometries agree with the experiment (but Si_{15}^+ C_s (I), Si_{15}^+ C_s (II), and Si_{16}^+ C_{2v} do not) [38]. The calculated mobilities for n $\geq$ 15 are quite sensitive to the cluster structure. For example, we have located six Ge_{16}^+ isomers within 1 eV from the lowest energy one. Their mobilities at 295 K deviate from the measurement by -2%, +2%, -4.5%, -4.5%, +2%, and -3%. An absolute deviation of $\leq$ 1% is expected for the correct geometry. So the global minimum for Ge_{16}^+ is the only isomer among at least seven low energy ones to agree with experiment. Unfortunately, the mobilities computed for Ge_{13}^+ C_{2v} (II) and Ge_{13}^+ C_s at either temperature are so close that they could not be distinguished in the experiments. The data do not support the C_{2v} structure for Ge_{12}^+, but the C_s geometry (the global minimum for Si_{12}^+) fits. As for silicon clusters [38], the room-temperature measurements exclude the octahedron-based geometries for Ge_9^+ (C_s tricapped octahedron) and Ge_{10}^+ (T_d tetracapped octahedron). Concluding, the mobility measurements confirm the onset of structural divergence between Si and Ge clusters by n=15 as predicted by DFT calculations.

Agreement with the mobility measurements is a necessary but not sufficient condition for a structural assignment, because different geometries often have similar mobilities. So it is important to determine directly if the cohesive energies of clusters are fully recovered by calculations. This is accomplished by comparing the computed dissociation pathways and their energies with experiment [39]. The measured primary fragmentation channels for Ge_n cations (n$\leq$23) [19] are the same as those for the Si_n^+, except that (i) Ge_9^+ loses Ge while Si_9^+ loses Si_3, and (ii) Ge_{22}^+ and Ge_{23}^+ eject Ge_7 but Si_{22}^+ and Si_{23}^+ eliminate Si_{10}. We have successfully predicted the main fragmentation channels for all Si_n^+ ($n\leq23$) except Si_{11}^+ using the PWB energies and assuming that the dissociation proceeds along the lowest energy pathway with no activation barrier to reverse processes [39]. This model has now reproduced all the primary experimental fragmentation channels for Ge_n^+ up to n=23, *including the changes* for n=9, 22,

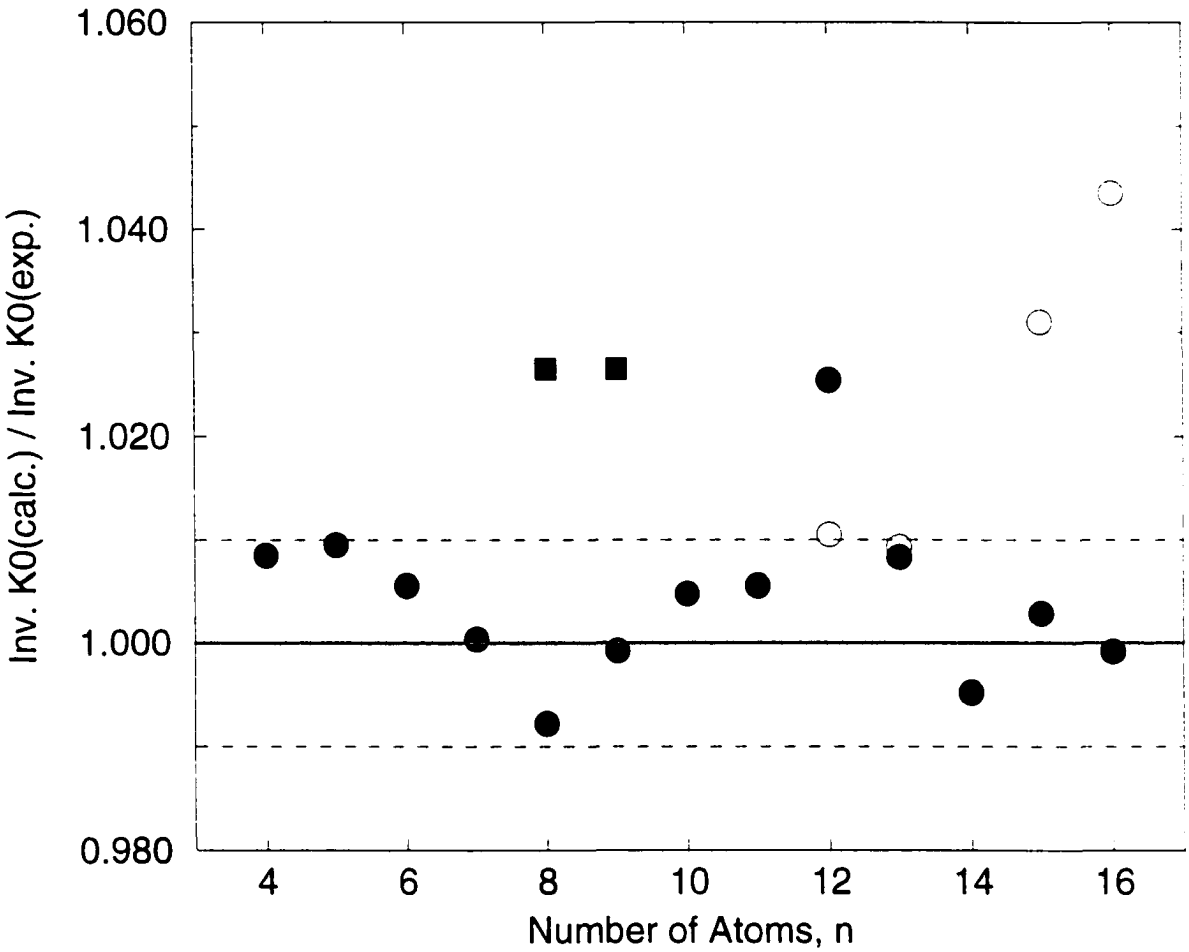

Figure 4.2 Relative deviations of the inverse mobilities (Inv. K_0) calculated for Ge_n cation from the measurements at 295 K. The filled circles are for the lowest-energy isomers, the empty circles are for the geometries that are global minima for Si_n^+, and the square are for the octahedron-based isomers of Ge_9^+ and Ge_{10}^+ (see text). The dotted lines delimit the error margin of 1%.

and 23. The difference in the dissociation of Si_9^+ and Ge_9^+ is not structurally induced, but that for n=22 and 23 is caused by the different geometries of Si_m^+ and Ge_m^+ for m=15 and 16, respectively. The lower energies of Ge_m^+ relative to Si_m^+ for these sizes make them the preferred products, and this causes the switch in the dissociation channels. If one assumes Ge_{15}^+ (Ge_{16}^+) to have the morphology of Si_{15}^+ (Si_{16}^+), the different dissociation products for n=22 (23) would not be explained.

The fragmentation pattern allows one to verify the relative energies of the proposed geometries, but the absolute values are best tested by dissociation energy measurements. The CID data [19] and our theoretical values are compared in Fig. 4.3. The agreement is quite good, which prove that our search has, at least, come close to the global minima on Ge_n^+ potential energy surfaces. The dissociation energies calculated for the geometries that are global minima for Si_n^+ (n=12, 13, 15 and 16) (dashed line) are obviously lower than for the geometries optimized fro Ge_n^+. For Ge_{16}^+ the difference is probably large enough to disqualify the C_{2h} (II) structure (the difference is somewhat underestimated in Fig. 4.3 because the DFT dissociation energies are systematically slightly larger than the experimental values).Thus the mobilities, fragmentation pathways, and dissociation energies are all consistent with the structures of Si and Ge clusters being different by n=16.

In summary, we have carried out a systematic ground state geometry search for the Ge_n neutrals and cations with up to 16 atoms. We have found that, like Si clusters, Ge clusters build up by stacking TTP subunits. However, the global minima for certain sizes starting from n=13 differ in details. The theoretical findings for cations are confirmed by the measured gas phase ion mobilities, dissociation energies, and fragmentation pathways.

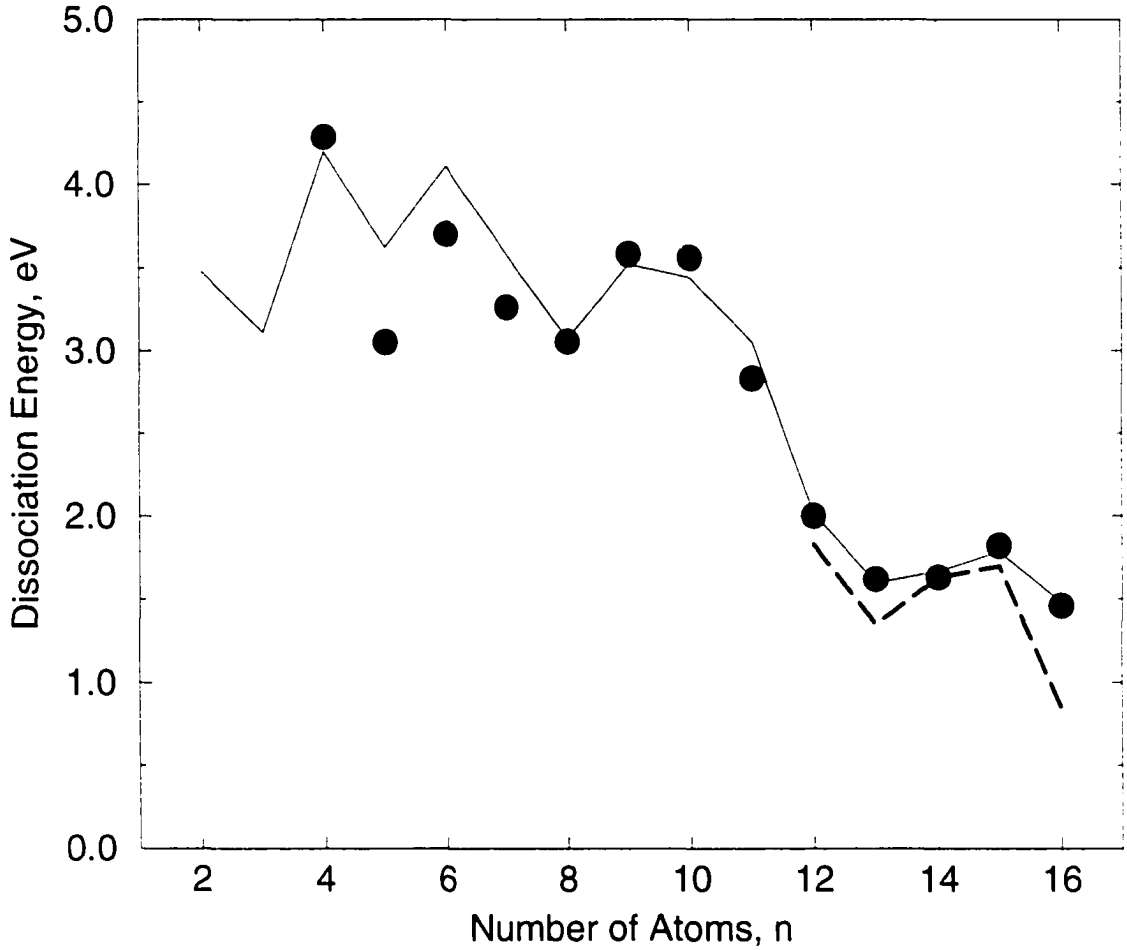

Figure 4.3 Dissociation energies of Ge_n cations. The circles are the experimental values [17], and the lines are the PWB calculations. The solid line is for the lowest-energy Ge_n^+ geometries and the dotted line (for n=12-16) is for the isomers that are global minima for Si_n^+.

CHAPTER 5 SILICON CLUSTERS ON SI(111) SURFACES

5.1 Introduction

Although enormous effort has been invested on the study of silicon clusters, most of the studies have been focused on isolated clusters. Recent scanning tunneling microscope (STM) study showed that there is a special type of cluster on Si(111) surfaces which is not only stable with respect to surface diffusion, but is also the fundamental unit in mass transport phenomena, step fluctuations in detachment and attachment of Si atoms at step edges, and epitaxial growth. [18] The STM study found that these "magic" clusters appear to be $\sim$ 1.5Å higher than Si adatoms on the Si(111)-(7×7) surfaces. The mirror symmetry of the (7×7) reconstruction along the $[\bar{1}\bar{1}2]$ direction is broken due to the presence of the cluster. An empty-state STM image of the cluster exhibits six protrusions with three slightly brighter than the other three. (Fig. 5.1(b)) The spacing between adjacent protrusions is $\sim$ 3.8 Å, which is much larger than the Si-Si bond length, indicating that the cluster contains more than six Si atoms. From the dynamic behavior of the clusters at step edges, the cluster size is estimated to be between 9 to 15 atoms. This special type of cluster is particularly stable because the clusters have never been observed to fragment into smaller clusters or grow into larger clusters by incorporation of additional Si adatoms or by coalescence of two clusters.

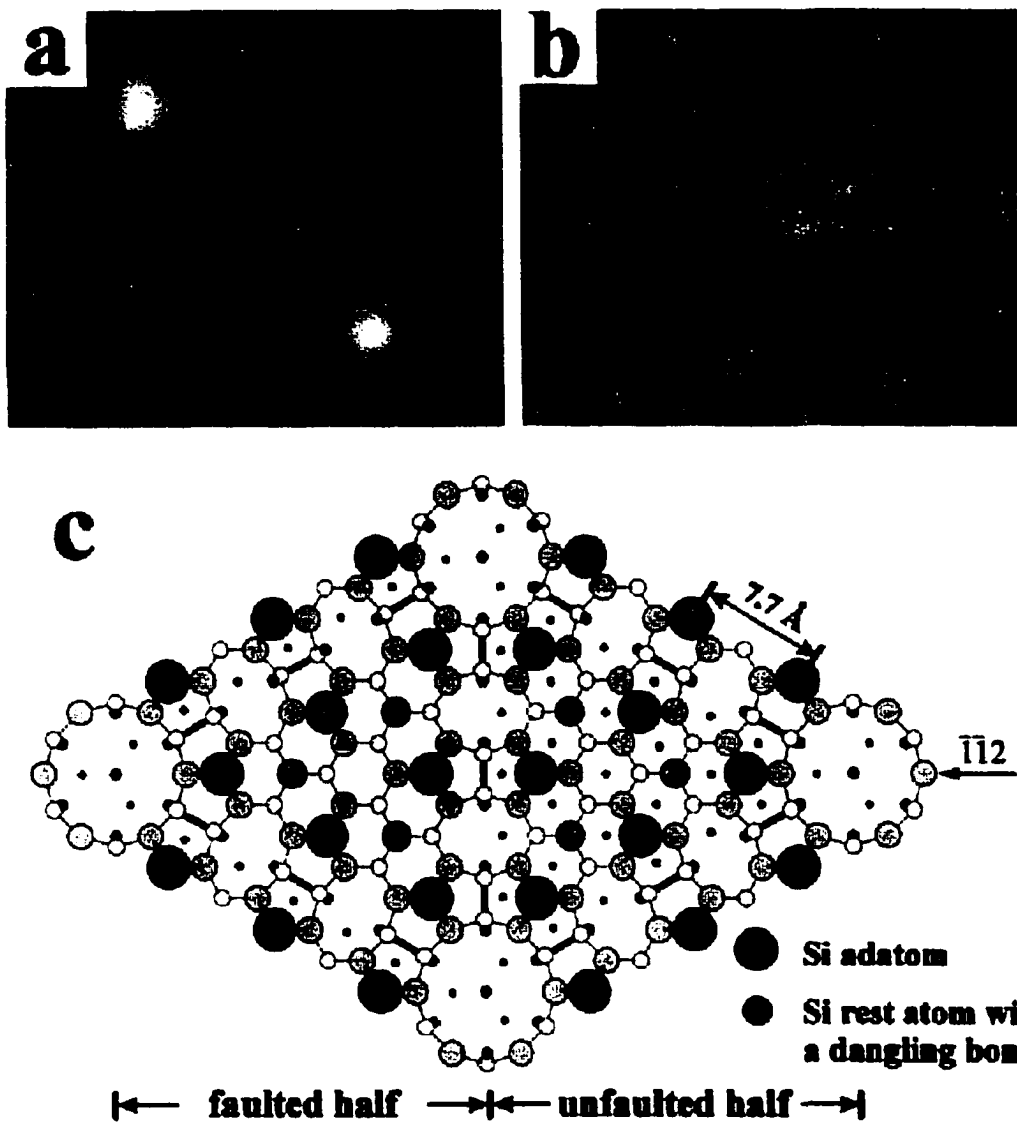

Figure 5.1 (a) STM image of two Si magic clusters taken at the sample bias of -1.5 V. (b) Another Si magic cluster taken at the sample bias of +1.2 V with a different tip. (c) Model of Si(111)-(7×7) with six protrusions seen in (b) marked with triangles. [18]

5.2 Theoretical Search for the Global Minima of Si Clusters on Si(111) Surfaces

5.2.1 Simulated Annealing by Tight-Binding Molecular Dynamics(TBMD)

Although STM studies [18] give valuable information about the overall shape of the magic silicon clusters on Si(111) surfaces, determination of the size and the precise atomic structure of the magic clusters has to rely on theoretical calculations.

Since the newly developed tight-binding model [17,37] has been very successful in the global minimum search of isolated silicon clusters, we use the same model to determine the structure of the magic cluster on the Si(111).

The (7×7) reconstruction of Si(111) is described by the well known dimer-adatom-stacking-fault (DAS) model. [162] (Fig. 5.2 (a)) In each unit cell of the (7×7) reconstruction, there are 12 adatoms on the top and 42 surface layer atoms. Six atoms in the surface layer called rest-atoms have one dangling bond each, while the other 36 surface atoms are saturated by the 12 adatoms on the top. The second layer has 48 atoms and all the inner layers have 7×7 = 49 atoms. In previous tight-binding calculations, the unit cell of the Si(111)-(7×7) surface takes 10 layers slab plus the two layers of adatoms which contain 498 atoms altogether. This substrate is too big to perform the global minimum search of the Si clusters on the Si(111) 7×7 surfaces in the present study. In order to make the simulations feasible, we reduce the number of atoms in the unit cell according to suggestions from the STM experiment [18]: (i) Since the magic clusters are found to be located on one half of the 7×7 unit cell, we will represent the substrate only by half of the 7×7 unit cell plus the dimers at the boundary between the two halves of the 7×7 unit cell (Fig. 5.2 (b)). (ii) Since the bonding between the magic cluster and the substrate involves only the adatoms and surface layer atoms, we will use a two-layer slab to model the substrate. The bottom layer of the slab is passivated by hydrogen atoms. After these simplifications, the substrate atom number is reduced to 87. (Fig. 5.2 (b)) These simplifications reduce the cost of computation significantly.

Simulated annealing is performed using tight-binding molecular dynamics (TBMD). We

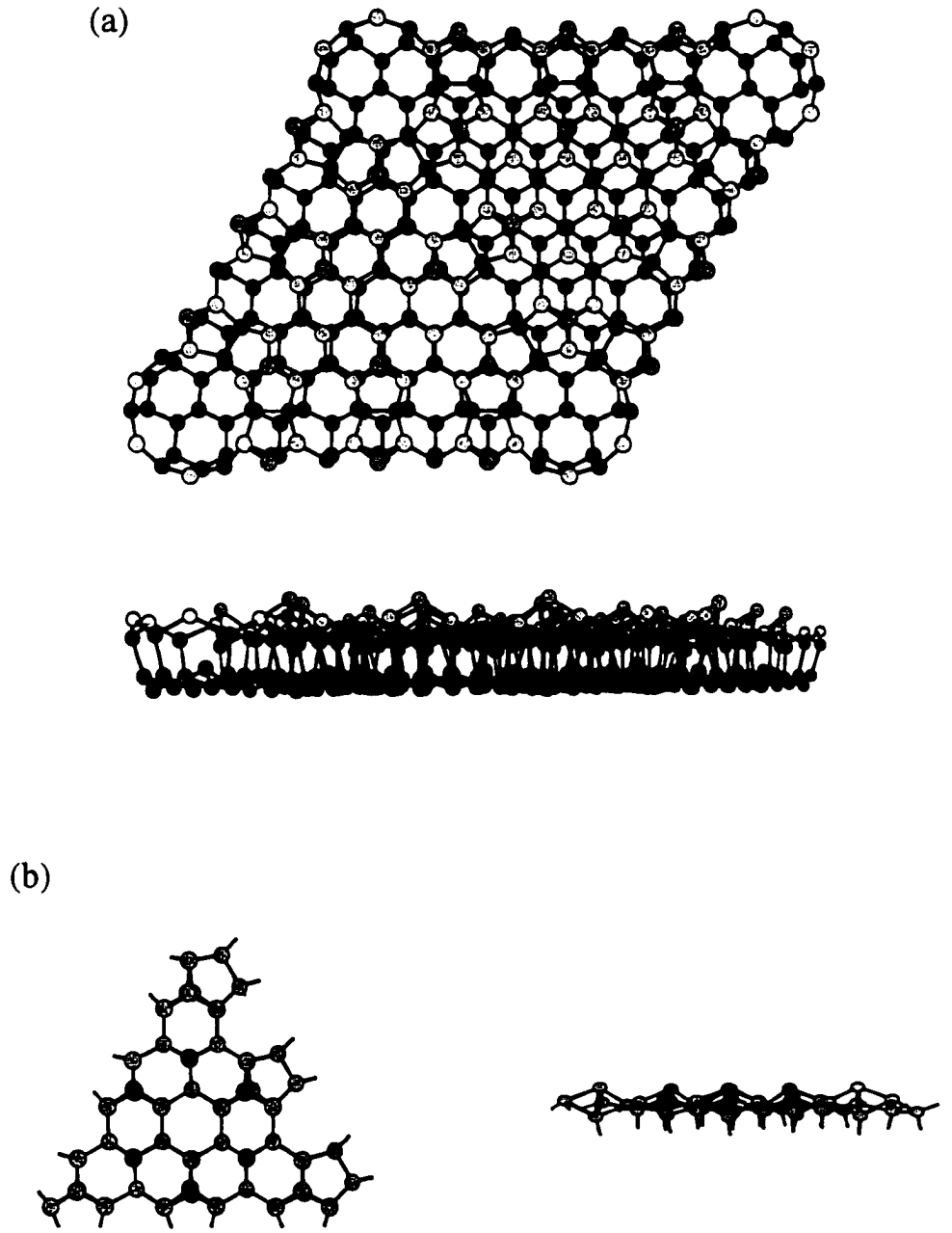

Figure 5.2 (a) The top view and side view of the DAS model for the 7×7 reconstruction of Si(111) surfaces. (b) The top view and the side view of the simplified substrate used in simulated annealing and GA. The blue atoms in (b) are the adatoms and rest atoms that may interact with the clusters.

randomly put atoms onto the substrate. The movements of the cluster atoms in the directions parallel to the substrate are confined in a cylinder which has a radius of 5.0Å and centered at the center position of the cluster according to the STM image (Fig. 5.1). When doing simulated annealing, we allow only the cluster atoms, three adatoms, and three rest-atoms (the blue atoms in Fig. 5.2 (b)) to move while the other atoms are kept at zero temperature. To improve the efficiency of the simulated annealing, we add a potential wall along the cylinder. whenever an atom hits the wall, it will bounce back to the cylinder region. Thus the simulated annealing is performed only on certain atoms and restricted in a cylinder region.

The geometries for various sizes of clusters after simulated annealing are listed in Fig. 5.3. We can see some common feature for different sizes of the clusters on Si(111) surface: One of the substrate adatoms is incorporated into the cluster and the dangling bonds of the three backbone atoms left behind are now saturated by other atoms in the cluster. The cluster also interact with the other two adatoms and two rest-atoms on the surface. When $n \geq 12$, the clusters show very clear three-dimensional lgrowth. Although simulated annealing gives us some valuable information on the bonding structure of the clusters on Si(111) surfaces, this method doesn't converge for this problem: Simulated annealing starting from different geometries often leads to different structures. This method is therefore not efficient for the global minimum search for the Si(111) surface cluster problem.

5.2.2 Global Minimum Structure Search by Genetic Algorithm

Genetic algorithms have been very successful in global minimum searches of isolate medium-sized silicon clusters [17,44]. Here we developed a genetic algorithm to perform the global minimum search of clusters on Si(111) surfaces. In this genetic algorithm:

(i) We maintain a pool of about 10 geometries sorted by their energies. Parent geometries are randomly chosen from the pool. This maintains the diversity of the parent geometries.

(ii) Children geometries are generated from parent geometries by cutting the 4 parent geometries in half. $4 \times 4 = 16$ geometries can be generated by the recombination of these half

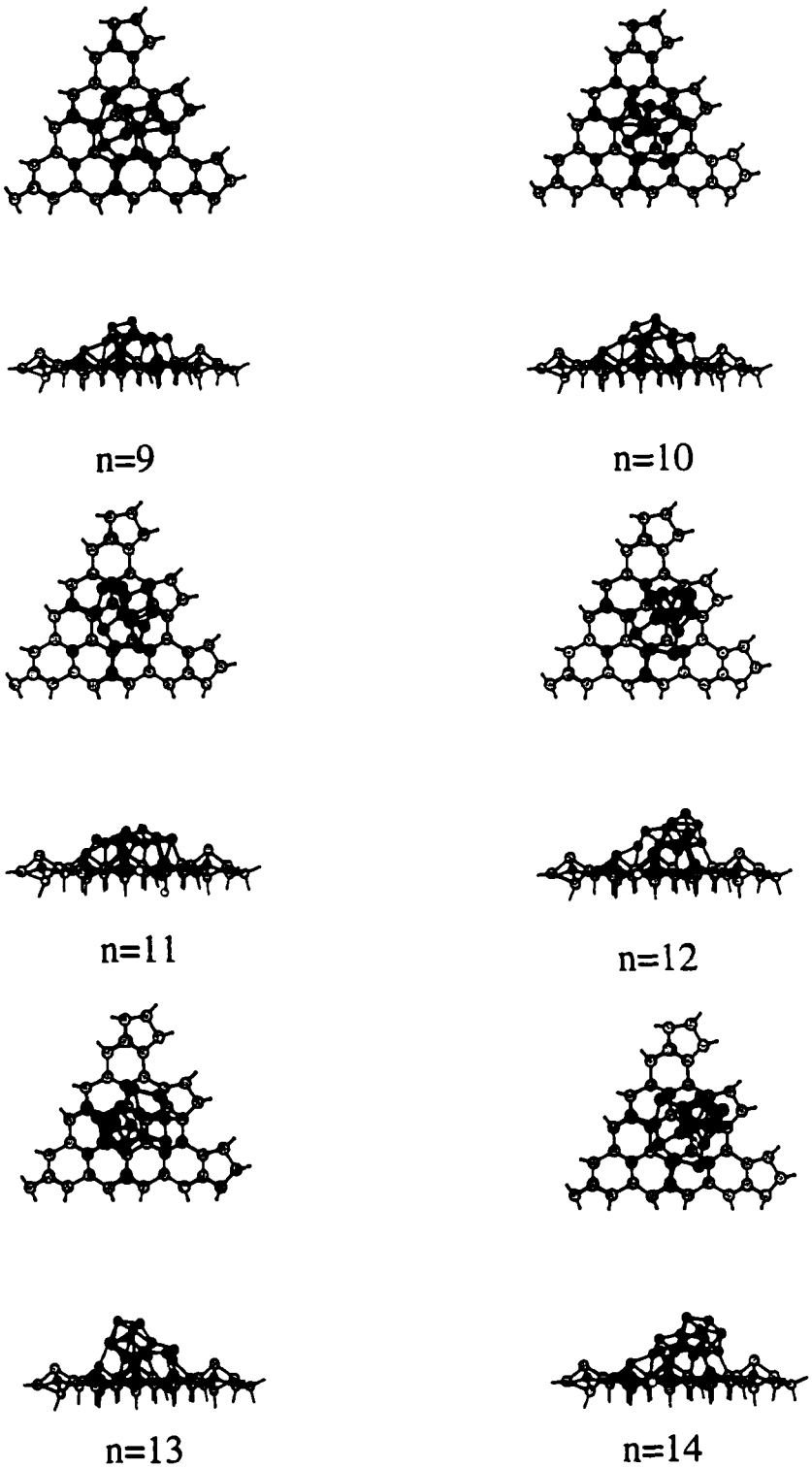

Figure 5.3 The geometries for cluster size n=9-14 after simulated annealing.

pieces. Among these 16 geometries, four are the parent geometries themselves and 12 are children geometries. These children geometries are then relaxed to the nearest local minima with the H atoms fixed and their energies are compared with those of the pool geometries. For a child whose energy is lower than any one of the pool, the child geometry is inserted into the pool and the pool is refreshed. Otherwise the child is discarded. The substrate (except the three rest-atoms and the three adatoms which are the blue atoms in Fig. 5.2 (b)) is relatively stable for various clusters on the surface since the clusters have no strong interactions with these atoms. Special treatment for these atoms is needed to keep the relative stability of the substrate when cutting the parent in half. We maintain a copy of imaginary atoms with the same coordinates as the original 7×7 unit cell for these atoms. Each of the relatively stable silicon atoms of the substrate have a correspondent atom in the imaginary atom set. Which half will these relatively stable silicon atoms go after cutting depends on which half will their correspondent imaginary atoms go.

(iii) Genetic algorithms are very easy to parallel because data passing is only required right after the child geometries' relaxation. Here we do not use the message passing interface (MPI) to pass data between different processes. Instead, we use a control process access the same files as the relaxation processes. The control process gathers geometries from those files, refreshes the parent pool, randomly chooses parents from the pool and generates child structures, then writes these child geometries to those files. Finally the relaxation processes read child structures from these files and perform the relaxation. The advantage of this method is that it doesn't need MPI and it can run on any group of machines as long as these machines share the same file server.

The lowest-energy geometries for different cluster sizes (n=6-14) found by the GA are listed in Fig. 5.4. These geometries have lower energy than those (Fig. 5.3) found by simulated annealing. Similar to the results from the simulated annealing, one of the substrate adatom is incorporated into the cluster leaving the three backbone atoms originally associate with it unsaturated. The clusters anchor on these three atoms, the other two adatoms, and the three rest-atoms. For n=6 and 7, the deposited atoms do not all connect together to form a cluster.

These deposited atoms prefer to saturate the dangling bonds already on the substrate. Notice that even for n=6 and 7, the bonds between one of the adatoms and the corresponding three backbone atoms are also broken and the adatom is bonded with the deposited atoms. Starting from n=8, the deposited atoms begin to form clusters. When $n \geq 13$, the clusters begin to grow in three dimensions.

To study the stability the silicon clusters on the Si(111) surface, we calculate the surface energy per cluster atom for the lowest energy structures for n=6-14. (Fig. 5.5) The surface energy per cluster atom E_{sur} is evaluated by the formula:

$$E_{sur} = \frac{E_s - E_p}{n} \tag{5.1}$$

where E_s is the total binding energy of the cluster with the substrate, and E_p is the total binding energy of the relaxed pure substrate with H atoms fixed. The magic cluster should have significantly lower surface energy per cluster atom than clusters of neighboring sizes. From Fig. 5.5 we can see that a good candidate is n=9. To confirm this result, LDA calculation of clusters on full 7×7 unit cell and STM image simulation are needed. The transition from two-dimensional growth to three-dimensional growth at n=13 is reflected by the kink at n=12 in Fig. 5.5.

Fig. 5.6 (a) and (b) are the two structures with 10 cluster atoms. To check the accuracy of our simplified calculation, we expanded the structures of Fig. 5.6 (a) and (b) to the full 7×7 unit cell (Fig. 5.6 (c) and (d)) and calculated their binding energies by LDA. The tight-binding energy difference per cluster atom between Fig. 5.6 (a) and (b) is 234 meV while the LDA binding energy difference per cluster atom between Fig. 5.6 (c) and (d) is 72 meV. The energy ordering of these two structures is unperturbed.

5.2.3 Summary

Both simulated annealing and genetic algorithm (GA) are performed to search for the ground states of clusters (n=9-14) on Si(111) surfaces. GA finds structures with lower energy than those found by simulated annealing for n=9-14. When $n \geq 13$, the clusters begin to grow

in three dimension. GA is also performed for n=6, 7, 8. when $n \geq 8$, the deposited atoms begin to bond together and form a cluster on the surface. The surface cluster with 9 atoms has the lowest surface energy within tight-binding.

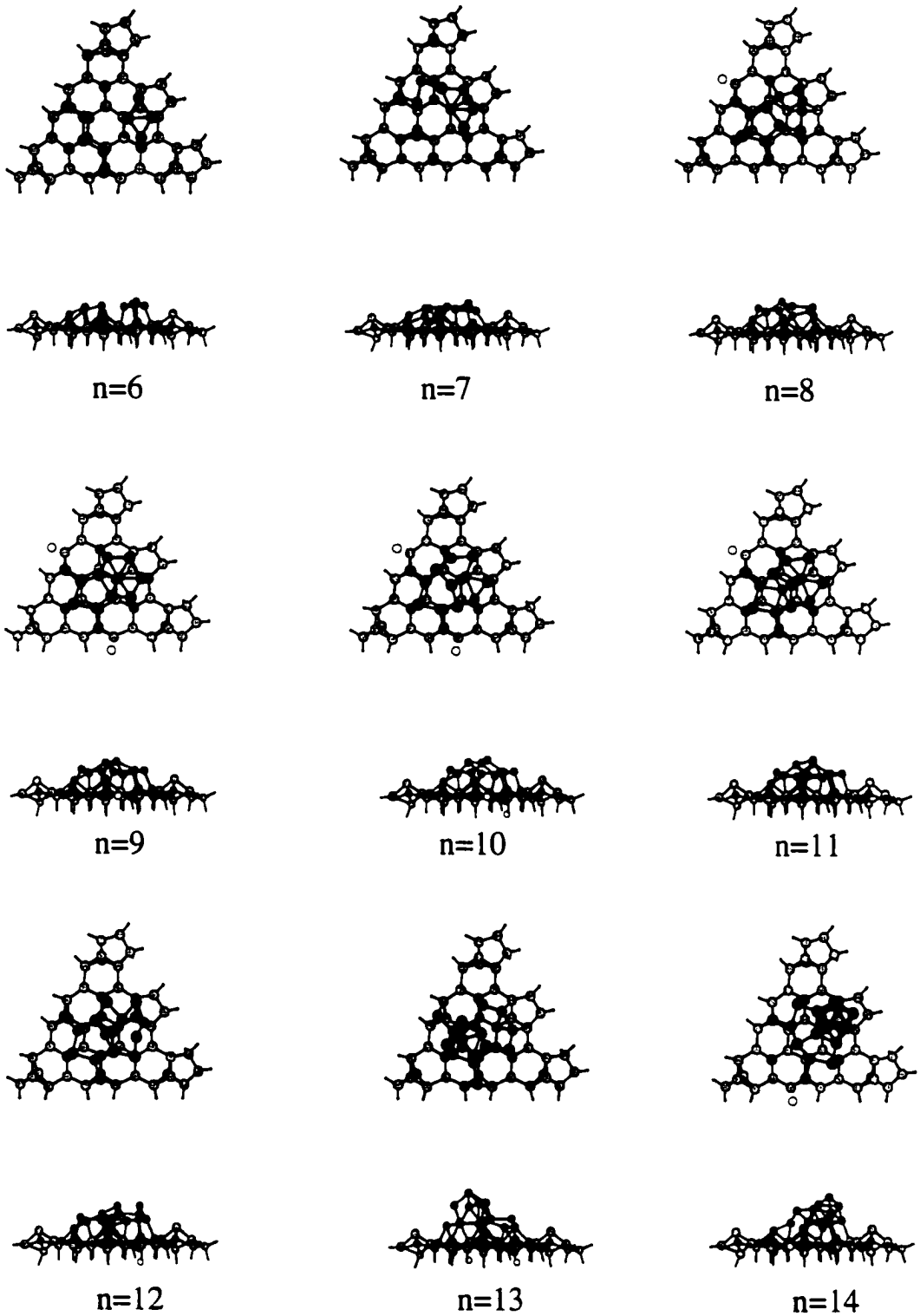

Figure 5.4 The geometries for cluster size n=6-14 optimized by genetic algorithm (GA).

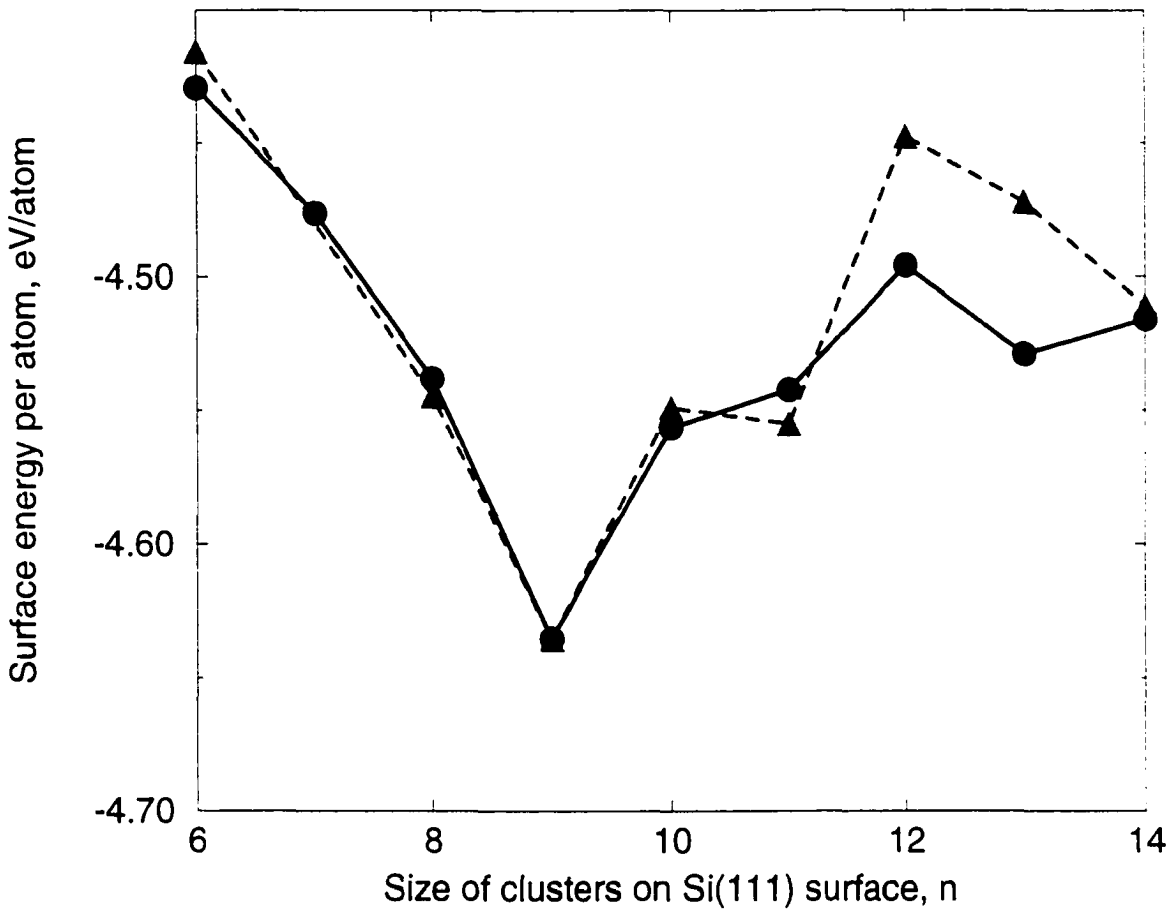

Figure 5.5 The surface energy per cluster atom for clusters (n=6-14) on Si(111) surface. The filled circle and solid line are for the simplified substrate. The triangle and dashed line are for the full Si(111) 7×7 unit cell substrate.

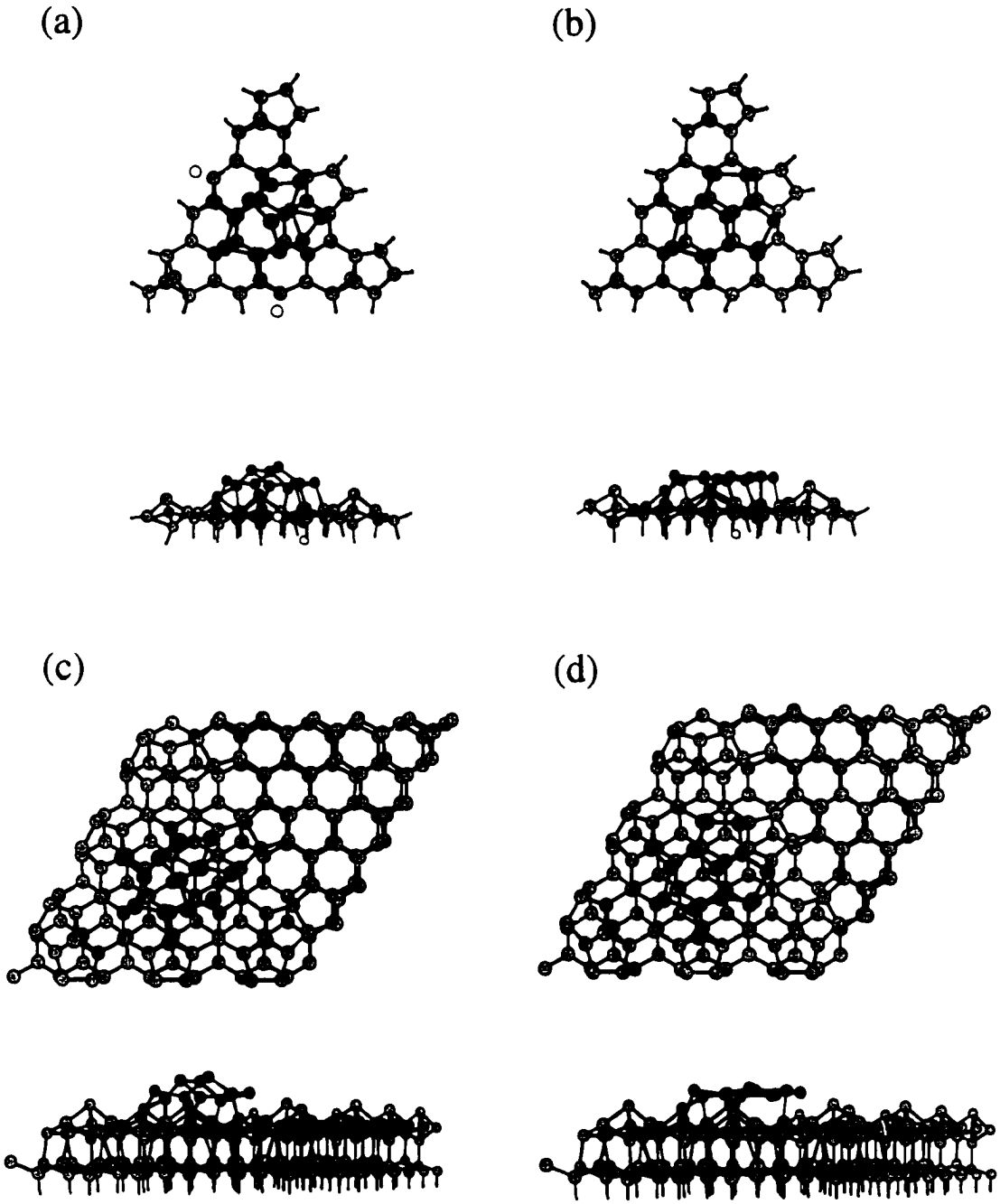

Figure 5.6 (a) The lowest energy structure found by GA for n=10. (b) An local minimum structure for n=10. (c) and (d) are structures expanded to full 7×7 unit cell from (a) and (b), respectively.

BIBLIOGRAPHY

[1] J. R. Heath, Y. Liu, S. C. O'Brien, Q. L. Zhang, R. F. Curl, F. K. Tittel, and R. E. Smalley, J. Chem. Phys. **83**, 5520 (1985)

[2] D. J. Trevor, D. M. Cox, K. C. Reichmann, R. O. Brickman, and A. Kaldor, J. Phys. Chem. **91**, 2598 (1987).

[3] K. Fuke, K. Tsukamoto, and F. Misaizu, Z. Phys. D **26**, S204 (1993); K. Fuke, K. Tsukamoto, F. Misaizu, and M. Sanekata, J. Chem. Phys. **99**, 7807 (1993).

[4] C. B. Winstead, S. J. Paukstis, and J. L. Gole, Chem. Phys. Lett. **237**, 81 (1995); A. Marijnissen and J. J. ter Meulen, **263**, 803 (1996).

[5] E. C. Honea, A. Ogura, C. A. Murray, K. Raghvachari, W. O. Sprenger, M. F. Jarrold and W. L. Brown, Nature (London) **366**, 42 (1993).

[6] S. Li, R. J. Van Zee, W. Weltner Jr. and K. Raghvachari, Chem. Phys. Lett. **243**, 275 (1995).

[7] C. C. Arnold and Daniel M. Neumark, J. Chem. Phys. **99**, 3353 (1993); **100**, 1797 (1994).

[8] C. Xu, T. R. Taylor, G. R. Burton and D. N. Neumark, J. Chem. Phys. **108**, 1395 (1998).

[9] O. Cheshnovsky et al., Chem. Phys. Lett. **138**, 119 (1987).

[10] H. Kawamata et al., J. Chem. Phys. **105**, 5369 (1996); R. Kishi et al., ibid. **107**, 10029 (1997).

[11] L. A. Bloomfield, R. R. Freeman, and W. L. Brown, Phys. Rev. Lett. **54**, 2246 (1985).

[12] W. Begemann, K. H. Meiwes-Broer and H. O. Lutz, Phys. Rev. Lett. **56**, 2248 (1986).

[13] Q. L. Zhang, Y. Liu, R. F. Curl, F. K. Tittel and R. E. Smalley, J. Chem. Phys. **88**, 1670 (1988).

[14] M. F. Jarrold and E. C. Honea, J. Phys. Chem. **95**, 9181 (1991).

[15] M. F. Jarrold and J. E. Bower, J. Chem. Phys. **96**, 9180 (1992).

[16] R. R. Hudgins, M. Imai, M. F. Jarrold, and Ph. Dugourd, J. Chem. Phys. **111**, 7865 (1999).

[17] K. M. Ho, A. A. Shvartsburg, B. Pan, Z. Y. Lu, C. Z. Wang, J. G. Wacker, J. L. Fye, and M. F. Jarrold, Nature (London) **392**, 582 (1998).

[18] I. Hwang, M. Ho, and T. T. Tsong, **83**, 120 (1999). M. Ho, I. Hwang, T. T. Tsong, **84**, 5792 (2000).

[19] J. M. Hunter *etal.*, Phys. Rev. Lett. **73**, 2063 (1994).

[20] M. F. Jarrold and V. A. Constant, Phys. Rev. Lett. **67**, 2994 (1991).

[21] M. Springborg, *Density – Functional Methods in Chemistry and Materials Science*, edited by M. Springborg, Chichester, New York, Wiley (1997).

[22] P. Hohenberg and W. Kohn, Phys. Rev. **136**, B864 (1964).

[23] W.Kohn and L. J. Sham, Phys. Rev. **140**, A1133 (1965).

[24] A. D. Becke, Phys. Rev. A. **38**, 3098 (1988).

[25] J. P. Perdew, *Electronic Structure of solids'* 91, edited by O. Ziesche and H. Esching, Akademie Verlag, Berlin (1991); J. P. Perdew and Y. Wang, Phys. Rev. B **33**, 8800 (1986).

[26] D. R. Hamann, M. Schlüter and C. Chiang, Phys. Rev. Lett. **43**, 1494 (1979).

[27] N. Troullier and J. L. Martins, Phys. Rev. B **43**, 1993 (1991).

[28] M.P. Allen and D.J. Tildesley, *Computer Simulation of Liquids*, Oxford [Oxfordshire], Clarendon Press, New York, Oxford University Press, (1987).

[29] C. W. Gear, The numerical integration of ordinary differential equations of various orders, Report ANL 7126, Argonne National Laboratory, (1996); C. W. Gear, *Numerical initial value problems in ordinary differential equations*, Prentice-Hall, Englewood Cliffs, NJ (1971).

[30] DMol package, V96.0/4.0.0, Molecular Simulations, Inc., San Diego CA (1995).

[31] R. car and M. Parrinello, Phys. Rev. Lett. **55**, 2471 (1985).

[32] J. Chelikowsky, N. Troullier and Y. Saad, Phys. Rev. Lett. **72**, 1240 (1994); X. Jing, N. Troullier, D. Dean, N. Binggeli, J. Chelikowsky, K. Wu and Y. Saad, Phys. Rev. B **50**, 12234 (1994).

[33] G. D. Smith, *Numerical Solutions of Partial Differential Equations : Finite Difference Mothods* (Oxford Univ. Press, Oxford, 1978), 2nd ed.

[34] G. Wannier, Phys. Rev. **52**, 191 (1937).

[35] J. C. Slater and G. F. Koster, Phys. Rev. **94**, 1498 (1954).

[36] C. Z. Wang and K. M. Ho, *Advances in Chemical Physics*, Vol XCIII, Edited by I. Prigogine and Stuart A. Rice, 1996 (John Wiley & Sons, Inc.).

[37] M. S. Tang, C. Z. Wang, C. T. Chan and K. M. Ho, Phys. Rev. B. **53**, 979 (1996).

[38] B. Liu, Z. Y. Lu, B. Pan, C. Z. Wang, K. M. Ho, A. A. Shvartsburg and M. F. Jarrold, J. Chem. Phys. **109**, 9401 (1998).

[39] A. A. Shvartsburg, M. F. Jarrold, B. Liu, Z. Y. Lu, C. Z. Wang and K. M. Ho, Phys. Rev. Lett. **81**, 4616 (1998).

[40] A. A. Shvartsburg, B. Liu, Z. Y. Lu, C. Z. Wang, M. F. Jarrold and K. M. Ho, Phys. Rev. Lett. **83** 2167 (1999).

[41] J. Muller, B. Liu, A. A. Shvartsburg, S. Ogut, J. R. Chelikowsky, K. W. M. Siu, K. M. Ho, and G. Gantefor, Phys. Rev. Lett. **85** 1666 (2000).

[42] A. A. Shvartsburg, B. Liu, M. F. Jarrold and K. M. Ho, J. Chem. Phys. **112**, 4517 (2000).

[43] A. A. Shvartsburg, B. Liu, K. W. M. Siu and K. M. Ho, to be published.

[44] I. Rata, A. A. Shvartsburg, M. Horoi, T. Frauenheim, K. W. M. Siu and K. A. Jackson, Phys. Rev. Lett. **85** 546 (2000).

[45] D. Forezag and T. Frauchheim, Phys. Rev. B **51**, 12947 (1995).

[46] B. K. Rao, S. N. Khanna and P. Jena, Phase transition, **24-26**, 35 (1990).

[47] K. Raghavachari and V. Logovinsky, Phys. Rev. Lett. **55**, 2853 (1985).

[48] K. Raghavachari, J. Chem. Phys. **84**, 5672 (1986).

[49] K. Raghavachari and C. M. Rohlfing, J. Chem. Phys. **89**, 2219 (1988).

[50] K. Raghavachari, Z. Phys. D **12** 61 (1989).

[51] C. M. Rohlfing and K. Raghavachari, Chem. Phys. Lett. **167**, 559 (1990).

[52] K. Raghavachari and C. M. Rohlfing, Chem. Phys. Lett. **198**, 521 (1992).

[53] K. Raghavachari, Phase transition, **24-26**, 61 (1990).

[54] G. Pacchioni and J. Koutecky, J. Chem. Phys. **84**, 3301 (1986).

[55] D. Tomanek and M. A. Schluter, Phys. Rev. Lett. **56**, 1055 (1986); Phys. Rev. B **36**, 1208 (1987).

[56] O. F. Sankey, D. J. Niklewski, D. A. Drabold, and J. D. Dow, Phys. Rev. B **41** , 12750 (1990).

[57] R. Fournier, S. B. Sinnott, and A. E. Depristo, J. Chem. Phys. **97**, 4149 (1992).

[58] P. Ballone, W. Andreoni, R. Car, and M. Parrinello, Phys. Rev. Lett. **60** 271 (1988); W. Andreoni and G. Pastore, Phys. Rev. B **41**, 10243 (1990).

[59] (a) W. Andreoni, Z. Phys. D **19**, 31 (1991); (b) U. Rothlisberger, W. Andreoni, and P. Giannozzi, J. Chem. Phys. **96**, 1248 (1992).

[60] M. V. Ramakrishna and A. Bahel, J. Chem. Phys. **104**, 9833 (1996).

[61] N. Binggeli, J. L. Martins, and J. R. Chelikowsky, Phys. Rev. Lett. **68**, 2956 (1992); J. R. Chelikowsky and N. Binggeli, Mater. Sci. Forum **232**, 87 (1996).

[62] J. R. Chelikowsky, N. Binggeli and K. M. Glassford, Z. Phys. D **26**, 51(1993)

[63] N. Binggeli and J. R. Chelikowsky, Phys. Rev. B **50**, 11764 (1994).

[64] P. Ordejon, D. Lebedenko, and M. Menon, Phys. Rev. B **50**, 5645 (1994).

[65] I. H. Lee, K. J. Chang, and Y. H. Lee, J. Phys.: Condens. Matter **6**, 741 (1994).

[66] A. Sieck, D. Porezag, T. Frauenheim, M. R. Pederson, and K. Jackson, Phys. Rev. A **56**, 4890 (1997).

[67] I. Vasiliev, S. Ogut, and J. R. Chelikowsky, Phys. Rev. Lett. **78**, 4805 (1997).

[68] A. Bahel, J. Pan, and M. V. Ramakrishna, Mod. Phys. Lett. B **9**, 811 (1995).

[69] T. Slee, L. Zhenyang, and D. M. P. Mingos, Inorg. Chem. **28**, 2256 (1989).

[70] L. Goodwin, A. J. Skinner, and D. G. Pettifor, Europhys. Lett. **9**, 701 (1989);

[71] K. Laasonen and R. M. Nieminen, J. Phys.: Condens. Matter **2**, 1509 (1990);

[72] S. Erkoc, Z. Phys. D **19**, 423 (1991);

[73] C. R. Zacharias, M. R. Lemes, and A. Dal Pino, Jr., J. Mol. Struct.: THEOCHEM **430**, 29 (1998).

[74] C. H. Patterson and R. P. Messmer, Phys. Rev. B **42**, 7530 (1990)

[75] S. Saito, S. Ohnishi, C. Satoko, and S. Sugano, J. Phys. Soc. Jpn. **55**, 1791 (1986); Z. Phys. D **14**, 237 (1989).

[76] J. A. Niesse and H. R. Mayne, Chem. Phys. Lett. **261**, 576 (1996).

[77] T. T. Rantala, D. A. Jelski, and T. F. George, J. Cluster Sci. **1**, 189 (1990).

[78] I. Kwon, R. Biswas, C. Z. Wang, K. M. Ho, and C. M. Soukoulis, Phys. Rev. B **49**, 7242 (1994).

[79] J. R. Chelikowsky and R. Keawing, Solid State Commun. **64**, 843 (1987);

[80] J. R. Chelikowsky, Phys. Rev. Lett. **60**, 2669 (1988).

[81] J. R. Chelikowsky, J. C. Phillips, M. Kamal, and M. Strauss, Phys. Rev. Lett. **62**, 292 (1989).

[82] J. R. Chelikowsky and J. C. Phillips, Phys. Rev. Lett. **63**, 1653 (1989); Phys. Rev. B **41**, 5735 (1990).

[83] J. R. Chelikowsky, K. M. Glassford, and J. C. Phillips, Phys. Rev. B **44**, 1538 (1991).

[84] J. C. Phillips, J. Chem. Phys. **87**, 1712 (1987); Phys. Rev. B **47**, 14132 (1993).

[85] A. Bahel and M. V. Ramakrishna, Phys. Rev. B **51**, 13849 (1995).

[86] A. D. Mistriotis, N. Flytzanis, and S. C. Farantos, Phys. Rev. B **39**, 1212 (1989).

[87] S. Li, R. L. Johnston, and J. N. Murrell, J. Chem. Soc., Faraday Trans. **88**, 1229 (1992); D. J. Wales and M. C. Waterworth, **88**, 3409 (1992).

[88] K. Jug, J. Mol. Struct.: THEOCHEM **202**, 277 (1989); H. Kupka and K. Jug, Z. Phys. D **13**, 301 (1989); Chem. Phys. **130**, 23 (1989); H. J. Nolte and K. Jug, J. Chem. Phys. **93**, 2584 (1990); K. Jug and U. Wolf, Chem. Phys. **163**, 69 (1992).

[89] B. L. Gu, Z. Q. Li, and J. L. Zhu, J. Phys.: Condens. Matter **5**, 5255 (1993).

[90] X. G. Gong, Q. Q. Zheng, and Y. Z. He, J. Phys.: Condens. Matter **7**, 577 (1995).

[91] D. A. Jelski, Z. C. Wu, and T. F. George, Chem. Phys. Lett. **150**, 447 (1988).

[92] E. Kaxiras and K. A. Jackson, Z. Phys. D **26**, 346 (1993); Phys. Rev. Lett. **71**, 727 (1993).

[93] J. C. Grossman and L. Mitas, Phys. Rev. Lett. **74**, 1323 (1995); Phys. Rev. B **52**, 16735 (1995).

[94] M. Menon and K. R. Subbaswamy, Phys. Rev. B **50**, 11577 (1994); 55, 9231 (1997).

[95] M. R. Pederson, K. Jackson, D. V. Porezag, Z. Hajnal, and T. Frauenheim, Phys. Rev. B **54**, 2863 (1996).

[96] J. Song, S. E. Ulloa, and D. A. Drabold, Phys. Rev. B **53**, 8042 (1996).

[97] R. P. Messmer, C. H. Patterson, Chem. Phys. Lett. **192**, 277 (1992).

[98] M. S. Tang, C. Z. Wang, C. T. Chan, K. M. Ho, Phys. Rev. B **53**, 979 (1996).

[99] S. Wei, R. N. Barnett, and U. Landman, Phys. Rev. B **55**, 7935 (1997).

[100] C. Jo and K. Lee, J. Korean Phys. Soc. **32**, 182 (1998).

[101] W. von Niessen and V. G. Zakrzewski, J. Chem. Phys. **98**, 1271 (1993).

[102] J. Zhao, X. Chen, Q. Sun, F. Liu, and G. Wang, Phys. Lett. A **198**, 243 (1995).

[103] R. Kishi, Y. Negishi, H. Kawamata, S. Iwata, A. Nakajima, and K. Kaya, J. Chem. Phys. **108**, 8039 (1998).

[104] M. Woeller, M. Mhlhuser, S. D. Peyerimhoff, and F. Grein, Chem. Phys. Lett. **288**, 603 (1998)

[105] G. von Helden, M. T. Hsu, N. Gotts, and M. T. Bowers, J. Phys. Chem. **97**, 8182 (1993); G. von Helden, N. G. Gotts, W. E. Palke, and M. T. Bowers, Int. J. Mass Spectrom. Ion Processes **138**, 33 (1994).

[106] J. M. L. Martin, J. El-Yazal, and J. P. Francois, Chem. Phys. Lett. **248**, 345 (1996); **252**, 9 (1996).

[107] K. A. Jackson, M. R. Pederson, D. Porezag, Z. Hajnal, and T. Frauenheim, Phys. Rev. B **55**, 2549 (1997).

[108] M. F. Jarrold, the Sicluster review paper.

[109] M. F. Jarrold and J. E. Bower, J. Phys. Chem. **92**, 5702 (1988).

[110] Y. Liu, Q. L. Zhang, F. K. Tittel, R. F. Curl and R. E. Smalley, J. Chem. Phys. **85**, 7434 (1986).

[111] K. Raghvachari and C. M. Rohlfing, Chem. Phys. Lett. **143**, 428 (1988).

[112] W. Begemann, S. Dreihofer, G. Ganteför, H. R. Sickmann, K. H. Meiwes-Broer, H. O. Lutz, *Element and Molecular Clusters*, T. P. Martin (ed.), Springer-Verlag, Berlin (1987).

[113] R. W. Schmude, Jr., Q. Ran, K. A. Gingerich, and J. E. Kingcade, Jr., J. Chem. Phys. **102**, 2574 (1995); Q. Ran, R. W. Schmude, Jr., M. Miller, and K. A. Gingerich, Chem. Phys. Lett. **230**, 337 (1994); K. A. Gingerich, Q. Ran, R. W. Schmude, Jr., Chem. Phys. Lett. **256**, 274 (1996).

[114] N. Binggeli and J. R. Chelikowsky, Phys. Rev. Lett. **75**, 493 (1995).

[115] J. R. Chelikowsky and N. Binggeli, Mater. Sci. Forum **232**, 87 (1996).

[116] S. Öğüt and J. R. Chelikowsky, Phys. Rev. B **55**, R4914 (1997).

[117] K. Raghavachari and C. M. Rohlfing, J. Chem. Phys. **94**, 3670 (1991).

[118] C. M . Rohlfing and K. Raghavachari, J. Chem. Phys. **96**, 2114 (1992).

[119] L. A. Curtiss, P. W. Deutsch, and K. Raghavachari, J. Chem. Phys. **96**, 6868 (1992).

[120] R. Kishi, H. Kawamata, Y. Negishi, S. Iwata, A. Nakajima, and K. Kaya, J. Chem. Phys. **107**, 10029 (1997).

[121] R. Kishi, S. Iwata, A. Nakajima, and K. Kaya, J. Chem. Phys. **107**, 3056 (1997).

[122] G. S. Icking-Konert, H. handschuh, P. S. Bechthold, G. Ganteför, B. Kessler and W.Eberhardt, Surf. Rev. Lett. **3**, 483 (1996).

[123] G. von Helden, M. T. Hsu, P. R. Kemper, and M. T. Bowers, J. Chem. Phys. **95**, 3835 (1991).

[124] G. von Helden, M. T. Hsu, N. G. Gotts, and M. T. Bowers, J. Chem. Phys. **97**, 8182 (1993).

[125] K. B. Shelimov, J. M. Hunter, and M. F. Jarrold, Int. J. Mass Spectrom. Ion Processes **138**, 17 (1994).

[126] J. M. Hunter, J. L. Fye, and M. F. Jarrold, Science **260**, 784 (1993).

[127] J. M. Hunter, J. L. Fye, and M. F. Jarrold, J. Chem. Phys. **99**, 1785 (1993).

[128] J. M. Hunter, J. L. Fye, E. J. Roskamp, and M. F. Jarrold, J. Chem. Phys. **98**, 1810 (1994).

[129] E. Mack, Jr. J. Am. Chem. Soc. **47**, 2468 (1925).

[130] A. A. Shvartsburg and M. F. Jarrold, Chem. Phys. Lett. **261**, 86 (1996).

[131] A. A. Shvartsburg and M. F. Jarrold, Phys. Rev. A **60**, 1235 (1999).

[132] A. A. Shvartsburg, G. C. Schatz, and M. F. Jarrold, J. Chem. Phys. **108**, 2416 (1998).

[133] A. A. Shvartsburg, R. R. Hudgins, Ph. Dugourd, and M. F. Jarrold, J. Phys. Chem. A **101**, 1684 (1997).

[134] A. A. Shvartsburg, R. R. Hudgins, R. Gutierrez, G. Jungnickel, T. Frauenheim, K. A. Jackson, and M. F. Jarrold, J. Phys. Chem. A **103**, 5275 (1999).

[135] A. A. Shvartsburg, L. A. Pederson, R. R. Hudgins, G. C. Schatz, and M. F. Jarrold, J. Phys. Chem A **102**, 7919 (1998).

[136] A. A. Shvartsburg,R. R. Hudgins, P. Dugourd, R. Gutierrez, T. Frauenheim,and M. F. Jarrold, Phys. Rev. Lett. **84**, 2421 (2000).

[137] M. F. Mesleh, J. M. Hunter, A. A. Shvartsburg, G. C. Schatz and M. F. Jarrold, J. Phys. Chem. **100**, 16082 (1996).

[138] G. von Helden, E. Porter, N. G. Gotts, and M. T. Bowers, J. Phys. Chem. **99**, 7707 (1995).

[139] J. L. Fye and M. F. Jarrold, Int. J. Mass Spectrom. **185/186/187**, 507 (1999).

[140] Ph. Dugourd, R. R. Hudgins, and M. F. Jarrold, Chem. Phys. Lett. **267**, 186 (1997).

[141] R. R. Hudgins, Ph. Dugourd, J. M. Tenenbaum, and M. F. Jarrold, Phys. Rev. Lett. **78**, 4213 (1997).

[142] J. P. K. Doye and D. J. Wales, Phys. Rev. B **59**, 2292 (1999).

[143] S. Lee, T. Wyttenbach, G. von Helden, and M. T. Bowers, J. Am. Chem. Soc. **117**, 10159 (1995).

[144] R. R. Hudgins, Y. Mao, M. A. Ratner, and M. F. Jarrold, Biophys. J. **76**, 1591 (1999).

[145] Ph. Dugourd, R. R. Hudgins, J. M. Tenenbaum, and M. F. Jarrold, Phys. Rev. Lett. **80**, 4197 (1998).

[146] M. F. Jarrold, J. Phys. Chem. **99**, 11 (1995).

[147] Ph. Dugourd, R. R. Hudgins, D. E. Clemmer, and M. F. Jarrold, Rev. Sci. Instrum. **68**, 1122 (1997).

[148] E. A. Mason, and E. W. McDaniel, *Transport Propeties of Ions in Gases* (Wiley, New York, 1988).

[149] T. Lange and T. P. Martin, Angew, Chem. Int.Ed. Engl. **31**, 172 (1992).

[150] U.Rothlisberger, W. Andreoni, and P. Giannozzi, J. Chem. Phys. **96**, 1248 (1992)./94

[151] C. E. Moore, Natl. Stand. Ref. Data Ser. (U.S., Natl. Bur. Stand.) **34**, 2 (1970).

[152] S. Lee, N. G. Gotts, G. von Helden, and M. T. Bowers, Science **267**, 999 (1995)

[153] T. P. Martin and H. Schaber, J. Chem. Phys. **83**. 855 (1985).

[154] W. Schulze, B. Winter, and I. Goldenfeld, J. Chem. Phys. **87**, 2402 (1987).

[155] G. R. Burton *et al.*, J. Chem. Phys. **104**, 2757 (1996); Y. Negishi *et al.* Chem. Phys. Lett. **294**, 370 (1998).

[156] J. R. Chelikowsky *et al.*, Mater. Res. Soc. Symp. Proc. **408**, 19 (1996).

[157] D. Dai and K. Balasubramanian, J. Phys. Chem. **96**, 9236 (1992); J. Chem. Phys. **96**, 8345 (1992); **105**, 5901 (1996); **108**, 4379 (1998).

[158] P. Jackson *et al.*, Int. J. Mass. Spectrom. Ion. Process. **164** 45 (1997).

[159] E. F. Archibong and A. St-Amant, J. Chem. Phys. **109**, 962 (1998).

[160] M. Menon, J. Phys. Condens. Matter **10**, 10991 (1998).

[161] G. A. Antonio *et al.*, J. Chem. Phys. **88**, 7671 (1988). A. M. Mazzone, Phys. Rev. B **54**, 5970 (1996); P. K. Sitch, T. Frauenheim, and R. Jones, J. Phys. Condens. Matter **8**, 6873 (1996).

[162] K. Takayanagi, Y. Tanishiro, M. Takahashi, and S. Takahashi, J. Vac. Sci. Technol. **A 3**, 1502 (1985). K. Takayanagi, Y. Tanishiro, S. Takahashi, and M. Takahashi, Surf. Sci. **164**, 367 (1985).